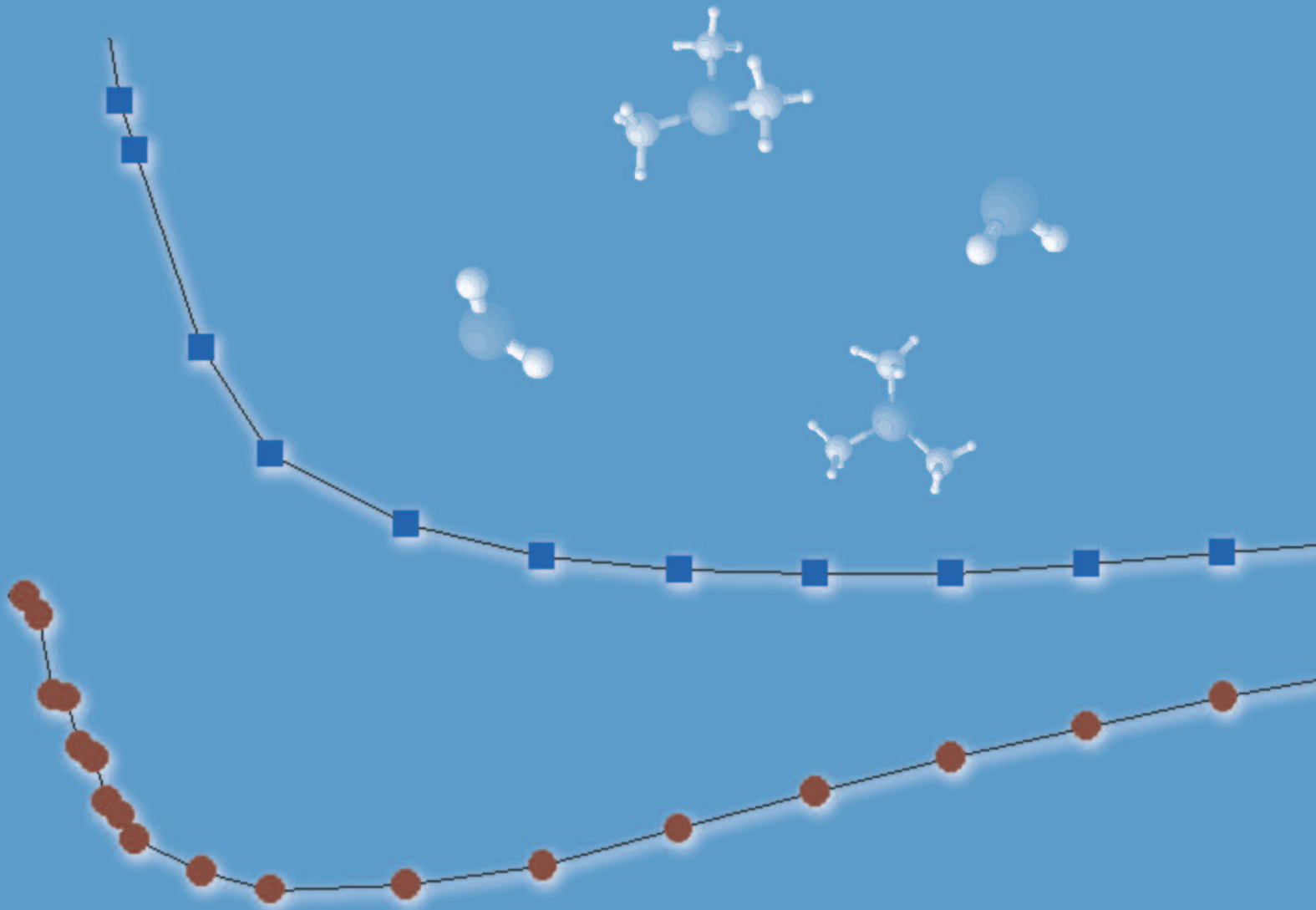


Luca Lamagna

Atomic layer deposition and characterization of rare earth oxides for innovation in microelectronics



Tutor: Prof. Marco Fanciulli



Università degli Studi di Milano-Bicocca

Dipartimento di Scienza dei Materiali
Ph.D. School in Nanostructures & Nanotechnologies
XXII cycle 2006-2009

Dissertation for the degree of Doctor of Philosophy

Atomic layer deposition and characterization of rare earth oxides for innovation in microelectronics

Candidate: Luca Lamagna
Matr. 708225

Tutor: Prof. Marco Fanciulli
Coordinator: Prof. Leo Miglio

Milano, December 17th 2009



Laboratorio Nazionale MDM
CNR-INFM

An online record is available on: <http://www.boa.unimib.it/>

© 2009 Luca Lamagna and Laboratorio Nazionale MDM, CNR-INFM.
All rights reserved. This work may not be translated or copied in whole or in part without
the written permission of the author.

INDEX

| | |
|---|-----------|
| Chapter 1: Introduction | 1 |
| Motivations of the research and framework of the activity | 1 |
| Innovation in micro- and nanoelectronics | 2 |
| Germanium and III-V high-mobility substrates | 7 |
| Rare Earth Oxides | 9 |
| Outline of the Thesis | 10 |
| | |
| Chapter 2: Experimental | 15 |
| Introduction | 15 |
| Atomic Layer Deposition | 16 |
| Spectroscopic Ellipsometry | 20 |
| Characterization techniques | 22 |
| | |
| Chapter 3: La-based oxides | 27 |
| Introduction on La-based oxides | 28 |
| Hexagonal La ₂ O ₃ phase: stabilization and dielectric properties | 29 |
| Crystallographic evolution of La ₂ O ₃ films upon annealing | 30 |
| Structural and chemical properties of La ₂ O ₃ /Si interfaces | 31 |
| Atomic layer deposition of La ₂ O ₃ using La(ⁱ PrCp) ₃ | 33 |
| Introduction on LaZrO compounds | 40 |
| Atomic layer deposition of LaZrO | 41 |
| | |
| Chapter 4: Er-based oxides | 53 |
| Introduction on Er-based oxides | 54 |
| Atomic layer deposition of ErHfO | 55 |
| Atomic layer deposition of Er-doped HfO ₂ | 64 |

| | |
|---|------------|
| Chapter 5: High-<i>k</i> oxides on high-mobility substrates | 69 |
| Introduction on high- <i>k</i> oxides on high-mobility substrates | 70 |
| La ₂ O ₃ on Ge(100) | 71 |
| La-doped ZrO ₂ on Ge(100) | 75 |
| Er-doped HfO ₂ on Ge(100) | 79 |
| Atomic layer deposition of high- <i>k</i> oxides on III-V substrates | 82 |
| | |
| Chapter 6: <i>In situ</i> Spectroscopic Ellipsometry | 87 |
| <i>In situ</i> Spectroscopic Ellipsometry of thin films grown by Atomic Layer Deposition | 88 |
| Substrate effect: study of the Si(100) and Ge(100) cases | 93 |
| <i>In situ</i> characterization of Er-doped HfO ₂ films | 97 |
| APPENDIX: SE modeling of ultra thin films | 98 |
| | |
| Chapter 7: Thermal and Plasma Assisted Atomic Layer Deposition of Ruthenium thin films | 101 |
| APPENDIX: SE modeling of metal thin films | 109 |
| | |
| Chapter 8: Conclusions | 113 |
| List of publications related to this work | 115 |

Acknowledgements

Curriculum Vitae

LIST OF ABBREVIATIONS AND ACRONYMS

ALD: Atomic Layer Deposition
CET: Capacitance Equivalent oxide Thickness
CMOS: Complementary Metal Oxide Semiconductor
Cp: Cyclopentadienyl, C₅H₅
CV: Capacitance Voltage
CVD: Chemical Vapor Deposition
D_{it}: Density of Interface Traps
DRAM: Dynamic Random Access Memory
EELS: Electron Energy Loss Spectroscopy
EOT: Equivalent Oxide Thickness
ErHfO: Er_xHf_yO_z
FTIR: Fourier Transform Infrared spectroscopy
GI: Grazing Incidence
HR: High Resolution
IC: Integrated Circuit
IL: Interfacial Layer
ⁱPr: isopropyl, -CH(CH₃)₂
IV: Current Voltage
LaZrO: La_xZr_yO_z
Me: methyl, -CH₃
ML: Monolayer
MOSFET: Metal Oxide Semiconductor Field Effect Transistor
NVM: Non-Volatile Memory
PA-ALD: Plasma Assisted Atomic Layer Deposition
R&D: Research and Development
RE: Rare Earth
REO: Rare Earth Oxide
RTA: Rapid Thermal Annealing
SAED: Selected Area Electron Diffraction

SE: Spectroscopic Ellipsometry
SIMS: Secondary Ion Mass Spectroscopy
STEM: Scanning Transmission Electron Microscopy
TEM: Transmission Electron Microscopy
ToF: Time of Flight
TXRF: Total reflection X-Ray Fluorescence
XPS: X-ray Photoelectron Spectroscopy
XRD: X-Ray Diffraction
XRR: X-Ray Reflectivity

Chapter 1

Introduction

Motivations of the research and framework of the activity

The research activity described in this thesis was mainly carried out in the framework of the European project REALISE “Rare earth atomic layer deposition for innovation in electronics” [1]. The principal project aims were to:

- deposit high permittivity rare earth oxide layers with sub-nanometer control
- integrate these dielectrics into innovative memory and communication devices

The idea was to develop and optimize the deposition process of novel ultra-thin dielectric films and to investigate and characterize their physical and chemical properties before testing them for applications in innovative microelectronic devices. The growth process which was the subject of the research is atomic layer deposition (ALD). Nowadays, this technique is one of the leading technologies employed for deposition of nanometer-scale films at an industrial level. Indeed ALD allows deposition of conformal ultra-thin layers with an extremely precise thickness control. Moreover, ALD growth processes are scalable up to 8” or 12” large area substrates making this technique very promising for the necessities of high-throughput industries.

Most of the materials investigated in this study belong to the rare earth oxides (REOs) family. Rare earth-based binary and ternary oxides are high dielectric constant (high- k) materials which might be successfully employed in several microelectronic fields. Indeed, the scaling down of the device dimensions requires the employment of ever-thinner insulating dielectric layers for logic, memory and communication applications. Appropriate physical and chemical stability are required together with stringent electrical requisites in terms of permittivity value and leakage current. Thus, a variety of high- k dielectrics was identified, deposited using ALD and characterized in order to assess the potential implementation in advanced nano-scaled devices. The REOs were deposited on different semiconductor substrates in order to address different oxide/semiconductor interfaces. In addition, an *in situ* study of the ALD processes and of the film and interface optical properties was performed using spectroscopic ellipsometry during the deposition of the various stacks.

Therefore, the research activity was balanced between the development of new ALD processes and the assessment and the discussion of more fundamental scientific issues connected with the structural, chemical and electrical properties of the thin films grown by ALD.

Innovation in micro- and nanoelectronics

Device scaling and high-*k* dielectrics

The fast and continuous progress of science and technology towards nanotechnology is daily demonstrated by the successful fabrication of micro- and nanodevices which are employed in a large variety of industrial, consumer, and biomedical applications. Nanotechnology encompasses the production of physical, chemical, and biological systems at scales ranging from individual atoms to submicron dimensions, as well as the integration of nanostructures into larger scale systems. Research in nanotechnology constantly affords to the community actual breakthroughs in several areas such as materials and manufacturing, electronics, medicine and healthcare, energy, biology and biotechnology [2]. Semiconductor industry has especially distinguished itself as “the leader” in terms of innovation and improvement in its products. Integration, cost, speed, power consumption, compactness and functionality have been the basis concepts on which all the R&D programs in this field were based so far. However, the actual driving force of this constant evolution, as well explained by the Moore’s Law, has always been the strong desire of miniaturization of the device dimensions in order to allow a consequent increase of the device density per area. In this respect, several semiconductor companies have already started to transfer their products from the 8” (200 mm) to the 12” (300 mm) wafers. The 12” wafers used today can yield 2.25 times more chips per wafer than older ones thus significantly boosting total monthly output. Following the Moore’s law has been the leading trend for the past 30 years and the predicted goals have been actually achieved in terms of device dimension, density and performances. In order to make such an evolution possible, some technological and scientific issues must be carefully addressed. The scientific community, together with the R&D sections of the semiconductor companies, works on the International Roadmap for Semiconductors (ITRS) providing targets and guides for the future technology nodes [3]. ITRS reflects not only the semiconductor industry evolution on the continued scaling of the CMOS technology (*more Moore*) but it also addresses post-CMOS devices and a wide range of different systems (*more than Moore*) Figure 1.1.

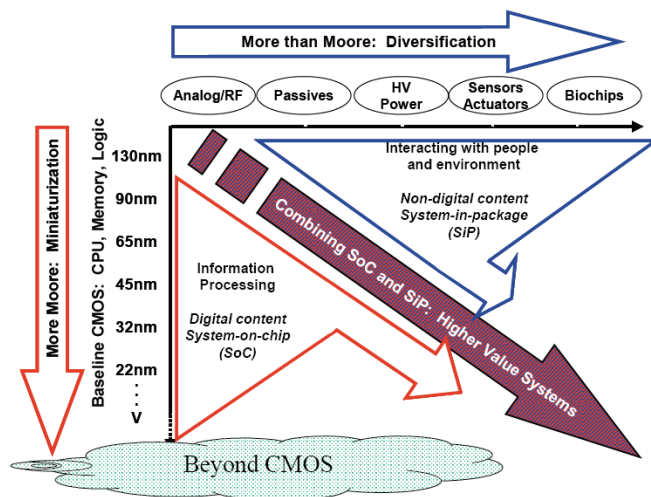


Figure 1.1: Device miniaturization (*more Moore*) and diversification (*more than Moore*) in future advanced micro- and nanoelectronics.

Scaling along the *more Moore* path is feasible following two approaches:

- ❖ Geometrical Scaling, thus shrinking the horizontal and vertical physical feature sizes of the logic or memory device parts
- ❖ Equivalent Scaling, which occurs in conjunction with the Geometrical Scaling, thus improving devices structure and technology and employing new materials

In order to pursue this technological revolution, a continuous improvement of the industrial CMOS process flow and of the related technologies is needed [4,5,6]. As far as the introduction of new materials is concerned, a main issue is represented by the search and the development of a suitable deposition technique. In fact, the CMOS process flow employed to fabricate logic chips, capacitors, and memory devices actually demands a great amount of thin films depositions. Thin films technology plays a very important role for the evolution of the micro- and nanoelectronic industries. For example, the gate oxide of the MOSFETs and several layers of a DRAM or NVM stack are thin films (10-50 nm) which have to be deposited with an extremely accurate thickness and composition control. There are several physical vapor deposition techniques (i.e. sputtering, thermal or e-beam evaporation) that are currently employed to deposit materials for selected applications. However, chemical vapor deposition (CVD) is preferred for other specific applications. Amongst the CVD techniques, ALD is currently considered the most promising solution for the growth of ultra-thin, conformal and stoichiometric oxide, nitride and metal films [7].

ALD offers outstanding advantages, compared to CVD, in term of sub-nanometric film thickness control. Furthermore, ALD allows depositing ultra-thin films in high aspect ratio structures and it suitably covers any kind of geometric profile. Nowadays ALD is already and successfully employed for the growth of thin films in several industrial applications [8,9].

In order to pursue the Geometrical or the Equivalent Scaling, a key role is played by the choice of the material with respect to its specific final application. The scaling can be indeed accompanied by the rise of unexpected drawbacks [10,11]. For the fabrication of the new generation of microprocessors, the thickness of the SiO₂ transistor's gate oxide has scaled from 100 nm down to 1.2 nm. At this low thickness the oxide does not guarantee its effective dielectric properties. Indeed, being SiO₂ thickness extremely scaled down, the expected bulk dielectric properties are lost and, consequently, a quantum mechanical electron tunneling through the layer generates unacceptable current flows throughout the oxide layer during MOSFET operations [12,13]. Leakage current is indeed the major problem when the thickness of a SiO₂ gate oxide is drastically reduced to only few nm. Semiconductor industry started many years ago in looking for a proper substitute for SiO₂. So far, the most feasible solution is represented by the introduction of high dielectric constant (k) materials as a replacement of SiO₂ [14,15,16,17,18]. These oxides (e.g. Al₂O₃, ZrO₂, HfO₂, La₂O₃) are characterized by elevated permittivity values which are associated to their polarizability inside an electric field. Compared to SiO₂, a high- k dielectric can provide an increased capacitance for the same physical thickness or, alternatively, the same capacitance for an increased physical thickness (Figure 2.2) [19].

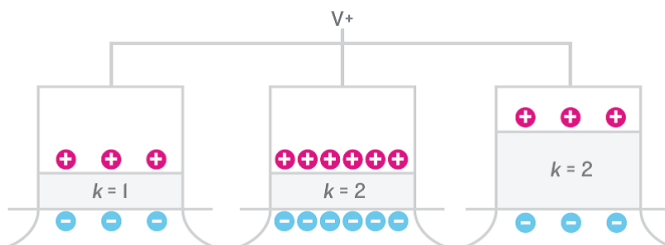


Figure 2.2: The dielectric constant k is a measure of an insulator's ability to concentrate an electric field. If one gate oxide has twice the k of another, a given voltage will draw twice as much charge into the transistor channel. Or, the same amount of charge will accumulate, if the high- k dielectric is made twice as thick.

High- k materials were demonstrated as the effective solution to fabricate transistors characterized by a 10 times lower leakage current values associated to comparable or even better device performances [20,21]. Currently, an Hf-based high- k gate oxide material is used in the post-45 nm transistors production by a semiconductor industry [22,23]. High- k materials are employed, in most of the cases,

as dielectrics inserted in capacitor structures. The gate capacitance (C_{ox}) in a parallel plate capacitor is expressed as:

$$C_{ox} = \frac{k_0 k_{ox} A}{t_{ox}}$$

where k_{ox} is the permittivity of the dielectric, k_0 is the permittivity of the free space, A is the area of the capacitor and t_{ox} is the dielectric thickness. To compare the electrical performances of a high- k material with SiO_2 it is introduced the concept of Equivalent Oxide Thickness (EOT).

$$EOT = \frac{k_{\text{SiO}_2}}{k_{\text{high-}k}} \cdot t_{\text{high-}k}$$

EOT is defined as the equivalent theoretical thickness of SiO_2 that would be required to achieve the same capacitance density achieved using a high- k dielectric [13]. For example, replacing SiO_2 ($k = 3.9$) with a 10 nm thick high- k oxide which displays a k value 10 times higher than SiO_2 (i.e. $k = 39$) allows to achieve an EOT of 1 nm. This means that it is possible to obtain the same gate capacitance drastically reducing the undesired leakage currents due to an increase of the physical thickness of the dielectric. On the other hand, as previously mentioned (see Figure 2.2), it is also possible to obtain an increased gate capacitance keeping the high- k thickness fixed. In order to provide a common figure of merit even amongst different technologies, ITRS establishes every year the EOT target values that should be achieved depending on the applications; thus guiding the applied research on the high- k materials. However, a dielectric should satisfy a number of requirements; amongst them it is worth mentioning also the band offset against the semiconductor substrate. In particular, an adequate conduction band offset ensures the minimum leakage current; i.e. on Si it should be at least 1 eV. Due to the fact that there is an inverse dependence of k on band gap [17], the employment as gate oxide of ultra high- k dielectrics is intrinsically problematic. The development and integration of novel high- k materials necessarily requires a thorough investigation of the structural and chemical properties of the dielectrics [24]. Different crystalline phases or oxide stoichiometries has to be correlated with the dielectric properties of the material [25,26,27]. Concomitantly, interface engineering represents a major issue that has to be carefully addressed [28]. Indeed, the formation of an interfacial layer (IL) between the dielectric and the underlying semiconductor substrate may directly affect the electrical properties of the stack and thus the electrical performances of the final device [29]. Hence, depending on the final application, the high- k dielectric must to be deposited and engineered with certain specifics as discussed for few examples in the following sections. Process integration and Front End processes challenges related to the evolution of logic and memory technologies can be well understood by looking at the extremely different requirements that the ITRS has updated in its 2008 overview document [3]. In the following three tables, referred to three kinds of semiconductor technologies, the **white** cell background means that manufacturable solutions already exist and are being optimized, **yellow** means that manufacturable solutions are known and **red** means that manufacturable solutions are not known yet.

High performance logic MOSFET requirements

For the evolution towards high speed and low power MOSFETs and for the scaling beyond the 45 nm technology generation thin high- k dielectric films will be required to be employed as gate oxide. In Table 1.1 the EOT and leakage current densities targets for the forthcoming nodes are reported.

Table 1.1: High performance logic requirements. Source ITRS Update 2008 [3].

| <i>Year of Production</i> | 2009 | 2010 | 2011 | 2012 | 2013 | 2014 | 2015 |
|--|-------------|-------------|-------------|-------------|-------------|-------------|-------------|
| <i>½ Pitch (nm)</i> | 59 | 52 | 45 | 40 | 36 | 32 | 28 |
| <i>Physical gate length (nm)</i> | 27 | 24 | 22 | 20 | 18 | 17 | 15 |
| <i>EOT (nm)</i> | 1.0 | 0.95 | 0.88 | 0.75 | 0.65 | 0.6 | 0.53 |
| <i>Maximum gate leakage current density (A/cm²)</i> | 650 | 830 | 900 | 1000 | 1100 | 1200 | 1300 |

Non Volatile Memories

Innovation in NVM is associated to the evolution of the existing flash memories technology but also to the study and engineering of new memories solutions. In Table 1.2 are reported the EOT target values proposed for both tunnel and interpoly dielectrics either for NAND or for NOR memory cells. It is worthy to notice that NAND has surpassed CMOS technology in terms of half pitch scaling and is thus now leading the scaling rush.

Table 1.2: NVM requirements. Source ITRS Update 2008 [3].

| <i>Year of Production</i> | 2009 | 2010 | 2011 | 2012 | 2013 | 2014 | 2015 |
|---|-------------|-------------|-------------|-------------|-------------|-------------|-------------|
| <i>NAND Flash poly ½ Pitch (nm)</i> | 40 | 36 | 32 | 28 | 25 | 22 | 20 |
| <i>NOR Flash ½ Pitch (nm)</i> | 50 | 45 | 40 | 35 | 32 | 28 | 25 |
| <i>Flash NOR tunnel oxide EOT (nm)</i> | 8.5-9.5 | 8-9 | 8-9 | 8-9 | 7-8 | 7-8 | 7-8 |
| <i>Flash NAND tunnel oxide EOT (nm)</i> | 6-7 | 6-7 | 6-7 | 6-7 | 6-7 | 6-7 | 6-7 |
| <i>Flash NOR interpoly EOT (nm)</i> | 13-15 | 11-13 | 6-12 | 6-12 | 6-12 | 4-6 | 4-6 |
| <i>Flash NAND interpoly EOT (nm)</i> | 10-12 | 9-11 | 9-11 | 9-11 | 4-6 | 3-5 | 3-5 |
| <i>Tunnel / Interpoly max leakage current at 2 V for 10 years data retention (A×10⁻²³)</i> | 5 | 5 | 2.5 | 2.5 | 1.3 | 1.3 | 1.3 |

DRAM technology

Innovation in DRAM technology is challenging in terms of new device structure and in particular for the necessarily integration of new materials in order to achieve the extremely low EOT targets that are expected for the forthcoming nodes (Table 1.3).

Table 1.3: DRAM requirements. Source ITRS Update 2008 [3].

| <i>Year of Production</i> | 2009 | 2010 | 2011 | 2012 | 2013 | 2014 | 2015 |
|--|-------------|-------------|-------------|-------------|-------------|-------------|-------------|
| <i>DRAM ½ Pitch (nm)</i> | 50 | 45 | 40 | 36 | 32 | 30 | 25 |
| <i>DRAM cell size (µm²)</i> | 0.015 | 0.0122 | 0.0096 | 0.0078 | 0.0061 | 0.0054 | 0.0038 |
| <i>DRAM storage node cell capacitor dielectric: EOT (nm)</i> | 0.8 | 0.6 | 0.5 | 0.4 | 0.3 | 0.3 | 0.3 |

By looking at these extremely different EOT target values that are associated to the forthcoming MOSFET, NVM and DRAM technological nodes, it is possible to better appreciate how challenging and complicated is the task to pursue the device miniaturization and evolution. Scaling of MOSFETs to the 22 nm technology generation presents a particularly challenging issue in the control of the gate oxide k and thickness, in order to achieve sub-nm EOT values, and in the gate oxide coupling with a proper metal gate electrode. The main issue in scaling the high density NVM towards the next generations is represented by the limited scaling of the tunnel and interpoly dielectric physical thickness in order to guarantee charge retention and correct coupling ratio. In DRAM technology, the main issue associated with scaling is the achievement of adequate storage capacitance for devices with reduced size and high aspect ratio, thus including difficulties in implementing ultra high- k storage dielectrics in order to achieve extremely low EOT values.

What clearly turns out from this brief review is that the introduction of high- k dielectrics plays a fundamental role for all the aforementioned different technologies, being currently the only feasible way to accomplish with manufacturable solution. Depending on the EOT target, and thus on the specific technology, novel high- k or even ultra high- k dielectrics are definitely needed by the semiconductor industry for the production of new advanced ultra-scaled nanoelectronic devices. Due to the accurate thickness and dimensional control that is required in all these nanoscale systems, ALD appears as the most promising technique candidate to be employed for the deposition of such a ultra-thin films on large scale area substrates.

Germanium and III-V high-mobility substrates

An extremely important topic is represented by the search of alternative channel materials for the so-called post-Si MOSFET technology. The idea is to find an alternative semiconductor substrate which can be integrated on a Si platform wafer, for the realization of the next generation of nanoelectronic devices. Indeed, an effective way to reduce supply voltage and the resulting power consumption in future ultra-scaled devices, without affecting the electrical performance, is to use high-mobility channels in order to increase the current drive of CMOS [30]. High-mobility materials, such as Ge and III-V compounds, are extremely interesting because of their elevated carrier (electron and hole) mobilities (Table 1.4) compared to Si [31].

Table 1.4: High-mobility semiconductor substrates.

| | Si | Ge | GaAs | InP | InAs | InSb |
|---|------------------------------------|-------------------------------------|-------------------------------------|------------------------------------|------------------------------------|-------------------------------------|
| Electron mobility (cm ² /Vs) | 1600 | 3900 | 9200 | 5400 | 40000 | 77000 |
| Electron effective mass (m_0) | m_t : 0.19 m_l : 0.916 | m_t : 0.082 m_l : 1.467 | 0.067 | 0.082 | 0.023 | 0.014 |
| Hole mobility (cm ² /Vs) | 430 | 1900 | 400 | 200 | 500 | 850 |
| Hole effective mass (m_0) | m_{HH} : 0.49 m_{LH} : 0.16 | m_{HH} : 0.28 m_{LH} : 0.044 | m_{HH} : 0.45 m_{LH} : 0.082 | m_{HH} : 0.45 m_{LH} : 0.12 | m_{HH} : 0.57 m_{LH} : 0.35 | m_{HH} : 0.44 m_{LH} : 0.016 |
| Bandgap (eV) | 1.12 | 0.66 | 1.42 | 1.34 | 0.36 | 0.17 |
| Permittivity | 11.8 | 16 | 12 | 12.6 | 14.8 | 17 |

m_{HH} , mass of heavy holes; m_{LH} , mass of light holes; m_t , transverse effective mass; m_l , longitudinal effective mass.¹⁰

High- k materials for Ge and III-V compounds

However, as already discussed in the previous section on device scaling and high- k dielectrics, finding a high quality gate insulator remains a mandatory task also for alternative semiconductor substrates. Indeed, for both Ge and III-V the removal of the native oxides is a mandatory task due to the poor electrical quality of these dielectrics which are unsuitable for any kind of application into operative devices. As a consequence, the deposition of a high- k dielectric appears as the most feasible solution to concomitantly obtain low EOT values suitable for the technological application of the latter stacks. However, forming a high quality and low defects density oxide/Ge and oxide/III-V interface is a major challenge [32]. The main issue on Ge is connected with the nature of the GeO₂ and to the related poor interface electrical characteristics [33,34]. Indeed, GeO₂ is thermodynamically unstable at about 450 °C; it is soluble in water and presents an unacceptable interface defects density which jeopardizes the electrical properties of the CMOS device. Ge surface passivation after the removal of the native GeO₂ has been largely addressed in literature and several alternative solutions have been taken into account such as the direct deposition of the high- k (as discussed later in this work), the use of intentional interfacial passivating layer (IPL), i.e. GeON or thermally grown GeO₂ or the employment of other surface chemical treatments [35,36,37,38]. As far as the III-V compounds are concerned, the major issue is represented by the surface oxidation which leads to the formation of a high density of intrinsic defects, thus resulting in the so-called Fermi level pinning. As a consequence of that, the modulation through the gate bias of the carrier concentration at the oxide/III-V interface becomes difficult and inefficient. Focusing the attention on the III-As compounds (i.e. GaAs and In_xGa_{1-x}As), it turned out

that to achieve a low interface defects density their surfaces have to be cleaned and passivated prior to the deposition of a high- k dielectric [39]. Differently from Si and Ge, for III-As compounds does not exist a large variety of cleaning processes that can efficiently remove the native oxides leaving at the same time a clean and well ordered atomic surface [40]. In wet cleaning, usually NH_4OH or $(\text{NH}_4)_2\text{S}_2$ solutions are employed to partially remove the native oxides. However, the most efficient surface passivation has been reported for the so-called ALD self-cleaning effect. Trimethyl aluminum, the most common Al precursor used in ALD of Al_2O_3 , nearly reduces all the arsenic oxides providing a fairly good passivation of the $\text{Al}_2\text{O}_3/\text{III-As}$ surface [41,42,43,44].

Recent progresses achieved in Ge and III-V technology suggest that the implementation of high- k dielectrics, together with a proper surface passivation, is a very promising strategy for the combination of the latter high-mobility semiconductor substrates into the next CMOS device generations.

Rare Earth Oxides

Amongst the high- k dielectrics, REOs have lately received extensive attention; in fact there has been a wide interest in RE-based binary or ternary compounds as candidates to be employed in advanced CMOS technology [45]. The RE lanthanide elements, from La (first) to Lu (last), are characterized by various oxide stoichiometries e.g. RE₂O₃, REO or REO₂. Advantages and drawbacks of these RE-based oxides are intimately related to the intrinsic properties of the RE elements, which periodically vary with increasing the atomic number. Indeed, the 4*f* shell is progressively filled (empty in La, full in Lu) along the series while the ionic radius decreases (from 0.123 Å to 0.092 Å). In addition, the number and value of the oxidation states progressively change along the series thus determining different reactivity of the species, i.e. different moisture sensitivity. This periodical variation consequently affects the electronic properties and also the dielectric constant. More specifically, the k value is intimately connected with the fact that REOs show structural polymorphisms. Indeed, the value of the dielectric constant is related to frequencies of its dominant infrared optical modes which in turn are related to the crystalline structure. For example, cubic and hexagonal La₂O₃ crystalline phases are characterized by two different permittivity values of 17 and 26, respectively. In general, the early REOs (until Pr₂O₃) have a predicted stable hexagonal structure. Differently, for the others REOs the cubic (in the bixbyite form) is the most stable; however, also a monoclinic distortion of the cubic might appear [46]. The higher k value is the one associated to the crystalline structures that have the most intense absorption band at lower frequencies. In this respect REOs appears as an extremely promising solution as high- k dielectrics and there is a keen interest in the semiconductor industry in integrating these oxides into new devices. Another important aspect of the REOs, in the light of their potential integration in CMOS technology, is the predicted thermodynamic stability in contact with Si, Ge and III-V compounds. However, it is now clear that stability strongly differs depending on the semiconductors; being also very closely associated to the quality of the REO/substrate interface. In the light of the recent results obtained for REOs deposited with different techniques, there are two major drawbacks associated to the so-called “lanthanide contraction” which in turns are the strong hygroscopicity character and the tendency to form RE-based silicate and germanate species at the REO/substrate interface. In order to address both these issues, the study of REO was recently extended to more complex RE-based compounds. Indeed, an alternative approach can be to consider RE elements as dopant atoms to be included in transition metal oxide matrixes, i.e. ZrO₂ and HfO₂ [47,48,49]. It has been shown from *ab initio* calculations that high-symmetry phases of ZrO₂ and HfO₂ exhibit higher permittivity values. Indeed, k values in the range of ~34-37 for the cubic phase [50,51] and of ~30 for the tetragonal phase of ZrO₂ [50] (~47 in Ref.[51]) were calculated. Therefore, it is desirable to stabilize these metastable crystalline phases. However, the tetragonal and cubic phases are stable only at very high temperatures above 1500 °C. Similarly to the ZrO₂ system, for the HfO₂ system k values in the range of ~26-29 for the cubic phase [50,52] and of ~29 for the tetragonal phase of HfO₂ [50] (~70 in Ref. [52]) were calculated. In both systems, this cubic or tetragonal structure can be stabilized by adding through proper doping an appropriate cation, which allows for the formation of a solid solution. RE-based doping and consequent stabilization of metastable crystalline phases of ZrO₂ and HfO₂ has been already reported in literature [53,54,55,56]

Actually, a twofold approach is followed while performing the doping using a RE element. The potential stabilization of metastable crystalline phases might be accompanied by the possibility to benefit from the large RE ionic radius into the matrix and thus contributing to the dielectric properties. It is still an open question whether the RE atoms actually contribute to the dielectric constant or only contribute to the stabilization of metastable phases.

Outline of the Thesis

The aim of the research activity described in this thesis is to develop and investigate the ALD of REOs on different semiconductor substrates and to characterize and discuss the physical properties of the dielectric thin films as novel materials to be employed in advanced micro and nanoelectronic devices.

The research was carried out in the MDM (Materials and Devices for Microelectronics) national laboratory (<http://www.mdm.infm.it>). MDM belongs to INFM, the Italian Institute for the Physics of Matter which is part of CNR, the National Research Council. The laboratory is located in Agrate Brianza (MI, Italy), inside the STMicroelectronics/Numonyx industrial site. MDM major research activities are focused on investigating the structural, electrical, optical and magnetic properties of materials for present and future nanoelectronics, as well as developing innovative processes and characterization techniques. The scientific staff of the laboratory is composed by senior researchers, post-doctoral fellows and PhD and Master's students. The group has a wide and extensive expertise on the ALD and characterization of high- k dielectrics. Moreover, at MDM several advanced diagnostics are available thus giving the possibility to directly investigate the properties of the novel materials grown in the two ALD reactors which are installed in the clean room (class 1000).

The activity at MDM has been financially supported by the European project REALISE "*Rare earth atomic layer deposition for innovation in electronics*" (<http://www.tyndall.ie/realise>). The project partners were Tyndall National Institute (University College Cork, Ireland), University of Helsinki (Finland), University of Liverpool (United Kingdom), CNR-INFM MDM (Italy), SAFC-Hitech (United Kingdom), ASM Microchemistry, Numonyx (Italy), Qimonda Dresden (Germany), NXP Semiconductors Netherlands BV, CNRS-CEMES, (Toulouse, France). The project started on 01 Mar 2006 and ended on 30 Sep 2009. It was funded by the European Commission and by the project partners under the Sixth Framework Programme, in response to a joint call of the IST and NMP thematic priorities.

Two particularly fruitful collaborations with the partners are worth to be highlighted. Firstly, the intense work carried out together with S. Schamm and P. E. Coulon of the nanomaterials group at CNRS-CEMES in Toulouse (France). This collaboration provided the possibility to integrate all the results obtained at MDM with different expertise in transmission electron microscopy (TEM), particularly high resolution TEM (HRTEM) and electron energy loss spectroscopy (EELS). A cross-correlated characterization has been carried out on selected samples grown by ALD at MDM and shipped to CEMES for a nanoanalytical investigation, especially near interfaces.

Secondly, due to the fact that MDM laboratory is located inside Numonyx site an intense collaboration with the industry is actually possible. This happens in particular within research projects such as REALISE, where the industrial integration and evaluation of novel materials developed in research reactors is required. Indeed, both La- and Er-based films were deposited at MDM on 8" wafers patterned with NVM test structures supplied by Numonyx. Subsequently, the same wafers were processed inside the industrial pilot line of the R2 site in Agrate and then the oxides were electrically tested as interpoly dielectrics for the future generation NVM memories.

In general, the research approach which has been followed during this work can be divided in three main parts. At the beginning of this work, the Savannah 200 ALD reactor (Cambridge Nanotech, Inc.) was just installed. Therefore, the ALD parameters optimization for all the processes has been discussed and analyzed (see Chapter 3 and 4). At the same time, thorough characterizations of the structural, chemical, electrical and optical properties of the different oxides and of the high- k oxide/semiconductor

substrate interfaces have been carried out. The combination of these two activities is well represented by the *in situ* spectroscopic ellipsometry (SE) characterization which has been performed during ALD (see Chapter 6). *In situ* SE diagnostic has been employed to pursue the ALD process parameters optimization and turned out to be an extremely powerful and useful tool in monitoring thin films deposition. However, the most intriguing contribution from this analysis is actually the one related to the study of the very early stages of the ALD growth (0-3 nm).

In this thesis two main groups of binary and ternary REOs are discussed:

- La-based oxides, in Chapter 3
- Er-based oxides, in Chapter 4

ALD of pure binary La_2O_3 was the first process that was extensively investigated. In particular, the attention was focused on the stabilization of the hexagonal La_2O_3 phase. However, for this material major technological issues related to its hygroscopicity were determined. Afterwards, ternary La-based oxides such as LaZrO (La ~25%) and La-doped ZrO_2 (La ~5%) have been considered with the aim to achieve higher permittivity values, through the stabilization of the cubic and/or tetragonal phase of ZrO_2 , together with an acceptable stability upon air exposure. As an alternative to La-based materials, ALD processes for Er-based oxides were developed and the attention was focused on different Er-doped HfO_2 films. The stabilization through Er doping of the high-*k* cubic/tetragonal phase of the HfO_2 has been the main goal of this part of the research.

Some selected materials such as La_2O_3 , La-doped ZrO_2 and Er-doped HfO_2 were also grown and analyzed on Ge(100) for specific applications requiring stacks with high-*k* on high-mobility channels. Structural and electrical peculiarities, specifically related to the direct contact with Ge, were evidenced also through a fruitful wide collaboration with CNRS-CEMES (see Chapter 5). Within the framework of the activity carried out on high-mobility semiconductor substrates, La- ZrO_2 has been also deposited using ALD on GaAs and $\text{In}_x\text{Ga}_{1-x}\text{As}$ with the aim to investigate the effect of different interface preparation on the high-*k* deposition and characterization (see Chapter 5).

The *in situ* SE characterization has been initially employed to optimize all the different ALD processes. Moreover, specifically applied during the early stages of ALD, *in situ* SE provided insights on the interfaces and on the initial growth behavior of several oxides/substrates combinations (see Chapter 6).

In addition to the research carried out at MDM, thermal and in particular plasma assisted ALD of Ru films were studied during a 3 months internship in the “Plasma & Materials Processing” (PMP) group at the Department of Applied Physics of the Eindhoven University of Technology (The Netherlands) under the supervision of Prof. W. M. M. Kessels (<http://www.phys.tue.nl/pmp>) (see Chapter 7).

References

- [1] <http://www.tyndall.ie/projects/realise>.
- [2] Bhushan and Bharat (Ed.), “*Springer Handbook of Nanotechnology*” 2nd rev. and extended ed., ISBN 978-3-540-29855-7 (2007).
- [3] International Technology Roadmap for Semiconductors, <http://www.itrs.net>.
- [4] P. D. Agnello, IBM J. Res.&Dev. **46** (2002).
- [5] Y. Taur, IBM J. Res.&Dev. **46** (2002).
- [6] H. S. P. Wong, IBM J. Res.&Dev. **46** (2002).
- [7] M. Ritala and M. Leskela, “*Handbook of Thin Film Materials*”, **1** Academic Press (2001)
- [8] A. Sherman, “*Atomic Layer Deposition for Nanotechnology*”, Ivoryton Press, ISBN 978-0-9814663-4-7 (2008).
- [9] H. Kim, H. B. R. Lee, W. J. Maeng, Thin Solid Films **517** 2563 (2009).
- [10] S. E. Thompson and S. Parthasarathy, Materials Today **9**, 20 (2006).
- [11] M. Jeong, V. Narayanan, D. Singh, A. Topol, V. Chan, and Z. Ren, Materials Today **9**, 26 (2006).
- [12] A. I. Kingon, J. P. Maria, and S. K. Streiffer, Nature **406**, 1032 (2000).
- [13] G. D. Wilk, R. M. Wallace, J. M. Anthony, J. Appl. Phys. **89**, 5243 (2001)
- [14] B. H. Lee, J. Oh, H. H. Tseng, R. Jammy, and H. Huff, Materials Today **9**, 32 (2006).
- [15] J. P. Locquet, C. Marchiori, M. Sousa, J. Fompeyrine, J. W. Seo, J. Appl. Phys. **100**, 051610 (2006).
- [16] H. Wong, H. Iwai, Microelectr. Eng. **83**, 1867 (2006).
- [17] J. Robertson, J. Appl. Phys. **104**, 124111 (2008).
- [18] D. G. Schlom, S. Guha, and S. Datta, MRS Bulletin **33** (2008).
- [19] M. T. Bohr, R. S. Chau, T. Ghani and K. Mistry, IEEE Spectrum 30-35, (October 2007).
- [20] R. Chau, S. Datta, M. Doczy, B. Doyle, J. Kavalieros, and M. Metz, IEEE El. Dev. Lett. **25**, 408 (2004).
- [21] R. Chau, J. Brask, S. Datta, G. Dewey, M. Doczy, B. Doyle, J. Kavalieros, B. Jin, M. Metz, A. Majumdar, and M. Radosavljevic, Microelectr. Eng. **80**, 1 (2005).
- [22] <http://download.intel.com/technology/silicon/HighK-MetalGate-PressFoil-final.pdf>
- [23] <http://www.intel.com/pressroom/archive/releases/2007/20070128comp.htm>
- [24] B. W. Busch, O. Pluchery, Y. J. Chabal, D. A. Muller, R. L. Opila, J. R. Kwo, and E. Garfunkel, MRS Bulletin **27**, 206 (2002).
- [25] D. G. Schlom and J. H. Haeni, MRS Bulletin **27**, 198 (2002).
- [26] J. Robertson, MRS Bulletin **27**, 217 (2002).
- [27] R. Degraeve, E. Cartier, T. Kauerauf, R. Carter, L. Pantisano, A. Kerber, and G. Groeseneken, MRS Bulletin **27**, 222 (2002).
- [28] V. Misra, G. Lucovsky, and G. Parsons, MRS Bulletin **27**, 212 (2002).
- [29] M. V. Fischetti, D. A. Neumayer, and E. A. Cartier, J. Appl. Phys. **90**, 4587 (2001).
- [30] S. Takagi, T. Irisawa, T. Tezuka, T. Numata, S. Nakaharai, N. Hirashita, Y. Moriyama, K. Usuda, E. Toyoda, S. Dissanayake, and N. Sugiyama, IEEE Trans. Electron Devices **55**, 21 (2008).
- [31] MRS Bulletin, “*Ultimate scaling of CMOS logic devices with Ge and III-V materials*”, **34** (2009).
- [32] R. M. Wallace, P. C. McIntyre, J. Kim, and Y. Nishi, MRS Bulletin **34**, 493 (2009).
- [33] Y. Kamata, Materials Today **11**, 30 (2008).
- [34] K. Kita, T. Takahashi, H. Nomura, S. Suzuki, T. Nishimura, A. Toriumi, Appl. Surf. Sci. **254**, 6100 (2008).
- [35] A. Delabie, F. Bellenger, M. Houssa, T. Conard, S. Van Elshocht, M. Caymax, M. Heyns, and M. Meuris, Appl. Phys. Lett. **91**, 082904 (2007).
- [36] M. Caymax, M. Houssa, G. Pourtois, F. Bellenger, K. Martens, A. Delabie, S. Van Elshocht, Appl. Surf. Sci. **254**, 6094 (2008).
- [37] H. J. Na, J. C. Lee, D. Heh, P. Sivasubramani, P. D. Kirsch, J. W. Oh, P. Majhi, S. Rivillon, Y. J. Chabal, B. H. Lee, and R. Choi, Appl. Phys. Lett. **93**, 192115 (2008).
- [38] A. Molle, S. Spiga, and Marco Fanciulli, J. Chem. Phys. **129**, 011104 (2008).
- [39] M. Houssa, E. Chagarov, and A. Kummel, MRS Bulletin **34**, 504 (2009).
- [40] Z. Liu, Y. Sun, F. Machuca, P. Pianetta, W. E. Spicer, R. F. W. Pease, J. Vac. Sci. Technol. B **21**, 1953 (2003).
- [41] Y. Xuan, H. C. Lin, and P. D. Ye, IEEE Trans. on El. Dev. **54**, 1811 (2007).
- [42] D. Shahrjerdi, D. I. Garcia-Gutierrez, E. Tutuc, and S. K. Banerjee, Appl. Phys. Lett. **92**, 223501 (2008).

-
- [43] C. L. Hinkle, A. M. Sonnet, E. M. Vogel, S. McDonnell, G. J. Hughes, M. Milojevic, B. Lee, F. S. Aguirre-Tostado, K. J. Choi, H. C. Kim, J. Kim, and R. M. Wallace, *Appl. Phys. Lett.* **92**, 071901 (2008).
- [44] H. D. Lee, T. Feng, L. Yu, D. Mastrogiovanni, A. Wan, T. Gustafsson, and E. Garfunkel, *Appl. Phys. Lett.* **94**, 222108 (2009).
- [45] M. Fanciulli, G. Scarel (eds.), “*Rare earth oxide thin films: growth, characterization, and applications*”, Topics in Applied Physics vol. 106, Springer, Berlin (2007).
- [46] A. Molle, C. Wiemer, Md. N. K. Bhuiyan, G. Tallarida, M. Fanciulli, G. Pavia, *Appl. Phys. Lett.* **90**, 193511 (2007).
- [47] C. K. Lee, E. Cho, H. S. Lee, C. S. Hwang, and S. Han, *Phys. Rev. B* **78**, 012102 (2008).
- [48] D. Fischer and A. Kersch, *Appl. Phys. Lett.* **92**, 012908 (2008).
- [49] D. Fischer and A. Kersch, *J. Appl. Phys.* **104**, 084104 (2008).
- [50] G. M. Rignanese, X. Gonze, G. Jun, K. Cho, A. Pasquarello, *Phys. Rev. B* **69**, 184301 (2004).
- [51] X. Zhao and D. Vanderbilt, *Phys. Rev. B* **65**, 075105 (2002).
- [52] X. Zhao and D. Vanderbilt, *Phys. Rev. B* **65**, 233106 (2002).
- [53] C. N. Ginestra, R. Sreenivasan, A. Karthikeyan, S. Ramanathan, and P. C. McIntyre, *Electrochem. Solid-State Lett.* **10**, B161 (2007).
- [54] C. Adelman, V. Sriramkumar, S. Van Elshocht, P. Lehnen, T. Conard, and S. De Gendt, *Appl. Phys. Lett.* **91**, 162902 (2007).
- [55] S. Ramanathan, A. Karthikeyan, S. A. Govindarajan, and P. D. Kirsch, *J. Vac. Sci. Technol. B* **26**, L33 (2008).
- [56] C. Dubourdieu, E. Rauwel, H. Roussel, B. Holländer, M. Rossell, G. Van Tendeloo, S. Lhostis, S. Rushworth, *J. Vac. Sci. Technol. A* **27**, 503 (2009).



Chapter 2

Experimental

Introduction

This chapter introduces the two main techniques that are discussed in this research work: atomic layer deposition and spectroscopic ellipsometry. Atomic layer deposition is the chemical growth technique which has been employed to deposit all the materials discussed in this work. Spectroscopic ellipsometry is a non-destructive optical characterization technique which is extremely useful for the evaluation of film thickness and optical constants and that was employed during this work either *ex situ* or *in situ* during the deposition. In addition, all the main diagnostics which were employed to analyze the dielectric films prepared by atomic layer deposition are briefly introduced. X-ray diffraction and reflectivity were employed to determine film thickness and its crystalline phase. Moreover, X-ray reflectivity has been powerfully combined with spectroscopic ellipsometry for the thickness determination in multilayer stacks and in particular for the investigation of the formation of an interfacial layer between the high- k oxide and the semiconductor substrate. As far as the chemical characterization is concerned, time of flight secondary ion mass spectroscopy provided useful information about the bulk composition of oxide layers but was also employed to detect the formation of interfacial layers. On the other hand, X-ray photoemission spectroscopy was mainly employed in the analysis of ultra thin layers in order to have the possibility to determine the nature of the chemical bonds present at the interface.

As already mentioned, a complementary detailed nanocharacterization of the interfaces was possible thanks to the collaboration with CEMES in Toulouse. Topographic, structural and chemical description from the nanometric to the atomic scale of high- k REO-based thin films deposited on Si(100) and on Ge(100) was performed using transmission electron microscopy techniques. Beyond the complete description of the different layers in the stack and of the interface with the semiconductor substrate, these results were always correlated with the MDM structural, chemical and electrical considerations. The dielectric properties of the oxides were probed by means of a thorough electrical characterization. MOS capacitors were prepared in order to evaluate, by means of capacitance-voltage and conductance-voltage characteristics, the EOT and the k value of the oxide, the performances in terms of leakage current and eventually the interface defects density.

Atomic Layer Deposition

Atomic layer deposition (ALD) [1] is a growth technique which belongs to the chemical vapor deposition (CVD) group but differs from the conventional CVD for several reasons. ALD is indeed based on the use of separate self-limiting chemical reactions thus completely avoiding any kind of vapor phase reactions. This technique allows depositing ultra thin oxide or metal films with an extremely accurate sub-nanometer thickness control. The films that are deposited by ALD display an excellent conformality and uniformity. Moreover, ALD can be performed at relatively low temperatures if compared to the standard CVD processes thus significantly enlarging the range of applications. ALD was invented by Suntola and Antson in the 1970's and was originally called atomic layer epitaxy [2]. They developed the technique targeting the deposition of thin semiconducting and insulating layers (e.g. ZnS:Mn and AlTiO) for the realization of large-area flat panel displays. Over the years, ALD has gained an enormous consideration in the research and development sections of thin films deposition. Nowadays, ALD is already employed by semiconductor industry to deposit several kinds of materials. Moreover, it can be certainly considered amongst the most promising growth techniques that might be adopted for the realization of the next generation advanced devices for disparate applications e.g. nanoelectronic, micro-electro-mechanical-systems, photonic, photovoltaic or biology [3,4,5]. ALD has been widely employed and investigated to deposit oxides [4,5,6,7,8]; in addition a large amount of nitrides and metals can also be grown using ALD [4,5,26,9]. In this case, it might be preferable to introduce a reductive agent such as H₂ or NH₃. It is well established now that the alternative configuration to thermal ALD, plasma assisted ALD, represents a very good solution to deposit nitride or metal thin films [10,11,12]. ALD is based on the use of self-limiting chemical reactions which occur between the molecules of a vapor phase precursor and the active chemical groups that are present on a surface [13,14,15,16]. These chemical reactions can be activated simply through thermal energy supplied to the substrate; this is the case of the most common thermal ALD configuration which is also the main subject of this work. However, there is an alternative approach of supplying energy to the substrate which is nowadays widely investigated. This is the plasma assisted ALD; in this case the reactant species of the second half of the ALD cycle are generated in a plasma environment [17,18,19,20]. An ALD cycle (Figure 2.1) is composed by four separate steps.

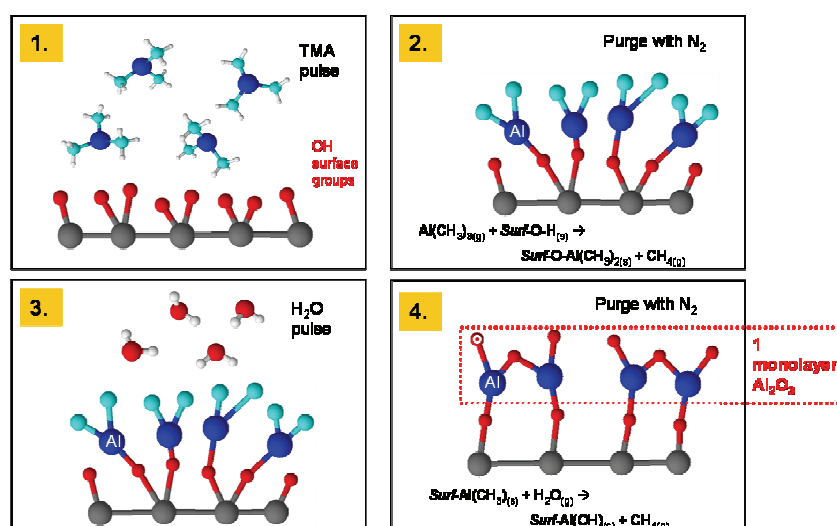


Figure 2.1: Four steps of one ALD cycle of the TMA and H₂O process.

During the first step molecules of a precursor are injected in the reaction chamber such as they can chemically react with the available groups present on the surface. The principle of ALD is to work with self-limiting reactions, therefore, an excess of precursor can be supplied without affecting the reaction mechanisms. The second step, which concludes the first half cycle, consists of a purging of the reaction chamber by means of an inert gas (N_2 , Ar). In this way all the reactions by-products and all the excess of precursor are removed and pumped away. The second half of the ALD cycle is based on a second self-limiting chemical reaction between the molecules of another precursor and the new groups present on the surface. Another purging step concludes the ALD cycle, removes all the volatile reactions by-products and the excess of precursor present in the chamber. After one full ALD cycle, a single monolayer of material is formed on the substrate and the chemical surface groups are similar to those present at the beginning of the deposition. For this reason, ALD cycles can be repeated in a long sequence thus obtaining the formation of a desired number of monolayers and consequently of a film with a precise thickness which is simply function of this number of cycles. Every ALD process is characterized by a peculiar growth rate which depends mainly on the deposition temperature and on the precursor's combination while it should be in principle independent from the dose of reactants. Pursuing the development and the optimization of an ALD process there are three parameters/conditions that have to be investigated, verified and controlled. The first mandatory condition that has to be verified is the so-called pulse saturation. The growth rate of the process must be stable regardless of the dose of gas injected inside the reactor. This means that a saturation curve can be built, which shows that the growth rate, initially low due to under-dosing condition, can be stabilized increasing the dose of precursor up to a situation where the reactant is used in conditions of reasonable dosing excess (Figure 2.2). However, it must be remarked that for excessively long doses the self-limiting behavior might be lost due to partial desorption of the surface groups. The saturation can be easily and efficiently monitored and verified by means of *in situ* SE measurements performed in different growth conditions (see Chapter 6).

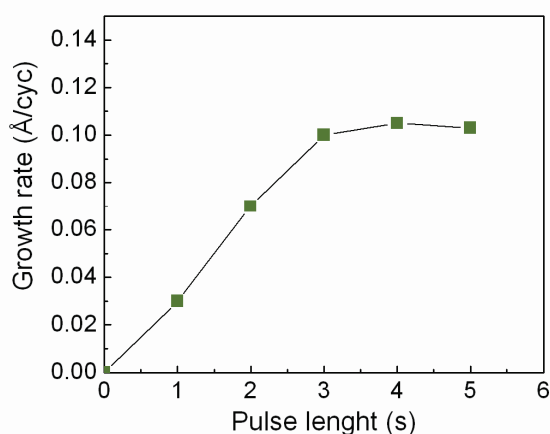


Figure 2.2: Pulse saturation curve. In this example the growth rate appears stable for a precursor pulse which is longer than 3 s.

Another extremely important parameter that must be carefully investigated in ALD is the growth (or deposition) temperature (T_g). Indeed, a real ALD process occurs only when the deposition temperature is placed within a precise range of values which has been identified as the “ALD window” (Figure 2.3). In thermal ALD this window corresponds to the range of T_g in which the growth rate of the process results fairly stable within the experimental error. However, it is worth mentioning that many ALD processes are fully determined by the surface density of species (i.e. OH group density) and when this density is temperature-dependent (e.g. due to dehydroxylation) the growth per cycle is also temperature-dependent. For T_g values out of this particular range, additional undesired chemical and physical

phenomena affect the ALD process and become detrimental for the film growth. Excessively low T_g might either lead to higher growth rates due to condensation of the precursor or to lower growth rates due to the insufficient thermal energy supplied to the molecules. On the other hand, excessively higher T_g might either lead to higher growth rates caused by the raise of thermally promoted gas phase reactions or to lower growth rates due to the partial decomposition of the precursor molecules. Usually ALD processes are developed in the 50–400 °C temperature range.

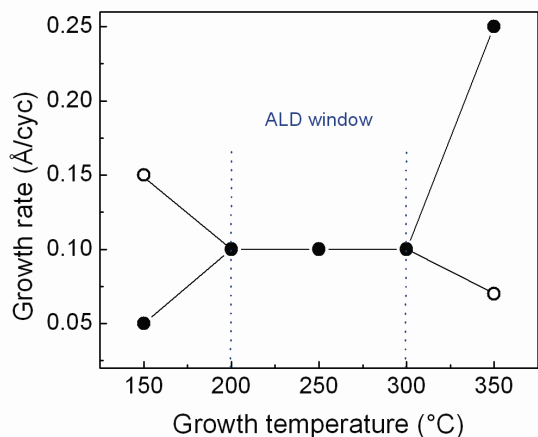


Figure 2.3: Growth rate vs growth temperature: the so-called ALD window.

Once the precursor's dose and the ALD window have been established, for an ALD process a linear relationship between the number of ALD cycles and the film thickness must be easily verified (Figure 2.4). If the growth rate is stable and the film deposition occurs uniformly on the substrate surface, by means of ALD it is possible to deposit films of every thickness. In particular, it is possible to realize extremely uniform and conformal ultra thin films which can even be only 1-2 nm thick.

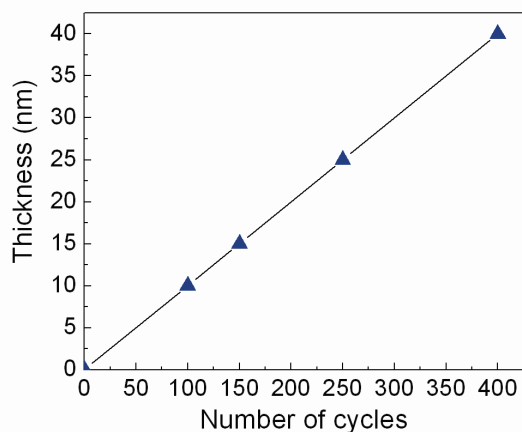


Figure 2.4: Linear plot of film thickness vs number of ALD cycles.

An extremely important role in ALD is played by the precursor's choice. Nowadays, a wide selection of suitable chemical compounds is available on the market [21,22]. The research in this field has made considerable progresses in the recent few years coming up with a lot of novel reactants which has consequently broadened the possibility of the research on materials grown with ALD. The most important physical and chemical features of a suitable ALD precursor are listed below [1,23,24]:

- good thermal stability in vapor phase
- good thermal stability at T_g within the ALD window
- good volatility
- high purity

The most common organometallic precursors are the β -diketonate, halide, alkoxide, amidate and of the cyclopentadienyl complexes [25,26,27]. However, chemical engineering performed on this kind of relatively simple molecules lead to the development of the modified cyclopentadienyl. These compounds present more volatility and therefore higher vapor pressure at the ALD operative conditions. Completely different kinds of reactants have been therefore obtained, making possible the growth via ALD of extremely novel compounds.

Nowadays, there are many kinds of commercial reactors available [28,29,30,31,32,33] and most of the reactors are flow type systems. However, there are differences in the flow dynamic and thus in how the precursor gas is supplied into the reaction chamber. The system which has been used for this research work is a Savannah 200 ALD reactor (Figure 2.5) from Cambridge Nanotech Inc. [28]. It is a flow type reactor with an 8" reaction chamber; there is a single gas injection point and a single outlet through which the reaction gases are pumped continuously. This single injection point might cause directional thickness non-uniformities due to the fact that the gas flow is extremely directional atop the substrate.



Figure 2.5: The ALD reactor Savannah 200.

In order to address this possible drawback, most of the new ALD reactors are equipped with a shower head injector which improves a lot the gas distribution and consequently reduces this undesired non-ideal effect. Some of the films that are discussed in this Thesis were grown in a flow type F-120 ALD reactor (ASM Microchemistry Ltd. [32]).

Spectroscopic Ellipsometry

Spectroscopic ellipsometry (SE) is an optical technique which is nowadays widely used by the semiconductor industry to perform the accurate monitoring and control of thin films deposition steps which are present within the CMOS technology process flow. In fact, it allows checking, in a very fast and non-destructive way, thickness and optical properties of materials. Upon the analysis of the change of polarization of light, which is reflected off a sample, ellipsometry can yield information about layers that are thinner than the wavelength of the probing light itself, even down to fraction of monolayers. Ellipsometry can probe the complex refractive index, which gives access to fundamental physical parameters and is related to a variety of sample properties, including morphology, crystal quality and even chemical composition or electrical properties. It is commonly used to characterize film thickness for single layers or complex multilayer stacks ranging from a few Å or tenths of nm up to several μm with an excellent accuracy. SE can employ broad band light sources, which cover a certain spectral range in the infrared, visible or ultraviolet spectral region. By that the complex refractive index in the corresponding spectral region can be obtained, thus giving access to a large number of fundamental physical properties [34,35,36,37,38]. *Ex situ* SE analysis can quickly provide films thickness and therefore it turns out to be an excellent tool for developing and optimizing the deposition processes. Ellipsometry is based on the analysis of the polarization state of a beam of light that is emitted by a lamp, linearly polarized by a polarizer and then falls onto a sample. After reflection the beam light passes a second polarizer, which is called analyzer, and falls into the detector. For an SE measurement the angle of incidence is equal to the angle of reflection. The nature of the polarization change of the light is determined only by the sample's properties such as thickness and optical constants. Light, which is polarized parallel or perpendicular to the plane of incidence, is called *p* or *s* polarized, respectively. SE measures two parameters, which are conventionally denoted by Ψ and Δ . The polarization state of the light incident upon the sample may be decomposed into the *s* and a *p* component (the *s* component is oscillating perpendicular to the plane of incidence and parallel to the sample surface, and the *p* component is oscillating parallel to the plane of incidence). The amplitudes of these components, after reflection and normalized to their initial value, are denoted by R_s and R_p , respectively. SE actually measures the ratio of R_s and R_p , which is described by the fundamental equation of ellipsometry:

$$\rho = \frac{R_p}{R_s} = \tan \Psi \cdot e^{i\Delta}$$

$\tan \Psi$ and Δ are the amplitude ratio and the phase shift (difference) upon reflection, respectively. Since SE is measuring the ratio of the two latter values rather than their absolute values, it is very robust, accurate, and reproducible. SE is indeed an indirect method; in general the measured Ψ and Δ cannot be converted directly into the optical constants of the sample and a model analysis must be carefully performed. In all other cases a layer model must be established, which considers the optical constants and thickness parameters of all individual layers of the sample including the correct layer sequence. The sample is assumed to be composed by a certain number of discrete and defined layers that are optically homogeneous, isotropic, and must not fully absorb the light. By using an iterative procedure (least-squares minimization) unknown optical constants and/or thickness parameters are varied, and Ψ and Δ values are calculated. The calculated Ψ and Δ values, which match the experimental data best, provide the optical constants and thickness parameters of the sample. A comparison of the experimental and modeled data is shown in Figure 2.6. In order to quantify how well the data generated by the optical model fit, and thus agree, with the experimental measured Ψ and Δ spectra it is introduced the concept of Mean Squared Error (MSE) value. Basically, the MSE sums over all the SE wavelengths the differences between the experimental and the model data. The lower is the MSE value, the better is the agreement between the experimental and model generated SE data [39,40].

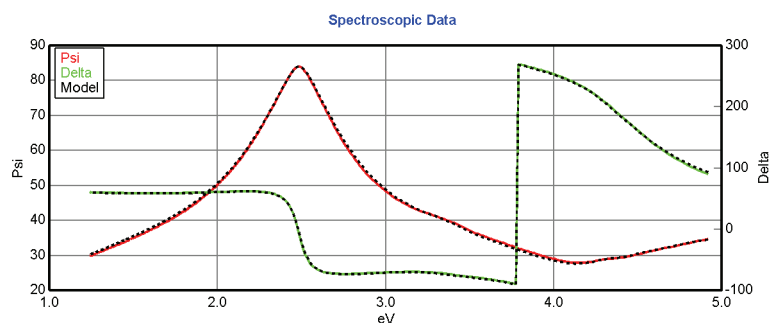


Figure 2.6: Ψ and Δ SE spectra. Experimental (red and green) and model curves.

***In situ* spectroscopic ellipsometry**

In this study the ALD reactor was properly modified in order to perform *in situ* SE measurements directly during the ALD experiments. A new reactor lid equipped with two small windows was designed together with the manufacturers Cambridge Nanotech and J. A. Woollam (Figure 2.7). In this configuration, SE is an even more powerful diagnostic that can be employed to characterize the growth and the properties of a material neither breaking the vacuum nor changing the deposition conditions. Being capable of measuring ultra thin films with thicknesses down to few monolayers, *in situ* SE is capable to provide information that can be used to study the growth rate per cycle during the early stages of the deposition, nucleation or interfacial layer formation effects [41,42,43,44].

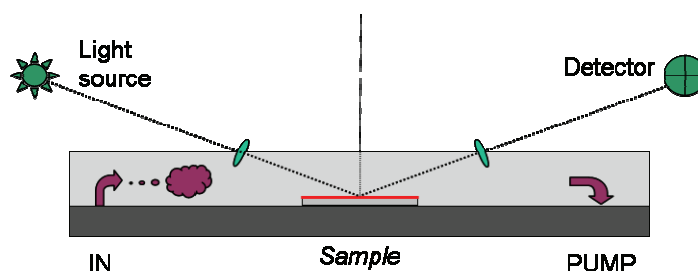


Figure 2.7: Sketch of the *in situ* SE setup mounted on the ALD reactor.

The ALD-SE setup configuration is characterized by:

- ❖ 2 quartz windows
- ❖ SE light beam angle of incidence 70°
- ❖ SE energy range 1.0 – 5.0 eV

In situ SE monitoring turned out to be very useful during the development and the optimization of the different ALD processes. Measurements were carried out on different substrates (e.g. Si, Ge) and at several deposition temperatures (80 – 300 °C) and provided unique information on specific process details. A particular focus was dedicated to the investigation of the early stages of the ALD growth. In this respect, *in situ* SE demonstrated and confirmed to be an extremely powerful tool providing singular data on such kind of specific topic.

Characterization Techniques

Several complementary techniques were employed to perform a thorough structural, chemical and electrical characterization of the films grown using ALD.

X-ray reflectivity and X-ray diffraction

Film thickness and crystalline structure were characterized by means of X-ray reflectivity (XRR) and X-ray diffraction (XRD). A parallel beam of Cu K_{α} radiation was used; XRR spectra were collected using a NaI scintillator detector. Grazing incidence (GI) XRD was performed with a curved position sensitive detector (Inel CPS) at an angle of incidence of 1 or 2 degrees [45]. The grazing incidence-wide exit angle configuration used for this work is particularly appropriate for the analysis of thin, polycrystalline films on a substrate, since it allows measuring the maximum volume of the thin film sample, therefore enhancing the signal to noise ratio. The accurate positioning of the (100) oriented substrate in such a way that the beam enters the sample in between the [110] and the [001] directions allows also to minimize the diffracted intensity from the substrate. GIXRD patterns were simulated by Rietveld refinement and the crystallographic phase composition, the lattice parameters, the dimension of the diffracting domains and the presence of preferential orientations are analyzed. XRR analysis provided the film thickness, surface and interfacial roughness and the materials electronic densities with an extreme accuracy. The simulation of the XRR curves was performed by modeling the stack structure with different layers of appropriate thickness, roughness and electronic density and by performing a simulation based on the minimization of the weighted sum of squares, based on the Matrix formalism corrected by a Croce-Névoit factor [45 and references therein]; XRR is well known to be a very accurate technique for the characterization of high- k oxides [46]. In addition, XRR results were always compared with SE analysis and TEM nanoanalysis, in particular for the several cases where a multilayer stack was investigated.

Time of flight secondary ion mass spectroscopy

Secondary ion mass spectrometry (SIMS) is based on the ejection of charged atomic and molecular species from the surface of a condensed phase (liquid or solid) under heavy particle bombardment. The mass/charge ratio (m/e) of the ionized particles emitted from the surface is analyzed by different types of mass analyzers obtaining a mass spectrum. The m/e spectrum supplies information on the chemical composition of the bombarded area. The emission processes induced by ion bombardment include electrons, photons and surface particles. Most of the emitted atoms are neutral but a small fraction is ejected as positive or negative ions. The secondary ion yield is influenced strongly by the type of primary ion and by the chemical environment of the sputtered species. The latter is the well-known matrix effect. For example, the secondary ion yield for the same species can be changed by several orders of magnitude going from an oxidized to a bare surface [47]. Dual beam Time of flight secondary ion mass spectroscopy (ToF SIMS) achieves the highest depth resolution due to the possibility of decoupling the sputtering gun from the analysis gun, thus employing relatively low energies for sputtering. In particular, by using Cs^{+} ions for sputtering, a very high sensitivity can be obtained in negative polarity. The detection limits for numerous elements can be further improved by modifying the surface chemistry of the analyzed material. The negative ion yields can be enhanced by several orders of magnitude by depositing or implanting in the surface of interest highly electropositive elements such as alkali metals. The Cs ions beam has, therefore, become the most commonly used primary ion source for negative secondary ion detection [48]. In this work ToF SIMS was employed to characterize the chemical composition of the oxide films throughout their entire thickness with extremely high depth resolution (<1 nm) and high sensitivity depending on the experimental conditions

and on the chemical species under analysis. ToF SIMS depth profiles herein presented were acquired in negative polarity on an ION-TOF IV instrument using Cs^+ ions at low energy for sputtering and Ga^+ ions at 25 keV for analysis.

X-ray photoemission spectroscopy

Composition of thin films and chemical bonding at the interface between thin films and substrates were investigated by X-ray photoelectron spectroscopy (XPS). XPS analyzing is based on the electronic photoemission from a core level induced by a X-ray beam irradiation. The physical process is schematically represented in Figure 2.8, where a photoelectron from a core level is emitted after interaction with the impinging photon beam thus leaving a core hole in the irradiated atom.

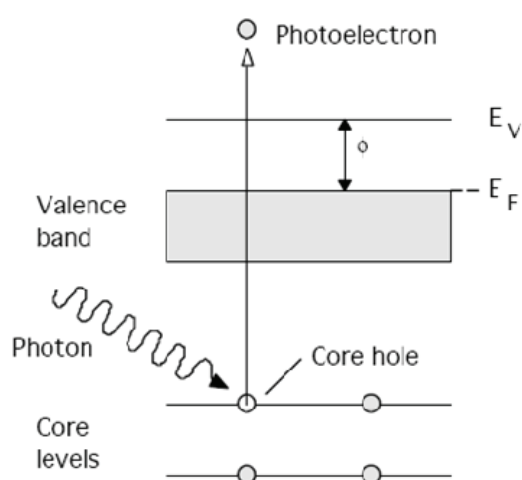


Figure 2.8: Photoemission process: a photon impinges the atom core level, a photoelectron is emitted from the core level thus leaving the atom ionized. E_F , E_V , and Φ are respectively the Fermi level, the vacuum level and the work function of the material under XPS analysis.

The XPS sampling depth is limited by the inelastic mean free path of photoelectrons inside the thin film; i.e. the average length that a photoelectron may cover before losing energy in inelastic scattering. This limitation makes XPS analysis effective only nearby the surface region of the samples, i.e. within a depth of few nanometers [49]. Within this restriction, the sampling depth can be varied by tuning the take-off angle (i.e. the angle formed by the photoelectrons and the impinging X-ray beam). Deeper regions and more superficial regions can be probed in a close-to-normal photoemission configuration ($9\sim 90^\circ$) and for smaller take-off angles, respectively. The X-ray beam is generated by standard Mg K_α (photon energy of 1256.6 eV) or Al K_α source (photon energy of 1486.6 eV). Spectra were recorded at a variable take-off angle by a semispherical analyzer endowed with an energy resolution of 0.6 eV and with an angle acceptance of 8° in the high-resolution mode using a pass energy of 20 eV, an energy step size of 0.05 eV, and a dwell time of 0.5 s. Multiple Voigt function (Lorentzians convoluted with Gaussians) fit was used to interpolate the spectra. Each Voigt function accounts for a single photoemission line component (e.g. the elemental $\text{La } 4d$ line) or for single contributions belonging to the same photoemission line (e.g. the oxidation state components of the $\text{Si } 2p$ line for oxidized Si, i.e. Si^0 , Si^{1+} , Si^{2+} , Si^{3+} , Si^{4+}). The careful deconvolution of the XPS lines as a function of the sampling depth can thus allow for the complete identification of the chemical bonding in the thin film and at the interface level.

Electrical measurements

Room temperature electrical measurements were performed on metal-insulator-semiconductor capacitors fabricated evaporating circular Al dots on the oxide stack. Capacitance-voltage (C-V) and conductance-voltage (G-V) curves were acquired using a Agilent E4980A meter while a HP 4140B pA meter/DC voltage source was used to record current-voltage (I-V) curves. CV characteristics provide a lot of information. From the maximum capacitance value measured when the MOS structure is biased in accumulation, the capacitance equivalent thickness (CET) can be extracted. This allows evaluating the oxide dielectric constant value by considering the slope of the linear fit of the CET dependence vs the oxide thickness. Moreover, the intercept of the fit with y-axis reveals the interfacial layer equivalent thickness. The dependence of the conductance and of the capacitance on the applied voltage and frequency allows determining the density of interface traps (D_{it}). D_{it} was estimated either using the Hill-Coleman method [50] or the conductance method proposed by Nicollian and Goetzberger [51]. The I-V curves allow evaluating the leakage current that is flowing through the gate stack at 1 V above the flat band voltage.

High resolution transmission electron microscopy and electron energy loss spectroscopy

TEM nanoanalysis was fully carried out at CNRS-CEMES by S. Schamm, P. E. Coulon and co-workers [52]. More details can be found in P. E. Coulon's PhD Thesis [53]. Plan view TEM samples and cross-sectional TEM samples (for observations respectively perpendicular and parallel to the film/substrate interface) were prepared by mechanical standard grinding, polishing and minimal Ar^+ ion milling. At a first step, the homogeneity of the films was controlled on the plan-view TEM samples by imaging micrometric areas of the film and also by investigating electron diffraction in order to identify the crystallographic state and structure of the phase present in the films. Then, the local structural and chemical properties at the film/substrate interface and within the film were analyzed by high resolution transmission electron microscopy (HRTEM) and electron energy loss spectroscopy (EELS) on cross-section samples. Experiments were performed with a field emission transmission electron microscope (FEI Tecnai F20) operating at 200 kV and equipped with a spherical aberration corrector that is particularly suitable for atomic structure imaging of interfaces without delocalization of contrasts. For local STEM-EELS studies, a scanning stage allowed to focus and scan a nanometer-sized probe across the film/substrate interface and an EELS spectrometer (Gatan GIF TRIDIEM) was used for the acquisition of EELS spectra at each focused point. From a dedicated quantitative treatment of the EELS spectra [54], elemental profiles of the elements of interest across the film/substrate interface are determined.

References

- [1] M. Ritala and M. Leskela, "*Handbook of Thin Film Materials*", **1** Academic Press (2001).
- [2] T. Suntola and J. Antson, US Patent 4 058 430 (1977).
- [3] M. Ritala, M. Leskela, *Nanotechnology* **10**, 19 (1999).
- [4] A. Sherman, "*Atomic Layer Deposition for Nanotechnology*", Ivoryton Press, ISBN 978-0-9814663-4-7 (2008).
- [5] H. Kim, H. B. R. Lee, W. J. Maeng, *Thin Solid Films* **517** 2563 (2009).
- [6] J. Niinisto, K. Kukli, M. Heikkila, M. Ritala and M. Leskela, *Adv. Eng. Mat.* **11**, 223 (2009).
- [7] J. Paivasaari, J. Niinisto, P. Myllymaki, C. Dezelah IV, C. H. Winter, M. Putkonen, M. Nieminen, L. Niinisto, "*Atomic Layer Deposition of Rare Earth Oxides*" in *Topics in Applied Physics*, Springer Berlin/Heidelberg, vol. 106 "Rare earth oxide thin films", pp 15-32 (2006).
- [8] A. C. Jones, H. C. Aspinall, P. R. Chalker, R. J. Potter, K. Kukli, A. Rahtu, M. Ritala, and M. Leskela, *J. Mater. Chem.* **14**, 3101 (2004).
- [9] B. S. Lim, A. Rahtu, and R. G. Gordon, *Nature Materials* **2**, 749 (2003).
- [10] E. Langereis, S. B. S. Heil, M. C. M. van de Sanden, and W. M. M. Kessels, *J. Appl. Phys.* **100**, 023534 (2006).
- [11] S. B. S. Heil, E. Langereis, F. Roozeboom, M. C. M. van de Sanden, and W. M. M. Kessels, *J. Electrochem. Soc.* **153**, G956 (2006).
- [12] H. C. M. Knoops, A. J. M. Mackus, M. E. Donders, M. C. M. van de Sanden, P. H. L. Notten, and W. M. M. Kessels, *Electrochem. Solid-State Lett.*, **12**, G34 (2009).
- [13] M. Leskela, M. Ritala, *Thin Solid Films* **409**, 138 (2002).
- [14] M. Leskela, M. Ritala, *Angew. Chem. Int.* **42**, 5548 (2003).
- [15] L. Niinistö, J. Päiväsaari, J. Niinistö, M. Putkonen, and M. Nieminen, *Phys. Stat. Sol. (a)* **201**, 1443 (2004).
- [16] R. L. Puurunen, *J. App. Phys.* **97**, 121301 (2005).
- [17] M. de Keijser and C. van Opdorp, *Appl. Phys. Lett.* **58**, 1187 (1990).
- [18] S. M. Rosnagel, A. Sherman, and F. Turner, *J. Vac. Sci. Technol. B* **18**(4), 2016 (2000).
- [19] H. Kim and S. M. Rosnagel, *J. Vac. Sci. Technol. A* **20**(3), 802 (2002).
- [20] S. B. S. Heil, J. L. van Hemmen, C. J. Hodson, N. Singh, J. H. Klootwijk, F. Roozeboom, M. C. M. van de Sanden and W. M. M. Kessels, *J. Vac. Sci. Technol. A* **25**(5), 1357 (2007).
- [21] <https://www.sigmaaldrich.com/safc-hitech/en-us/home.html>
- [22] <http://www.airliquide.com/en/semiconductors/aloha-advanced-precursors.html>
- [23] S. Rushworth, K. Coward, H. Davies, P. Heys, T. Leese, L. Kempster, R. Odedra, F. Song, P. Williams, *Surf. & Coat. Technol.* **201**, 9060 (2007).
- [24] S. Rushworth, H. Davies, A. Kingsley, T. Leese, R. Odedra, *Microelectronics Reliability* **47** 718 (2007).
- [25] C. Musgrave, R. G. Gordon, *Future Fab International* **18**, 126 (2005).
- [26] B. S. Lim, A. Rahtu, J. S. Park, and R. G. Gordon, *Inorg. Chem.* **42**, 7951 (2003).
- [27] S. D. Elliott, *Surf. & Coat. Technol.* **201**, 9076 (2007).
- [28] <http://www.cambridgenanotech.com>
- [29] <http://www.beneq.com>
- [30] <http://www.oxinst.com>
- [31] <http://www.picosun.com>
- [32] <http://www.asm.com>
- [33] <http://www.lesker.com>
- [34] H. G. Tompkins and E. A. Irene, "*Handbook of Ellipsometry*", W. Andrews Inc., New York (2005).
- [35] H. G. Tompkins, *A user's guide to Ellipsometry*, Dover Publications, Inc., Mineola, New York (1993).
- [36] J. N. Hilfiker, C. L. Bungay, R. A. Synowicki, T. E. Tiwald, C. M. Herzinger, B. Johs, G. K. Pribil, and J. A. Woollam, *J. Vac. Sci. Technol.* **21**, 1103 (2003).
- [37] 1st European School on Ellipsometry, "From Fundamentals to Applications in Nanoscience and Nanotechnology", Proceedings Volume, www.nanocharm.org, ISBN:978-3-901578-19-9 (2008).
- [38] K. Vedam, *Thin Solid Films* **313**, 1 (1998).
- [39] J. A. Woollam Co., Inc., 645 M street, suite 102 Lincoln, NE 68508-2243 (USA).
- [40] Guide to using WVASE 32, J. A. Woollam Co., Inc., (www.jawoollam.com).
- [41] J. W. Klaus, A. W. Ott, J. M. Johnson, and S. M. George, *Appl. Phys. Lett.* **70**, 1092 (1997).

-
- [42] E. Langereis, S. B. S. Heil, H. C. M. Knoop, W. Keuning, M. C. M. van de Sanden, and W. M. M. Kessels, *J. Phys. D: Appl. Phys.* **42**, 073001 (2009).
- [43] J. Humlíček, *Phys. Stat. Sol. (a)* **205**, 793 (2008).
- [44] D. Schmidt, S. Strehle, M. Albert, W. Hentsch, J.W. Bartha, *Microelect. Eng.* **85**, 527 (2008).
- [45] C. Wiemer, S. Ferrari, M. Fanciulli, G. Pavia, L. Lutterotti, *Thin Solid Films* **450**, 134 (2004).
- [46] C. H. Russell, *Mat. Res. Soc. Symp. Proc. Vol.* **716**, B1.3.1. (2002).
- [47] Benninghoven, F. G. Rudenauer, and H. W. Werner, *Secondary Ion Mass Spectrometry - Basic Concepts, Instrumental Aspects, Applications and Trends*, vol. 86, John Wiley & Sons, 1987.
- [48] M. L. Yu, Matrix effects in the work-function dependence of negative secondary-ion emission, *Phys. Rev. B* **26**, 4731 (1982).
- [49] D. Brigg and M. P. Seah, *Auger and X-ray Photoelectron Spectroscopy, Practical Surface Analysis*, 1st ed., Vol. 1., Wiley New York (1990),
- [50] W. A. Hill and C. C. Coleman, *Solid-State Electron.* **23**, 987 (1980).
- [51] E. H. Nicollian and A. Goetzberger, *Bell Syst. Tech. J.* **46** 1055 (1967).
- [52] S. Schamm, G. Scarel, M. Fanciulli, “*Local structure, composition and electronic properties of rare earth oxides thin films studied using advances transmission electron microscopy techniques (TEM-EELS)*” in *Topics in Applied Physics*, Springer Berlin/Heidelberg, vol. 106 “Rare earth oxide thin films”, pp 153-177 (2006).
- [53] P. E. Coulon, Ph.D. Thesis “*Films minces d’oxydes à grande permittivité pour la nanoélectronique: organisation structurale et chimique et propriétés diélectriques*”, Université Toulouse III – Paul Sabatier (2009).
- [54] R. F. Egerton, “*Electron Energy Loss in the Electron Microscope*”, 2nd ed. Plenum Press, New York, (1996).

Chapter 3

La-based oxides*

* Results published and to be published as:

G. Scarel, A. Debernardi, D. Tsoutsou, S. Spiga, S. C. Capelli, L. Lamagna, S. N. Volkos, M. Alia, and M. Fanciulli, *Appl. Phys. Lett.* **91**, 102901 (2007).

D. Tsoutsou, G. Scarel, A. Debernardi, S. C. Capelli, S. N. Volkos, L. Lamagna, S. Schamm, P. E. Coulon, M. Fanciulli, *Microelectr. Eng.* **85**, 2411 (2008).

S. Schamm, P. E. Coulon, S. Miao, S. N. Volkos, L. H. Lu, L. Lamagna, C. Wiemer, D. Tsoutsou, G. Scarel, and M. Fanciulli, *J. Electrochem. Soc.* **156**(1), H1 (2009).

D. Tsoutsou, L. Lamagna, S. N. Volkos, A. Molle, S. Baldovino, S. Schamm, P. E. Coulon, and M. Fanciulli, *Appl. Phys. Lett.* **94**, 053504 (2009).

M. Alessandri, A. Del Vitto, R. Piagge, A. Sebastiani, C. Scozzari, C. Wiemer, L. Lamagna, M. Perego, G. Ghidini, M. Fanciulli, *Microelectr. Eng.* **85** in press (2009).

L. Lamagna *et al.*, “*O₃-based atomic layer deposition of hexagonal La₂O₃ on Si and Ge*”, in preparation (2009).

Introduction on La₂O₃

La₂O₃ can be considered, amongst the REOs serie, one of the most promising oxides to be employed as dielectric in advanced micro- and nanoelectronic devices [1]. Indeed, La₂O₃ is expected to be stable in the hexagonal (*h*-) *P6₃/mmc* phase, which has the potential to promote a *k* value significantly higher than the one of the cubic (*c*-) *Ia-3* phase in which most of the RE oxides crystallize [2]. When it is stabilized in the hexagonal phase, La₂O₃ features the highest *k* value (*k* = 27) [3]. Arising from the so-called “lanthanide contraction” La₂O₃ results to be the most hygroscopic oxide of the REOs lanthanide serie [4] exhibiting also the highest affinity for Si atoms [5]. Moreover, despite thermodynamic predictions about the favorable stability of thin REO films on Si(100) [6], these films are found to be unstable. Arguments based on first principles calculations [7] and thermodynamic issues [8] as well as experimental studies [9,10,11,12,13,14] indicate that a thin interfacial layer (IL), which exhibits a rare earth silicate composition, is almost unavoidably formed between the REO film and Si(100). This phenomenon occurs irrespectively of film fabrication and is definitely relevant for the La₂O₃ case. It is worth remarking that an IL of SiO₂ or silicate composition could improve the device performance by preventing electron channel mobility reduction arising from remote phonon scattering [15]. On the other hand, a sharp high-*k* dielectric/Si interface would be preferable from the device point of view because IL formation increases the EOT of the stack.

The whole research conducted on the ALD and physical properties of La₂O₃, which is presented in this chapter, can be divided and discussed in different parts. Several topics were specifically addressed:

- the development of vacuum annealing thermal treatment to obtain the *h*-La₂O₃ phase
- the dielectric properties of the crystalline *h*-La₂O₃ (theory and experimental)
- the stability of the *h*-La₂O₃ phase upon exposure to air
- the effect of the ALD recipe/combination of precursors on the phase obtained in the as-grown films, on the phase obtained upon annealing as well as on the interfacial properties

In particular, it turned out that the use of different ALD recipes leads to the stabilization of the *h*-La₂O₃ in films of variable total thickness. More precisely, the use of O₃ as oxygen source allowed the obtainment of the *h*-La₂O₃ in comparatively thinner films. This trend was explained by performing a detailed structural and chemical investigation of the oxide/substrate interface. The work on the La₂O₃ was concluded by developing an optimized ALD recipe based on the use of La(¹PrCp₃) and O₃ at growth temperature of 200 °C.

In the sections below, few highlights extracted from three publications (Scarel *et al.* [3], Tsoutsou *et al.* [16], Schamm *et al.* [17]) which concern the research work carried out on La₂O₃ films are presented. To conclude the section the chapter dedicated to La₂O₃, a thorough discussion is then dedicated to ALD and characterization of films deposited using the optimized recipe La(¹PrCp₃) and O₃.

Hexagonal La_2O_3 phase: stabilization and dielectric properties

“Vibrational and electrical properties of hexagonal La_2O_3 films” [3]

We managed to obtain $h\text{-La}_2\text{O}_3$ in sufficiently thick films grown on Si(100) in the F-120 ALD reactor using $\text{La}(\text{Cp})_3$ and H_2O at a growth temperature of 260°C . The measured k value turned out to be in well agreement with the one theoretically calculated.

Figure 3.1 illustrates representative 100 kHz C-V curves for 120, 45, and 23.5 nm thick samples processed in vacuum (~ 1 mbar) at 600°C . Accumulation capacitance exhibits non-significant dispersion in the 50-300 kHz range. The 120 nm thick sample with $h\text{-La}_2\text{O}_3$ yields a stack $k = 25 \pm 2$ whereas the 45 nm thick sample, with $c\text{-La}_2\text{O}_3$ crystalline features evidenced by FTIR analysis, a stack $k = 16 \pm 2$. The 23.5 nm thick sample with La silicates exhibits a stack k of $\sim 11 \pm 2$. From a CET versus stack physical thickness plot (Figure 3.1_inset) acquired for samples thicker than 100 nm and processed at 600°C the k value of $h\text{-La}_2\text{O}_3$ films turns out to be 27 ± 3 , in good agreement with the value of 26 derived from our *ab initio* calculations.

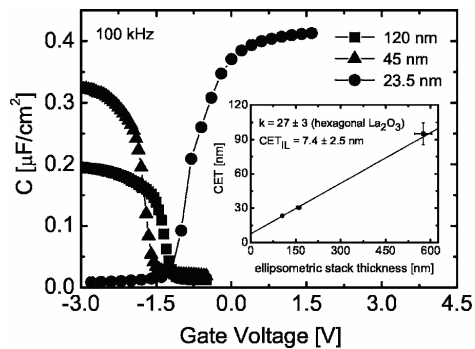


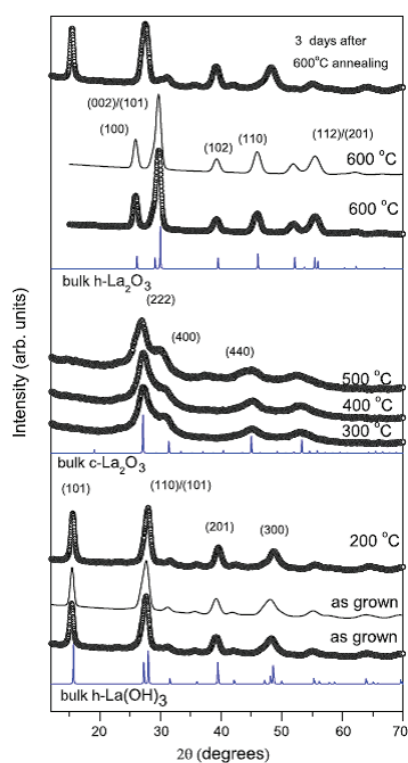
Figure 3.1: 100 kHz C-V curves for 120, 45, and 23.5 nm thick samples processed at 600°C . Inset: CET vs stack physical thickness plot acquired for samples thicker than 100 nm and also processed at 600°C .

In summary, we observed hexagonal $\text{La}(\text{OH})_3$ layers thicker than 100 nm to become $h\text{-La}_2\text{O}_3$ after annealing in vacuum at 600°C . The $h\text{-La}_2\text{O}_3$ films feature a dielectric constant ~ 27 ; in good agreement with *ab initio* calculations and significantly higher than the one of $c\text{-La}_2\text{O}_3$ layers (~ 17).

Crystallographic evolution of La_2O_3 films upon annealing

“Infrared spectroscopy and X-ray diffraction studies on the crystallographic evolution of La_2O_3 films upon annealing” [16]

After the obtainment of $h\text{-La}_2\text{O}_3$ films, we performed a complementary study. We systematically addressed the relation between the annealing process and formation of various La_2O_3 phases. In particular, we aimed at examining the crystallographic evolution of La_2O_3 films upon annealing in the 200-600 °C temperature range. Hygroscopicity, which deteriorates the dielectric properties of the as-grown and vacuum annealed films, was also addressed. La_2O_3 films were deposited in the F-120 ALD reactor on H-terminated Si(100) at 260 °C using $\text{La}(\text{Cp})_3$ and H_2O . The structural evolution upon annealing is shown in Figure 3.2, where the GIXRD patterns of thick (120 nm) La_2O_3 films are presented after annealing at different temperatures. The patterns of as-grown and 600 °C vacuum annealed films are simulated by Rietveld refinement [18]. A polycrystalline structure is established for all samples. As grown and 200 °C annealed samples, are indexed as hexagonal $\text{La}(\text{OH})_3$. The refined lattice parameters of the hydroxide phase in the as grown sample are $a = b = 6.57 \text{ \AA}$ and $c = 3.86 \text{ \AA}$, in agreement with the literature values [19]. The diffraction patterns, recorded following annealing in the 300-500 °C range, unveil the presence of cubic bixbyite $Ia\bar{3}$ La_2O_3 phase [20]. Moreover, after annealing at 600 °C annealing, the hexagonal $P6_3/mmc$ La_2O_3 structure with lattice constants $a = b = 3.93 \text{ \AA}$ and $c = 6.15 \text{ \AA}$ is determined, which is consistent with standard bulk $h\text{-La}_2\text{O}_3$ [21]. It is also important to note that a quick transformation from $h\text{-La}_2\text{O}_3$ into $\text{La}(\text{OH})_3$ occurs due to the H_2O absorption, indicating that the annealed crystalline films are chemically unstable upon exposure to air.



In summary, exposure of La_2O_3 films to air is accompanied by a fast formation of hydrated lanthanum oxide species, namely LaOOH and $\text{La}(\text{OH})_3$. Vacuum annealing in the 300-500 °C range results in the gradual formation of $c\text{-La}_2\text{O}_3$ whereas annealing at 600 °C generates the $h\text{-La}_2\text{O}_3$. Annealed $h\text{-La}_2\text{O}_3$ films were found to be extremely susceptible to moisture absorption.

Figure 3.2: GIXRD experimental spectra (dots) and Rietveld refinements (solid lines) of a 120 nm thick film treated at various annealing temperatures. The diffraction patterns of bulk $h\text{-La}(\text{OH})_3$, $c\text{-La}_2\text{O}_3$ and $h\text{-La}_2\text{O}_3$ are also shown for comparison (in blue).

Structural and chemical properties of $\text{La}_2\text{O}_3/\text{Si}$ interfaces

“Chemical/structural nanocharacterization and electrical properties of ALD-grown $\text{La}_2\text{O}_3/\text{Si}$ interfaces for advanced gate stacks” [17]

In a following study, the local structural and chemical properties of the $\text{La}_2\text{O}_3/\text{Si}$ interfaces and within the film were analyzed by HRTEM and STEM-EELS experiments. Moreover, we investigated the effect of the ALD oxygen source on the interface properties. All films were deposited in the F-120 ALD using $\text{La}(\text{Cp})_3$ as the La source and H_2O and O_3 as the O source. The films were grown on H-terminated Si(100) at a growth temperature of 260 °C [3]; film thickness varied within the 5-35 nm range. The samples were annealed in vacuum for 60 s at 600 °C. All the as-grown films, deposited using H_2O as oxygen source, can be chemically described by a two-layer model. Schematically, this consists of (i) a graded La silicate layer which is silica-rich near the substrate and (ii) a La-based layer. The frontier between the two layers that marks the extent of the interfacial layer (IL) can be defined structurally and chemically with the "chemical" IL thickness being larger than the "structural" one (Figure 3.3).

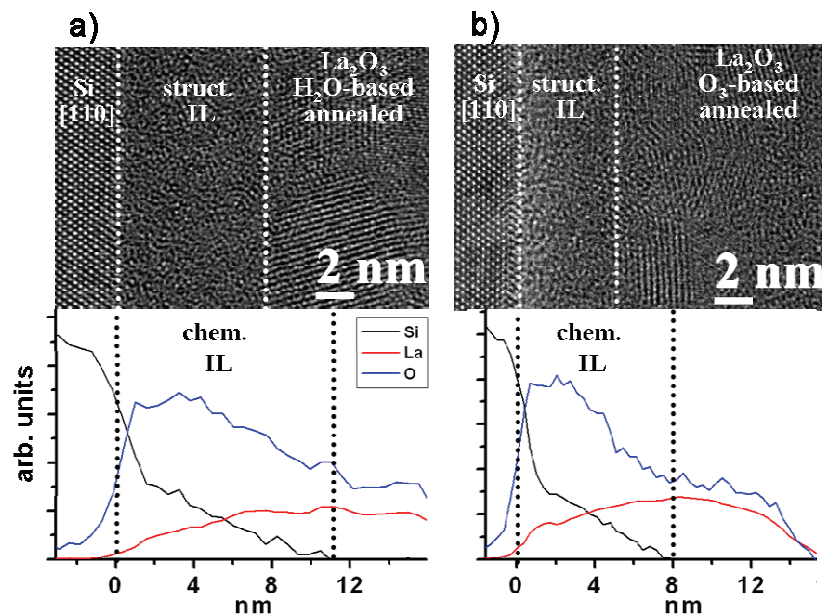


Figure 3.3: HRTEM images near the interface for annealed La_2O_3 films (a) H_2O -based and (b) O_3 -based. Dotted white lines are a guide for the eyes to visualize the borderline between the film amorphous and crystalline parts. Below each HRTEM image is an example of the corresponding EELS elemental ratio profiles across the interface.

Changing the film total thickness in the 7-30 nm range bears nearly no impact on the frontier between the completely amorphous and crystalline parts of the film. Elemental profiles reveal that the Si level becomes negligible only after approximately 8 ± 1 nm away from the substrate. The "structural" IL thickness increases following the thermal treatment. The annealing-induced increase of the "chemical" IL thickness can be understood if we consider that the La_2O_3 films contain adsorbed oxygen species as a result of their exposure to air prior the thermal treatment. Annealing could promote the diffusion of oxygen species towards the interface, therefore, generating an increased IL extent. When $\text{La}(\text{Cp})_3$ is combined with O_3 , significant structural and chemical modifications occur as opposed to oxidation by means of H_2O . Two La-based films, annealed in vacuum for 60 s at 600 °C, are compared to illustrate this point. The first film, which is 24 nm thick, was prepared with H_2O whereas the second one, which is 16 nm thick, was prepared with O_3 . Organization of the dielectric stack for each film is similar (i.e.,

an amorphous IL followed by a nanocrystalline layer). As depicted in Figure 3.3, the "structural" IL thickness is shorter for the O₃-based film (~5 nm) than for the H₂O-based film (~8 nm). Another important modification that is directly visible on the HRTEM images in Figure 3.3 (a) and (b) is that the silica-rich IL is clearly more pronounced for the O₃-based sample (band of clear contrast just above the Si substrate). Additionally, the La/O ratio stabilizes earlier in the O₃-based film than in the H₂O-based one with the relevant transition being more abrupt in the former case. Therefore the "chemical" IL thickness turns out to be ~8 nm for the O₃-based film in contrast to ~11 nm for the H₂O-based one. Note that the as-deposited films have similar structural and chemical IL (respectively 3.5/3 nm and 8/7 nm for the H₂O/O₃ precursors), the IL very near the substrate being Si richer for the O₃-based films than for the H₂O-based one. On the grounds of these results, we propose tentative explanations accountable for the IL formation with the O₃ process compared to the H₂O one. First, since the extent of the silica-rich IL just above the substrate is more pronounced for the O₃-based film, we can suspect that the reaction of O with the Si substrate to form a SiO_x phase is enhanced. This can be well understood because O₃ is a stronger oxidizing agent than H₂O. Secondly, films prepared with H₂O contain a greater amount of hydrogen not only because of the O precursor nature but also because, after exposure to air before the annealing step, H₂O-based films transform more dramatically to La(OH)₃ than O₃-based films. Consequently, we are inclined to believe that H incorporation is favorable to Si and O diffusion through the film and/or La(OH)₃ is more reactive than La₂O₃ towards silicate formation. Moreover, electrical characterization revealed that the average D_{it} measured for a stack grown using the O₃-based recipe is significantly lower than the one derived for the H₂O-based stack. A reason to explain the lower D_{it} value of the O₃-based stacks when compared with H₂O-based ones is that the former interface exhibits, as evidenced from the HRTEM image in Figure 3.3(b), a higher degree of "SiO₂/Si-like" structural order. Taking into account our earlier work [3], which demonstrates that the critical sample thickness required to produce the *h*-La₂O₃ phase in H₂O-based stacks is approximately 100 nm, another improvement gained by the replacement of H₂O by O₃ as the O source in the ALD process is the stabilization of the hexagonal phase in much thinner films since a 30 nm thick stack suffices to generate this phase with the O₃-based process.

In summary, we defined for the La-based films grown using ALD, an amorphous "structural" and a "chemical" IL. The properties of these ILs directly depend on the ALD precursor's combination. When La(Cp)₃ is combined with O₃ instead of H₂O in the ALD process, the properties of the La₂O₃/Si stack are noticeably improved since the specific O source generates a reduced silicate IL thickness, lower D_{it} value and smaller critical sample thickness for the stabilization of the hexagonal La₂O₃ phase.

Atomic layer deposition of La₂O₃ using La(ⁱPrCp)₃

The follow up of the research on ALD of La₂O₃ was initially focused on the test of different La ALD precursors alternatively to La(Cp)₃, which was initially employed. The selection was carried out amongst chemicals belonging to three main classes of La precursor: donor-functionalized alkoxides [La(mmp)₃, La(dmop)₃], β-diketonates [La(thd)₃] and cyclopentadienyl-based compounds [La(MeCp)₃, La(ⁱPrCp)₃] [22,23]. So far, the most effective precursors were identified as cyclopentadienyl-based La complexes. Indeed, the volatility and reactivity of these complexes is directly modified by substitution of the cyclopentadienyl group thus showing an improved precursor vapor pressure and reaction efficiency with the substrates [24,25]. The vapor pressure of La(ⁱPrCp)₃ is indeed higher than that of La(thd)₃ or La(Cp)₃; therefore, a lower source temperature (110 °C) could be used making this precursor a better candidate also for a large scale ALD utilization.

ALD of La₂O₃ was developed in the Savannah 200 ALD reactor using La(ⁱPrCp)₃ as La source and two different oxygen sources, i.e. H₂O and O₃. The growth temperature was varied in the 200-300 °C range.

La(ⁱPrCp)₃ and H₂O

Films deposited using the H₂O-based ALD recipe presented a noticeable and unacceptable thickness non-uniformity, in particular on 8" wafers, regardless of the growth temperature. Thickness non-uniformity (t_{non-un}) was defined as:

$$t_{non-un} = \frac{t_{max} - t_{min}}{2t_{ave}} \cdot 100$$

where t_{max} , t_{min} and t_{ave} are the maximum, minimum and average film thickness, respectively. This effect can be probably explained by referring to the well known hygroscopicity of La₂O₃. Despite in literature the use of this La precursor was already reported in literature in combination with H₂O [26,27], we observed extremely poor process conditions. Indeed, the excess of H₂O contained by definition in the ALD pulses may disturb the self-limiting growth behavior thus requiring excessively long purge times during the process [28]. La₂O₃ is actually reacting with H₂O vapor excess during the deposition giving rise to the immediate formation of La(OH)₃ specie on the surface. As a consequence, H₂O-based ALD of La₂O₃ demonstrated an intrinsic drawback which can be avoided using a different oxygen source like O₃. In addition, a substantial carbon contamination was detected in these films even after annealing at 800 °C. This finding was explained mainly referring to the thermal decomposition of La(ⁱPrCp)₃ molecules which was found to become particularly relevant for growth temperatures above 200 °C. Moreover, the well known tendency of La-based dielectrics to react with atmospheric CO₂ to form carbonates has to be taken into account [29,30]. The *h*-La₂O₃ phase was achieved in these films at a significantly lower critical thickness (~35 nm) than the one observed in the case of films deposited using the La(Cp)₃ and H₂O recipe. However, in this case the as-grown films exhibited a complicated and heterogeneous structural and chemical organization. The stacks can be described by a four layers structure as revealed by HRTEM and STEM-EELS analysis. The structure consists of a sub-nanometric silica-rich interfacial layer followed by an amorphous layer with a silicate-like composition, then a mixed amorphous and nanocrystalline layer rich in La, O and C develops over several nanometer before the films became polycrystalline and mainly composed of La₂O₃.

In summary, the La(ⁱPrCp)₃ and H₂O ALD recipe turned out not to be an ideal and controlled ALD process. Consequently, its development was withdrawn.

La(¹PrCp)₃ and O₃

In very good agreement with our preliminary results (Ref. 17) related to the use of O₃ in ALD of La₂O₃, the process based on this oxygen source turned out to be the most promising amongst the investigated ones. Fairly good film thickness uniformity was achieved on 4” Si wafers and indeed the process was even scaled-up on 8” substrates. In particular, films deposited at 200 °C presented an acceptable thickness non-uniformity <10%. Nevertheless, it must be remarked that such thickness uniformity was lost at higher deposition temperatures. This effect was attributed to the thermal decomposition of La(¹PrCp)₃. The thermal stability of this compound is indeed lower than the one of other compounds being a limiting factor for the selection of the ALD growth temperature. In Table 3.1 a summary of the ALD growth rates and thickness uniformities is reported for both the H₂O-based and O₃-based ALD processes.

Table 3.1: ALD process parameters for La₂O₃.

| Process | T _{La source} (°C) | T _{growth} (°C) | Growth rate (Å/cycle) ± 0.1 | Thickness uniformity |
|---|-----------------------------|--------------------------|-----------------------------|---|
| La(¹ PrCp) ₃ +H ₂ O | 110 | 200 – 250 | 1.2 – 1.5 | Highly non-uniform |
| La(¹ PrCp) ₃ +O ₃ | 110 | 200 | 1.0 | Fairly good t _{non-un} <10% |

It is worth noticing that, as shown in Figure 3.4, a good linear relationship between the ALD number of cycles and the total La₂O₃ film thickness was achieved for the O₃-based process. An average growth rate of ~1.0 ± 0.1 Å/cycle was obtained at a growth temperature of 200 °C.

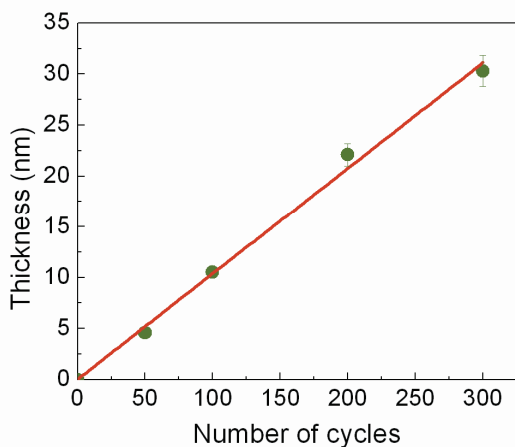


Figure 3.4: O₃-based ALD of La₂O₃. Linear plot of film thickness vs number of ALD cycles.

In the following section the main results obtained for La₂O₃ films grown using the latter optimized ALD recipe [La(¹PrCp)₃+O₃] are reported.

“O₃-based atomic layer deposition of hexagonal La₂O₃ on Si(100)” [31]

We have previously demonstrated that adopting La(Cp)₃ and O₃ instead of La(Cp)₃ and H₂O for the ALD growth of La₂O₃/Si stacks notably improves interface properties through generation of a lower IL thickness and interface trap density with an attendant smaller critical sample thickness for the stabilization of the *h*-La₂O₃ phase [14]. We extend our earlier work by presenting an analysis associated with the ALD growth of thin La₂O₃ films on Si(100) exploiting La(ⁱPrCp)₃ and O₃ as the ALD precursor combination. Particular emphasis is paid to the impact of the above ALD growth strategy upon the *h*-La₂O₃ phase achievement, IL formation and chemistry, La₂O₃/Si interface stability and selective electrical properties following the post-deposition RTA. Data are also discussed in connection to literature ones in order to evaluate the suitability of the proposed ALD recipe for fabricating advanced CMOS transistors with *h*-La₂O₃ as the gate dielectric. All the films were grown in the Savannah 200 ALD reactor on 4” H-terminated n-type Si(100). The H-terminated Si(100) substrates were obtained after RCA (Radio Corporation of America) cleaning (HCl:H₂O₂:H₂O = 1:1:5, 10 min at 85 °C) followed by a 30 s rinse in deionized water and a 30 s dip in a diluted HF solution (HF: H₂O = 1:50, at room temperature). La₂O₃ films were deposited at a growth temperature of 200 °C alternating pulses of La(ⁱPrCp)₃ and O₃; layers thickness was tuned varying the number of ALD cycles. ALD cycle structure was composed of 15 s La(ⁱPrCp)₃ pulse / 8 s purge with N₂ / 0.015 s O₃ pulse / 6 s purge with N₂. La source (supplied by SAFC Hitech) was kept at 150 °C; O₃ was obtained starting from ultra pure O₂ and was injected into the reactor at a concentration of ~ 200 g/Nm³. Film thickness was estimated by SE. In Table 3.2 is reported the list of as-grown and annealed samples discussed.

Table 3.2: Details of as-grown and annealed La₂O₃ films grown on H-terminated Si(100).

| Sample | Stack | Thickness as-grown (nm) | RTA | Thickness after RTA (nm) |
|--------|---|-------------------------|-------------------|--------------------------|
| S1 | <i>n</i> -Si/La ₂ O ₃ | 30.3 | @600 °C in vacuum | 24.7 |
| S2 | <i>n</i> -Si/La ₂ O ₃ | 22.1 | @600 °C in vacuum | 19.0 |
| S3 | <i>n</i> -Si/La ₂ O ₃ | 10.5 | @600 °C in vacuum | 10.4 |
| S4 | <i>n</i> -Si/La ₂ O ₃ | 4.6 | @600 °C in vacuum | 5.4 |

GIXRD analysis is performed on both as-grown and annealed La₂O₃ films in order to address the evolution of the crystallographic structure. Figure 3.5 illustrates GIXRD analysis performed on the 20 nm thick (i.e. sample S2). The as-grown films deposited on Si(100) are mainly amorphous. However, a large bump that might be related to the presence of crystallized hexagonal La(OH)₃ can be clearly identified in the as-deposited state. This finding confirms that, although the measurement was performed immediately after the film deposition, as expected La₂O₃ films grown by ALD are chemically unstable in air and prone to moisture absorption. Given the proved fast conversion to La(OH)₃ upon air exposure, we have decided not to investigate any electrical sample produced using as-grown films. We had previously reported, for samples deposited using a different combination of precursors, that a post-deposition RTA performed in vacuum environment (~1 mbar) promotes the crystallization of the as-grown films into the *h*-La₂O₃ phase [16,30]. In light of this observation, we systematically investigate the effect of this specific thermal treatment and the related evolution of the crystallographic structure of the La₂O₃ samples grown using an O₃-based ALD process.

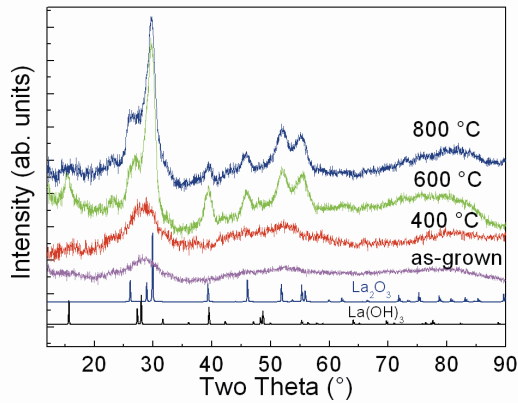


Figure 3.5: GIXRD analysis of 20 nm thick sample after annealing at different temperatures. The powder patterns of hexagonal $\text{La}(\text{OH})_3$ [32] and La_2O_3 [33] are also added for comparison.

The GIXRD spectra of the samples annealed at 400, 600 and 800 °C are shown in Figure 3.5. This study confirms that annealing at 600 °C promotes an almost complete conversion of the amorphous and partially hydroxylated layer into crystalline $h\text{-La}_2\text{O}_3$. The lattice parameters extracted from Rietveld refinement are $a = 3.92 \pm 0.01 \text{ \AA}$ and $c = 6.19 \pm 0.01 \text{ \AA}$, in fairly good agreement with those reported for hexagonal La_2O_3 ($a = 3.94 \text{ \AA}$ and $c = 6.13 \text{ \AA}$ [33]). Further increase of the annealing temperature up to 800 °C does not seem to significantly improve the crystallization of the layer. It is worth noticing that RTA performed at 400 °C already modifies the crystallographic order of the film although a full crystallization is definitely not accomplished in this case. Indeed, because of the fairly low thermal budget, the removal of OH^- groups from the hydroxide layer is not efficient to allow a full structural conversion. Differently from what observed in films grown using the $\text{La}(\text{Cp})_3$ and H_2O ALD recipe, in the 300-500 °C annealing temperature range we do not observe the formation of the cubic La_2O_3 phase [16]. Similar GIXRD analysis (data not shown) on La_2O_3 films thinner than 20 nm (e.g. samples S3 and S4) reveals that it is not possible to achieve the crystallization into the $h\text{-La}_2\text{O}_3$ phase across most of the sample thickness extent. This finding, which is correlated with Si atoms diffusion from the substrate induced by the RTA, will be addressed in a forthcoming part of this section.

XRR analysis performed on as-grown and 600 °C annealed S2 sample reveals the increase of the electron density of the main layer after annealing together with a corresponding thickness reduction, therefore confirming a densification of the layer due to OH^- desorption and crystallization. The electron density profiles extracted from the simulation of the XRR data are shown in Figure 3.6; values reported for $h\text{-La}_2\text{O}_3$ and for the crystallized hydroxides are also reported for comparison. The profiles are superimposed at the Si interface. Main modifications are found to occur also at the interface with Si, with the formation of a wider interfacial region.

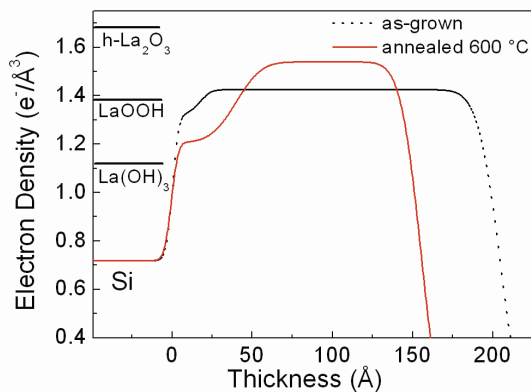


Figure 3.6: Electron density profiles extracted from the simulation of XRR data for as-grown (dotted line, black) and annealed at 600 °C (continuous line, red) nominally 20 nm thick sample.

Additional structural information with nanometric-scale resolution is provided for both as-grown and annealed La_2O_3 films by HRTEM analysis.

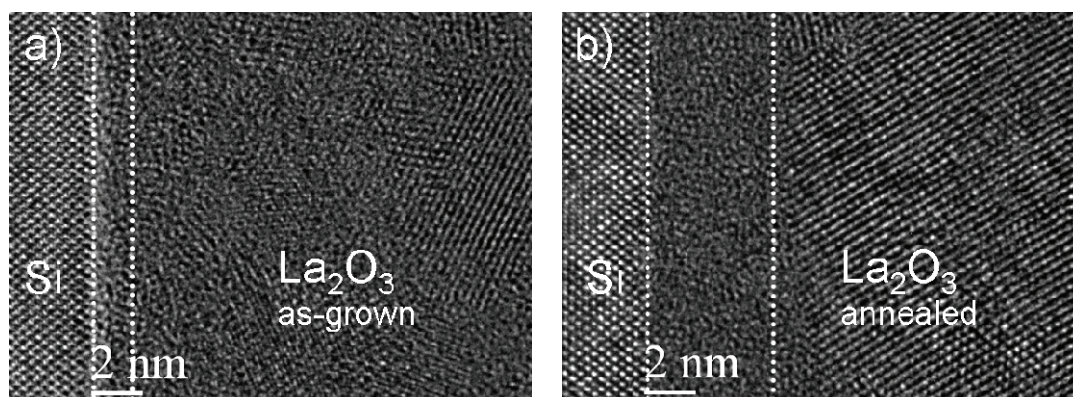
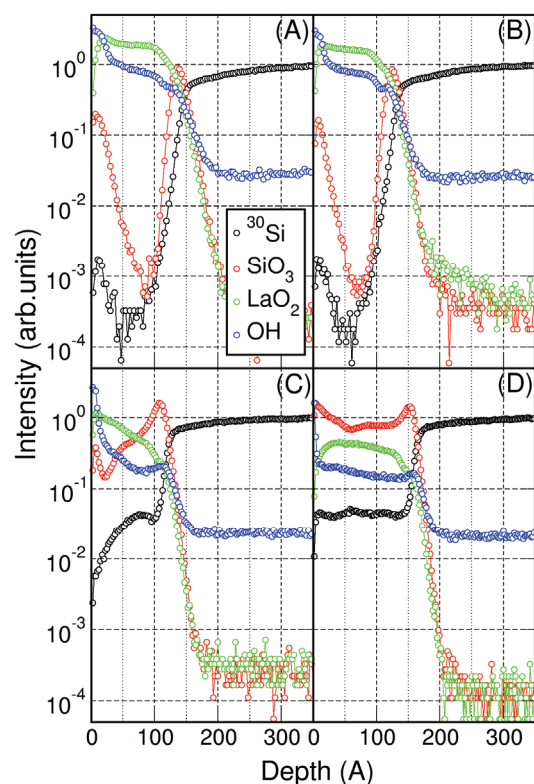


Figure 3.7: HRTEM cross sections of a 22 nm thick (a) as-grown and (b) annealed La_2O_3 film. Dotted white lines are a guide for the eyes to visualize the borderline between the film amorphous and crystalline parts.

Figure 3.7, which displays a HRTEM image for a 22 nm thick La_2O_3 film (i.e. sample S2) before and after RTA at 600 °C, indicates the presence of an amorphous transition region between the Si substrate and the film. The IL thickness increases with annealing from about 1.5 nm up to a value of ~5 nm. It is worth noticing that the extent of the IL appears to be minimized if compared to the ones observed in La_2O_3 films grown on H-terminated Si(100) using other ALD recipes [14]. After the amorphous IL, it is possible to identify a region containing La_2O_3 nanocrystals; therefore, manifesting in accordance with the GIXRD data in Figure 3.5 that RTA at 600 °C induces La_2O_3 film crystallization.



In order to address the evolution of the chemical properties at the interface and within the La_2O_3 films, ToF SIMS depth profiles were acquired on S3 in the as-grown state and after annealing performed at three different temperatures. A thinner sample than those used for GIXRD and HRTEM measurements is exploited for ToF SIMS analysis in order to probe the IL properties. In Figure 3.8, the ToF SIMS profile of as-grown sample (A) is compared with the depth profiles of the same sample after thermal treatments at 400 (B), 600 (C) and 800 °C (D).

Figure 3.8: ToF SIMS depth profiles acquired on ~10 nm thick films (A) as-grown and annealed at (B) 400 °C, (C) 600 °C and (D) 800 °C.

In good agreement with the HRTEM findings, the presence of a SiO_x -like IL in the as grown sample is revealed by monitoring the SiO_3 peak, as displayed in Figure 3.8(a). In addition, in the as-grown film, the SiO_3 and ^{30}Si signals at the surface reveal a moderate Si diffusion occurring through the La_2O_3 film during the ALD growth. Finally the depth profile of the OH^- signal shown in Figure 3.8(a) confirms the results of the GIXRD data analysis and attests the hygroscopicity of the as-grown La_2O_3 film. The analysis of the ToF-SIMS depth profiles after the 400 °C thermal treatment (Figure 4(b)) reveals that the chemical composition of the film has not been significantly affected by the low temperature annealing process. Indeed, the SiO_x -like IL seems stable in terms of thickness and composition and, moreover, the Si distribution throughout the layer is not modified by this low temperature annealing. Interestingly, despite the annealing process performed in vacuum, the OH^- profile is not altered, in good agreement with the GIXRD results; no significant modifications in the structure of the layer were revealed, thus confirming that the $\text{La}(\text{OH})_3$ conversion cannot be accomplished on Si(100) at an annealing temperature of 400 °C. In Figure 3.8(c) the depth profile of the sample annealed at 600 °C is reported. A clear reduction of the intensity of the OH^- signal is observed, in agreement with the structural analysis, supporting the hypothesis of the $\text{La}(\text{OH})_3$ conversion into $h\text{-La}_2\text{O}_3$ upon annealing at 600 °C. The ^{30}Si signal indicates that Si atoms diffusion from the substrate through the La_2O_3 occurred during the thermal treatment. The amount of $\text{La}(\text{OH})_3$ that can be actually crystallized in the $h\text{-La}_2\text{O}_3$ phase might depend on the amount of Si which is present in the layer. According to these results, the stack order atop the Si substrate after RTA at 600 °C can be roughly approximated by a tri-layer structure composed by an amorphous IL (mixture of SiO_x and LaSiO), a crystalline layer characterized by a decreasing Si content and a thin $\text{La}(\text{OH})_3$ surface layer. The presence of such a thin $\text{La}(\text{OH})_3$ top capping layer might be explained either by a not fully complete removal of the hydroxide component during the thermal treatment or by a re-hydroxylation that occurred during exposure to air before the ToF SIMS measurements. When the annealing temperature is increased up to 800 °C (Figure 3.8(d)), the thin $\text{La}(\text{OH})_3$ layer vanishes and no further reduction of the OH^- signal intensity is detected. Moreover the ^{30}Si signal in Figure 3.8(d) assumes a flat profile along the whole stack thickness, indicating that with a high temperature thermal treatment Si diffusion from the substrate throughout the entire stack thickness is promoted. This scenario is consistent with the formation of a fairly homogeneous LaSiO layer atop a stable IL and therefore with a two layers structure atop the Si(100).

The electrical characterization was performed at room temperature exclusively on MOS capacitors prepared on the stacks annealed in vacuum at 600 °C. To avoid moisture absorption, devices were mounted inside a cryomanipulator system operated in vacuum immediately after the metallization process. CET was determined from the device accumulation capacitance at 1 MHz.

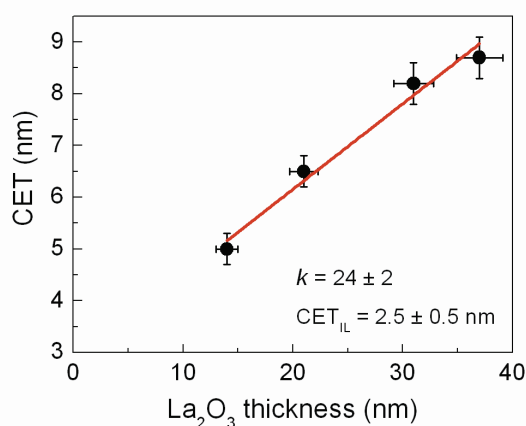


Figure 3.9: CET plot vs La_2O_3 physical thickness.

From the slope of a linear fit to a CET vs La_2O_3 thickness plot shown in Figure 3.9, the k value for the annealed La_2O_3 films is calculated to be around 24 ± 2 . In agreement with our GIXRD data, this value confirms that RTA in vacuum induces film crystallization into the h - La_2O_3 phase. It is noted that the lowest boundary associated with the k value derived here for the h - phase falls outside the typical range cited in the literature, [3,16] thus, suggesting a possible mixing of the stack crystalline part with an amorphous silica-based phase which is affecting the dielectric response of the whole stack. The fit in Figure 3.9 intercepts with the y -axis at a point corresponding to an IL with a CET of about 2.5 ± 0.5 nm which, in turn, yields, assuming the k value for the IL to be ~ 11 [17] an IL physical thickness of around 6-8 nm. This finding is in line either with HRTEM or with the ToF SIMS results, acquired on the sample annealed at 600 °C, where a significant Si atoms diffusion through about half of the 10 nm thick stack has been evidenced and associated with the formation of a LaSiO layer. A high k value which points to the expected 27 can be obtained only when the total film thickness is more than 20 nm. On the contrary, in thinner films the k value points more to a LaSiO value (~ 11) rather than the one associated to the h - phase. The electrical analysis has been therefore limited to the samples in which the structure after annealing can be mainly considered h - La_2O_3 and the interfacial region constitutes only a small part of the whole stack.

In conclusion, it is worth considering that the electrical analysis performed on the samples grown using the O_3 -based ALD recipe discussed in this work reveals the possibility to obtain h - La_2O_3 for a reduced stack thickness if compared to the ones previously reported [3,14,16,34]. This finding is associated to the obtainment of a less extended LaSiO region at the interface by means of the use of O_3 and probably also of a lower growth temperature. The achievement of a limited LaSiO region permits the crystallization of a significant part of the film into h - La_2O_3 and consequently allows a relative scaling of the EOT of the stack.

Introduction on LaZrO compounds

As the CMOS device dimensions continue to decrease in order to improve chip performance, high- k dielectrics are being introduced into the CMOS technology as alternative dielectrics to SiO_xN_y with the principal aim to suppress detrimental gate leakage current effects [35]. Among the various rare earth oxides [36] currently considered for the sub-45 nm high- k CMOS era La_2O_3 is remarkable mainly due to its high k value (~ 27 when crystallized into the hexagonal $P6_3/mmc$ phase) [37] and wide bandgap energy (~ 6 eV) [38]. However, the formation of $\text{La}(\text{OH})_3$ species arising from the absorption of OH^- groups when La_2O_3 is exposed to atmosphere significantly degrades its k value [39]. ZrO_2 could be another option for the sub-45 nm high- k CMOS nodes because it satisfies technology requirements in terms of k value and bandgap energy but the material is marginally chemically/thermally stable on Si [40], therefore, restricting an aggressive scaling down of the EOT. Alloying ZrO_2 with La_2O_3 to produce a ternary $\text{La}_x\text{Zr}_y\text{O}_z$ (LaZrO) compound might be a promising route to engineer a material suitable for high- k dielectric applications. Among the various growth techniques, [41,42,43,44,45,46] ALD appears to be the most attractive one for integration into the CMOS process cycle as it provides the capability to grow smooth and conformal films at a low deposition temperature, allowing also an accurate film thickness control at the nanometric scale [47].

In this second part of the Chapter, dedicated to LaZrO compounds, the development of the ALD process for a La-based ternary oxide is presented. The selection of a precise stoichiometry (i.e. La content = 25 %) was based on the optimization of the ALD process in terms of uniformity and growth rate. The structural and the electrical properties of this dielectric are presented. In addition, the same material was evaluated on 8" NVM test structures as potential high- k dielectric to be employed in novel NVM devices; the main results are summarized here.

Atomic layer deposition of LaZrO

ZrO₂ and LaZrO films were grown by ALD using La(ⁱPrCp)₃ in combination with the Zr precursor (CpMe)₂Zr(OMe)Me (also called ZrD-04), and O₃ as oxygen source. Films were grown in the Savannah 200 ALD reactor on 4" wafers; pulses of N₂ were injected in both chemical source cylinders (La and Zr) to improve precursor vapour extraction. La(ⁱPrCp)₃ and ZrD-04 were kept at 110 and 150 °C respectively. Preliminary ALD growth tests were performed using ZrD-04 and O₃; afterwards various La:Zr ALD pulse ratios were investigated (1:1, 1:4 and 4:1). LaZrO films were deposited by alternating ALD binary cycles of La₂O₃ and ZrO₂. The growth temperature ranged between 200 °C and 300 °C; it was found that the growth rate of both La₂O₃ and ZrO₂ steps increased when a higher growth temperature was used. Growth rates and process parameters of the various ALD processes are reported in Table 3.3 and Table 3.4. When La₂O₃ and ZrO₂ are mixed together in a ternary ALD recipe, the growth rates of the single steps/ALD cycles (Å/O₃ pulse) may differ from the values expected for the pure binary processes and therefore also a new global growth rate (Å/ternary cycle) can be calculated.

Table 3.3: ALD growth parameters for the depositions performed at 200 °C.

| Process | Pulse ratio La:Zr | T _{growth} (°C) | Growth rate (Å/ternary cycle) ± 0.1 | Growth rate (Å/O ₃ pulse) ± 0.1 |
|--|----------------------|-----------------------------|--|---|
| ZrD-04 + O ₃ | 0:1 | 200 | - | 0.4 |
| 1[La(ⁱ PrCp) ₃ +O ₃] + 1[ZrD-04+O ₃] | 1:1 | 200 | 1.4 | 0.7 |
| 1[La(ⁱ PrCp) ₃ +O ₃] + 4[ZrD-04+O ₃] | 1:4 | 200 | 2 | 0.4 |
| 4[La(ⁱ PrCp) ₃ +O ₃]+ 1[ZrD-04+O ₃] | 4:1 | 200 | 3.8 | 0.8 |

As far as the films deposited at 200 °C are concerned, the main issue turned out to be the poor reactivity of the ZrD-04 and O₃ process. This led to the obtainment of fairly low growth rates, in particular in the case of the 1:4 pulse ratio.

Table 3.4: ALD growth parameters for the depositions performed at 300 °C.

| Process | Pulse ratio La:Zr | T _{growth} (°C) | Growth rate (Å/ternary cycle) ± 0.1 | Growth rate (Å/O ₃ pulse) ± 0.1 |
|--|----------------------|-----------------------------|--|---|
| ZrD-04+O ₃ | 0:1 | 300 | - | 1.1 |
| 1[(ⁱ PrCp) ₃ La+O ₃] + 1[ZrD-04+O ₃] | 1:1 | 300 | 3 | 1.5 |
| 1[(ⁱ PrCp) ₃ La+O ₃] + 4[ZrD-04+O ₃] | 1:4 | 300 | 4.8 | 1.0 |
| 4[(ⁱ PrCp) ₃ La+O ₃] + 1[ZrD-04+O ₃] | 4:1 | 300 | 7.7 | 1.5 |

LaZrO films grown at 300 °C presented increasing thickness non-uniformity associated to the partial thermal decomposition of the La precursor occurring at temperatures above 200 °C. Indeed, the most promising ALD process was identified as the one characterized by the lowest La content. For the ALD pulse ratio set to 1:4, the thickness uniformity on 4" wafers was found to be fairly good ($t_{\text{non-un}} < 10\%$). The latter process was indeed also scaled-up to the 8" wafers. Lanthanum content was measured by means of XPS and EELS: La and Zr content was found to be around 25% and 75%, respectively. A self limiting behavior during the ALD pulses was achieved and a linear relation between the number of cycles and film thickness was observed as shown in Figure 3.10.

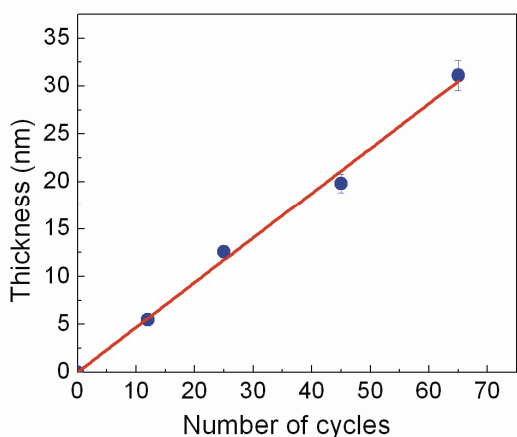


Figure 3.10: ALD of LaZrO (La:Zr = 1:4). Linear plot of the film thickness vs number of ALD cycles.

The latter ALD process, based on the combination of $\text{La}(\text{}^i\text{PrCp})_3$, ZrD-04 and O_3 at a growth temperature of 300 °C, with an ALD pulse ratio La:Zr = 1:4, was identified as the most promising and, therefore, film grown with this ALD recipe were thoroughly characterized.

“Atomic layer deposition of $\text{La}_x\text{Zr}_{1-x}\text{O}_{2-\delta}$ ($x=0.25$) high- k dielectrics for advanced gate stacks” [48]

We report on the growth of $\text{La}_x\text{Zr}_{1-x}\text{O}_{2-\delta}$ ($x = 0.25$) (LZO) by ALD using O_3 , a more powerful oxidizer than H_2O tested by Gaskell *et al.* [44,46], in combination with the same La [i.e., $(^i\text{PrCp})_3\text{La}$] and Zr [i.e., $(\text{MeCp})_2\text{ZrMe}(\text{OMe})$] precursors as in Ref. [44,46]. Contrary to Ref. [44,46], which are almost exclusively concerned with the properties of as-grown LZO films, our study merely focuses on annealed films since CMOS device processing involves some post-deposition thermal treatment. LZO films were deposited in the Savannah 200 ALD reactor on H-terminated n-Si(100) at a growth temperature of 300 °C. $(^i\text{PrCp})_3\text{La}$ and ZrD-04 complexes were kept at 150 and 110 °C respectively. O_3 (obtained from pure O_2) was injected into the reactor at a concentration of about 200 g/Nm³. The ALD cycle number varied between 12 and 50, resulting in a stack thickness within the 5-30 nm range. The oxide La atomic fraction $x = \text{La}/(\text{La}+\text{Zr}) = 0.25$, which was tuned by altering the ALD pulse number during the growth cycle, was estimated from the La $3d$ and Zr $3d$ core-level X-ray photoelectron spectroscopy (XPS) lines relying on the relevant atomic sensitivity factors. Post-growth rapid thermal annealing (RTA) was performed for 60 s in vacuum (~ 1 mbar) at 600 °C. Opposed to RTA in forming gas, or N_2 ambient, annealing in vacuum permits monitoring of thermally-induced structural, compositional and electrical changes minimizing any contribution to them coming from the atmosphere itself. Moreover, vacuum should enhance the removal of the OH^- groups from the La-based film. LZO films were characterized by a combination of: (i) grazing incidence x-ray diffraction (GIXRD) (ii) transmission electron microscopy in the high resolution (HRTEM) and electron energy loss spectroscopy (EELS) modes (iii) XPS and (iv) capacitance-voltage (CV), parallel conductance-voltage (G_pV) and current density-voltage (JV) measurements.

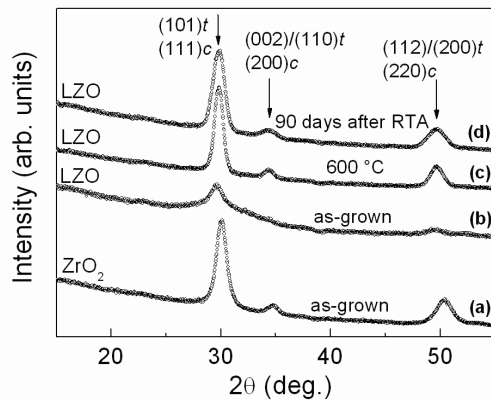


Figure 3.11: GIXRD spectra for the ZrO_2 and LZO films (a) ZrO_2 as-grown, (b) LZO as-grown, (c) LZO annealed at 600 °C and (d) LZO 90 days after annealing.

Figure 3.11 displays GIXRD spectra for the 24 nm thick ZrO_2 and LZO films. Although the monoclinic phase is the most stable phase [49] for pure ZrO_2 in equilibrium below 1100 °C, the as-grown ZrO_2 film [Figure 3.11(a)], which was deposited at 300 °C using the ZrD-04 and O_3 recipe [50] is found to adopt a cubic or tetragonal ZrO_2 structure [51] owing to ALD growth under non-equilibrium conditions. An XRD-based delineation between the cubic and tetragonal ZrO_2 phases is difficult since the respective reflections [51] appear at vicinal angles. The La incorporation into the host ZrO_2 matrix through the ternary ALD process mostly generates thin amorphous as-grown LZO films as evidenced from the very low signal in Figure 3.11(b).

The latter finding is subsequently confirmed by the TEM image as shown in Figure 3.12(a).

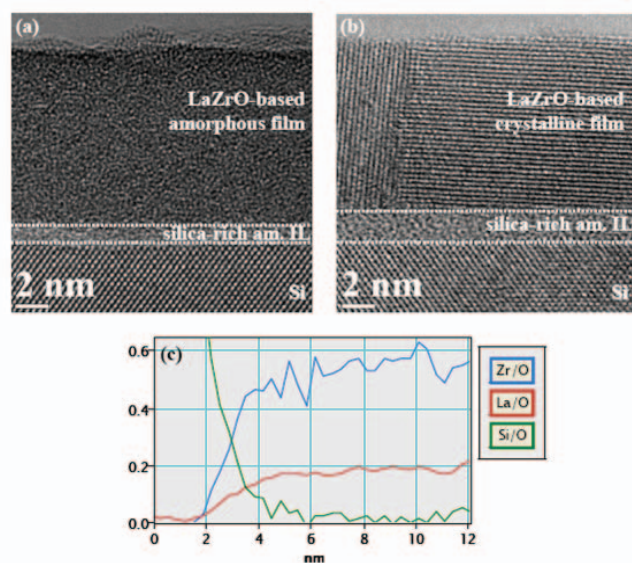


Figure 3.12: Cross-section HRTEM images for the 12 nm thick LZO film. (a) as-grown state, (b) after RTA for 60 s in vacuum at 600 °C. Dotted lines are guide to the eye. (c) STEM-EELS profiles of elemental La/O, Zr/O, and Si/O ratios for the annealed state.

As illustrated in Figure 3.11(c), LZO films crystallize after RTA into the cubic or tetragonal ZrO_2 phases. Thinner (20 and 12 nm) LZO films were found (data not shown) to exhibit the same structural behavior as the 24 nm thick one. It is noted that, contrary to La_2O_3 films, LZO films are not hygroscopic as demonstrated by both Figure 3.11(d) and XPS O 1s line (data not shown) taken after 90 days long exposure to air. HRTEM coupled to STEM-EELS data were recorded on the 12 nm thick as-grown and annealed LZO stacks. As depicted in Figure 3.12(a)-(b), an amorphous interface layer (IL) of clear contrast, corresponding to a silica-rich region in the elemental profiles (Figure 3.12 (c)), appears just above the Si substrate for both cases with the IL thickness increasing following RTA. Atop the IL, a predominantly amorphous high- k layer for the as-grown stack and a crystalline one for the annealed stack are observed. Chemically these layers can be divided in two regions, one of variable composition including La, Zr, O and Si elements and with a similar extent, 4 nm after the Si surface, for both films. Then, the composition becomes constant without Si and a La content of 25%. Crystallographic parameters measured on the projected planes of the HRTEM images and on selected area electron diffraction patterns (data not shown) for the annealed film correspond to those for the cubic or tetragonal ZrO_2 phases [51]. Differently from Ref. [45], no cluster nucleation, as manifested from the TEM-EELS analysis, occurs near the interface or within the film. To unveil the IL composition, an XPS analysis was conducted on a 5 nm thick LZO stack. Since the La 4d line overlaps with the high binding energy (BE) tail/oxidation state components of the Si 2p line, we considered the Si 2s line for the pertinent analysis.

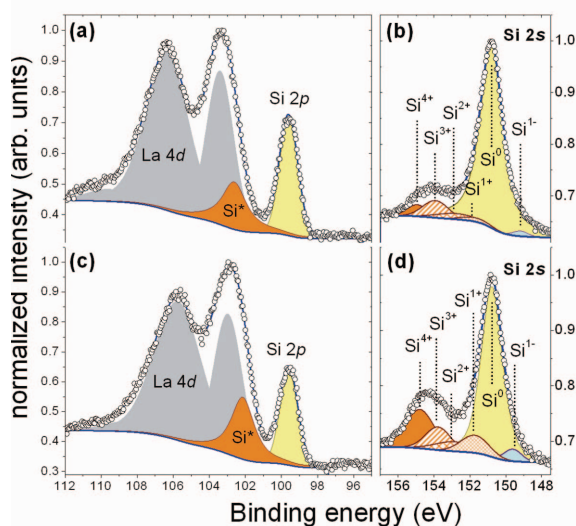


Figure 3.13: XPS Si 2p and 2s shape profiles at a take-off angle of 90° for a 5 nm thick LZO film. (a)–(b) Si 2p and 2s lines for the as-grown state. (c)–(d) Si 2p and 2s lines after RTA for 60 s in vacuum at 600 °C. Chemical shifts are 1.3, 2.1, 3.1, and 4.0 eV for 1⁺, 2⁺, 3⁺, and 4⁺ oxidation states, respectively.

Figure 3.13 compares the Si 2s lines for the as-grown and annealed states. The Si 2s peak is decomposed into six components: the elemental Si signal (Si^0), four oxidation state components (Si^{1+} , Si^{2+} , Si^{3+} , Si^{4+} corresponding to Si_2O , SiO , Si_2O_3 and SiO_2 species respectively) [52] and an additional component (Si^{1-}) related to a minor Si-metal bonding. In agreement with HRTEM analysis, XPS data manifest an RTA-induced increase of the IL thickness because the broad peak due to the overall oxide contribution is larger after RTA. They also corroborate the STEM-EELS data on the silica-rich nature of the IL since the Si^{4+} component, which implies a SiO_2 bonding arrangement, becomes the dominant one after RTA.

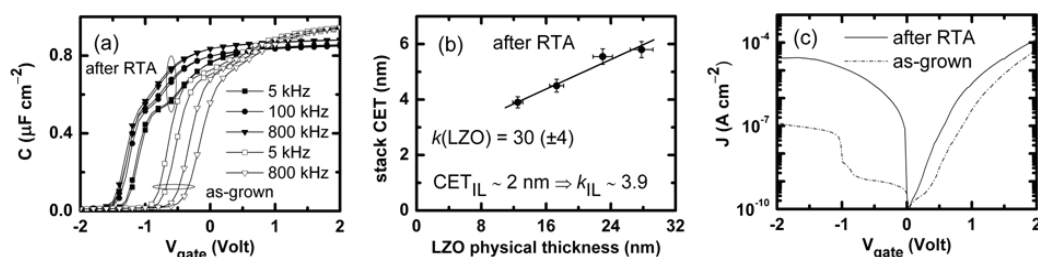


Figure 3.14: Electrical characteristics for MIS capacitors from a 13 nm thick LZO stack. (a) multifrequency C-V curves for as-grown (empty symbols) and RTA-treated (filled symbols) devices. (b) Stack CET vs LZO film physical thickness plot for RTA-treated devices. (c) J-V curves for as-grown and RTA-treated devices.

Figure 3.14(a) illustrates CV curves for as-grown and annealed LZO stacks of about 13 nm thickness. For both cases, accumulation capacitance exhibits minor frequency dispersion within the 5-800 kHz range. Table 3.5 summarizes certain electrical figures of merit derived from analyzing the data in Figure 3.14(a).

Table 3.5: Figures of merit for 13 nm as-grown and annealed LZO stacks (W) hysteresis width, V_{FB} (flatband voltage), D_{it} (interface traps density). a) Referenced to $C_{\text{max}}/2$ for a bidirectional -2/+2 V sweep at 100 KHz. b) Referenced to the experimental 800 kHz C-V curve; theoretical value derived from the Al-Si work function difference is -021 V. c) Hill-Coleman method applied to the $G_p V$ peak at 100 kHz.

| Stack state | W^a (mV) | V_{FB}^b (V) | D_{it}^c ($\times 10^{12} \text{ eV}^{-1} \text{ cm}^{-2}$) |
|---------------|------------------|-----------------------|--|
| As-grown | 170 (± 10) | -0.46 (± 0.07) | 3.8 (± 0.4) |
| RTA in vacuum | 40 (± 10) | -1.47 (± 0.15) | 2.1 (± 0.2) |

Evidently, RTA notably lowers the density of oxide trapped charge and interface defects while markedly enhancing the positive fixed charge density near the dielectric/Si interface. From the slope of a linear fit to a stack CET versus LZO physical thickness plot in Figure 3.14(b), the k value for annealed LZO films is estimated to be around 30. Based on k value calculated theoretically for different ZrO_2 crystalline phases [49,53], our result points more to a cubic rather than tetragonal ZrO_2 phases. In good agreement with the HRTEM and STEM-EELS analyses, the fit to the above plot intercepts with the y-axis at a point corresponding to an IL with a k value close to that of SiO_2 . It is underlined that our as-grown LZO films feature a k value that varies with the stack thickness such that it is as low as 17.5 for a 12.5 nm thick stack and as high as 24 for a 22.5 nm thick stack. In the light of dark field TEM images (data not shown), this trend is ascribed to the fact that as-grown LZO films are not entirely amorphous but contain a small fraction of isolated nanocrystals which contribute to a different extent to the film k value because their size is found to increase when the physical thickness of the layer increases. Consequently, it is inferred that the thermally-induced crystallization of the as-grown

amorphous LZO films is accompanied by a moderate k value enhancement also with respect to the parental ZrO_2 films [50]. Given the connection between phonon vibrational spectra and k value [54], the above finding can be tentatively attributed to softening, through partial substitution of Zr with La atoms [55], of the cubic or tetragonal ZrO_2 infrared-active transverse optical phonon mode with minimum frequency [53]. Finally, it is ascertained from Figure 3.14(c) that although RTA significantly degrades, compared to the as-grown state, the stack hardness to leakage paths, an acceptable leakage current density still flows through the MIS capacitor when pulsed in strong accumulation and inversion.

In conclusion, thin and uniform LZO films have been grown on Si(100) by ALD at 300 °C using (ⁱPrCp)₃La, ZrD-04 and O₃ sources. Their structural, chemical and electrical properties have been studied after 60 s vacuum anneal at 600 °C. Annealed films crystallize into cubic or tetragonal ZrO_2 phases with a k value of around 30. They are also immune to hygroscopicity and exhibit an acceptable leakage current density. Although such a high k value is desirable for further EOT scaling down, process optimization is still required in order to minimize both the sizable low- k silica-rich IL at the high- k /Si junction and the dielectric/Si interface defect density.

“Rare earth-based high- k materials for non-volatile memory applications” [56]

As indicated in the ITRS roadmap [57,58], NAND Flash scaling is currently progressing at a much faster rate than CMOS logic technology. Scaling of conventional floating gate flash memories, both in NOR or NAND architectures, presents tremendous challenges. In particular, high- k materials are very interesting for non-volatile memories based on metal gate/high- k /Si₃N₄/SiO₂/Si (TANOS) structures since they can be stacked as blocking oxide in substitution of standard oxide-nitride-oxide stack. Due to its excellent conformality, very good thermal stability, moderately high dielectric constant ($k \sim 10$ after crystallization), large band-gap and good resistance to leakage currents [59], Al₂O₃ is a well known high- k material which might be properly integrated as blocking oxide in 32 nm TANOS memories. For 22 nm node, dielectric materials with higher k values are currently under investigation. This work focuses on high- k materials to be implemented as blocking oxide. In the frame of this research activity, a comparison between Al₂O₃ and a La-based high- k dielectric is shown. Actually, alloying two binary high- k oxides like La₂O₃ [60] and ZrO₂ [61] might result in a ternary compound with optimized dielectric properties and thermal stability [62]. La _{x} Zr _{$1-x$} O _{$2-\delta$} ($x=0.25$) (LZO) compound is considered. In particular, this ternary oxide has been developed in a research tool at MDM, deposited on 8-inches patterned Si wafers, and then transferred to the Numonyx pilot line for device finishing and characterization in order to test their electrical properties as a possible dielectric, *i.e.* leakage current, EOT and dielectric constant. Many integration issues arose for the process in front end of line production of this material associated to the presence of metal contamination. In this respect, LZO films were capped with 80 Å thick Al₂O₃ films deposited by ALD.

LZO films have been grown by atomic layer deposition (ALD) using (¹PrCp)₃La, (MeCp)₂ZrMe(OMe) (SAFC Hitech) and O₃ at 300 °C. La atomic fraction $x = \text{La}/(\text{La}+\text{Zr}) = 0.25$, was tuned by altering the ALD pulse number in the growth cycle, and estimated by X-ray photoelectron spectroscopy and electron energy loss spectroscopy. The films have been deposited on 8” Si(100) patterned wafers in the 50-200 Å thickness range. In order to prevent La and Zr contamination in the front end of the line due to wafer processing, LZO films should be capped. For this purpose, a thin Al₂O₃ film has been deposited by ALD in ASM Pulsar 3000™ reactor using TMA and H₂O (as described in Ref. 59). In one case, H₂O was substituted by O₃ in order to evaluate the eventual beneficial effect of a stronger oxidizing precursor on the electrical properties of the stack. The thickness of the Al₂O₃ layer should be minimized in order to enhance the quality of the information that can be obtained on the high- k layer from the electrical characteristics of the capacitors. The stack thermal stability and structural evolution upon postdeposition rapid thermal annealing (RTA) at 900 °C in N₂ have been studied by Time of Flight-Secondary Ion Mass Spectrometry (ToF-SIMS), Total reflection X-ray fluorescence (TXRF), Transmission Electron Microscopy (TEM), and X-ray diffraction (XRD). Current-Voltage (J-V) and Capacitance-Voltage (C-V) curves have been measured on capacitors obtained by 3-masks test pattern. LZO might intermix with the other layers of the stack due to possible thermal instability issues. This fact would certainly constitute a main integration problem. Therefore, chemical interaction between LZO and Al₂O₃ has been studied in as-grown stacks and also after thermal treatments in N₂ atmosphere at 900 °C. In order to obtain a well defined bi-layer, different Al₂O₃ thicknesses have been taken into account. In particular, 40 and 80 Å thick films have been deposited on LZO.

ToF SIMS depth profiles performed on Al₂O₃/LZO stacks show that a slight diffusion of ZrO occurs through a 40 Å thick Al₂O₃ cap (not shown). Differently, capping the LZO film with an 80 Å thick Al₂O₃ film avoids undesired metal diffusion up to the surface (Figure 3.15(a)). After annealing only a slight intermix occurs, as reported in Figure 3.15(b): the ZrO signal increases within the Al₂O₃ region and AlO signal increases within the LZO region. Nevertheless, no Zr or La contaminants were revealed by means of TXRF on the surface of the wafer either before or after RTA.

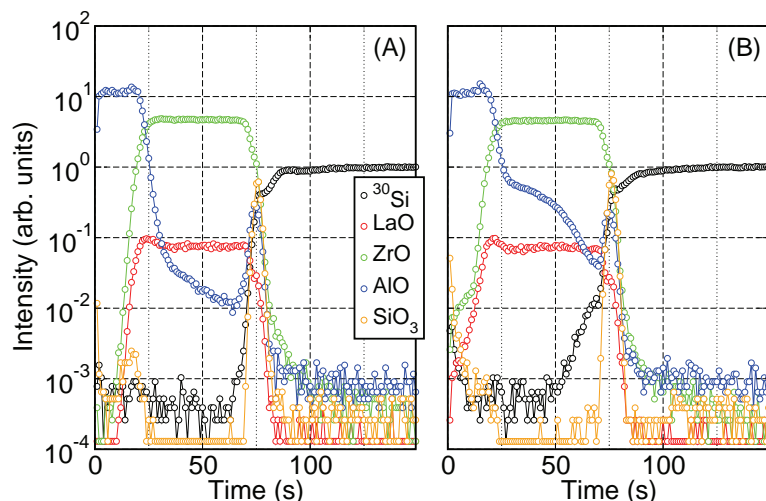


Figure 3.15: ToF SIMS depth profiles of (a) as deposited and (b) annealed at 900 °C in N₂ Al₂O₃/LZO stacks.

After annealing both Al₂O₃ and LZO films are completely crystallized as shown in the stack cross sectional TEM image (Figure 3.16).

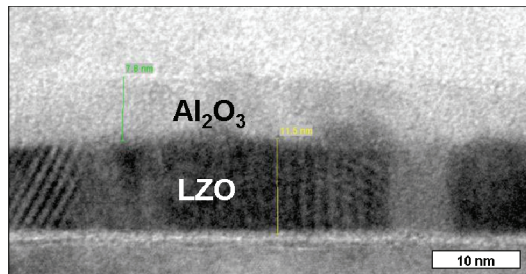


Figure 3.16: Cross-sectional TEM image of Al₂O₃/LZO stack annealed at 900 °C in N₂.

XRD performed on capped stacks before and after RTA (Figure 3.17) shows the crystallization of the Al₂O₃, while the crystallographic ordering of the LZO layer, in the cubic or tetragonal phase of ZrO₂, is mainly not affected by the thermal treatment. Moreover, TEM cross section shows well defined interfaces between the different layers.

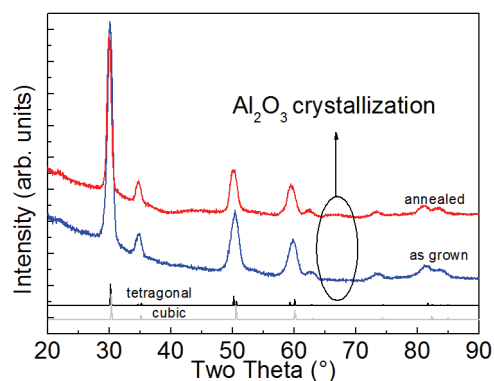


Figure 3.17: XRD analysis of as-grown and annealed Al₂O₃/LZO stacks. The thickness of the Al₂O₃ layer is 80 Å. The powder spectra of tetragonal and cubic ZrO₂ are also added for comparison.

The electrical characteristics of MOS structures have been evaluated. Three different film thicknesses have been deposited; each film has been capped with Al₂O₃ and subsequently annealed at 900 °C. 8” wafers have been processed using a 3 masks test pattern on which capacitors having different areas (1.1×10⁻³ cm² and 9.18×10⁻³ cm²) have been defined. A poly-Si layer, covered by WSi_x, in order to decrease its resistance, has been employed as metal gate for MOS structures on p-type, 1×10⁻¹⁸ cm⁻³ doped, Si(100) substrates. WSi_x/poly-Si/Al₂O₃/pSi(100) MOS structures and TaN/Al₂O₃/pSi(100) structures have been also evaluated as reference. In Table 3.6 description of the samples is reported.

Table 3.6: Description of the electrical samples: stack films thickness and postdeposition annealing. Al₂O₃ deposited on wf1–wf4 was prepared using H₂O-based ALD process whereas Al₂O₃ deposited on wf5 was prepared using O₃-based process.

| Sample | LZO thickness (Å) | Al ₂ O ₃ thickness (Å) | RTA |
|--------|-------------------|--|--------------------------|
| wf1 | 200 | 80 | 900 °C in N ₂ |
| wf2 | 150 | 80 | 900 °C in N ₂ |
| wf3 | 100 | 80 | 900 °C in N ₂ |
| wf4 | 50 | 110 | 900 °C in N ₂ |
| wf5 | 150 | 80 (O ₃ process) | 900 °C in N ₂ |

The EOT values of LZO have been evaluated from capacitance in the accumulation region (gate voltage -5 V and frequency 10 kHz) of capacitors having the same Al₂O₃ thickness and different LZO thicknesses, corresponding to samples w1, w2 and w3 (Table 3.6). The *k* value attributed to LZO films is equal to 27 ± 3, in fairly good agreement with the one reported in Ref. 48 (our earlier work), although in the present work the LZO was capped with Al₂O₃. This high permittivity value makes LZO a promising candidate for integration as blocking oxide in TANOS structures. The C-V curves (reported in Figure 3.18) show that all the samples have a hysteresis due to unstable charge present in the layer. This charge can be present both in the Al₂O₃ and LZO layers, the contribution to the charge of the different films cannot be attributed precisely due to the stacked structure of the dielectric in the MOS capacitor.

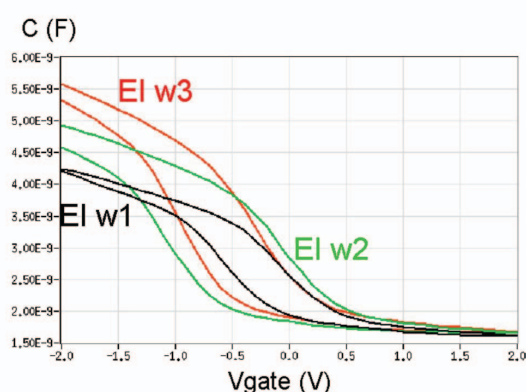


Figure 3.18: C–V plots of samples w1, w2 and w3. Measurements sequence is V_{gate} = -2/+2/-2 V.

The leakage current evaluation has been performed by normalizing all the J-V curves with respect to the EOT, thus obtaining J-E curves. In this way we can have a consistent comparison between the different samples and the Al₂O₃ reference. In Figure 3.19, J-E curves acquired on different samples are reported. J-V measurements have been carried out in positive and negative polarity in order to evaluate the fixed charge inside the films. Repeated J-V measurements in negative polarity do not reveal the presence of such fixed charge; moreover, no significant trapping during voltage ramp is observed. The

Al_2O_3 reference is reported both with poly-Si and metal gate (i.e. TaN). For low voltages the leakage current can be extrapolated by considering the slope of the curve. At low voltages, the leakage current measured for $\text{Al}_2\text{O}_3/\text{LZO}$ stacks is larger for all the analyzed samples as compared to the one measured on MOS structures including only Al_2O_3 . On the other hand, for high voltages the leakage current is lower for $\text{Al}_2\text{O}_3/\text{LZO}$ stacks. Therefore, this stack performs better in program/erase whereas Al_2O_3 is favored in retention. Furthermore, a very good breakdown field is measured: the film breaks down around 14-16 MV/cm, a value very close to that measured for Al_2O_3 films. Thus, depending on the working voltage of the memory, the electrical quality of this La-based film can be comparable and even better than that of Al_2O_3 . Comparing samples w2 and w5, LZO films present the same electrical characteristics, although Al_2O_3 was grown using H_2O and O_3 , respectively. Since the two stacks show the same electrical behavior, we can conclude that oxidant agent has in this case no appreciable impact.

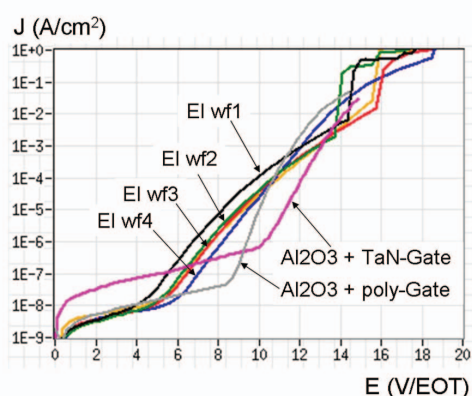


Figure 3.19: J-E curves relative to $\text{Al}_2\text{O}_3/\text{LZO}$ stacks with poly-Si as metal gate. Curves obtained on structures including only Al_2O_3 and both poly-Si and metal gate are reported as reference.

In this work we have shown the integration and the electrical analysis of LZO in 8" test structures for the evaluation of this material, as possible interpoly dielectric or blocking oxide candidate, for next generation of non-volatile memories. Amongst the different problems that might occur during integration, the La and Zr contamination issue has been solved by capping the LZO layer with a 80 Å thick Al_2O_3 film. In this way, a satisfactory integration in an industrial pilot line has been carried out, giving the possibility of electrically test this material on 8" test patterned wafers. Promising electrical results have been achieved; after integration LZO presents a large dielectric constant ~ 27 . This material contains instable charge as revealed by C-V hysteresis. Nevertheless, negative J-V characteristics are quite stable showing that no permanent charge trapping is occurring. Finally, LZO shows higher leakage current at low fields with respect to Al_2O_3 but lower leakage at higher fields. Stack quality in terms of breakdown electric field is also comparable. This ternary rare earth-based material shows promising results in terms of breakdown voltage, dielectric constant and leakage current. In order to further investigate its electrical behavior it needs to be integrated in a complete TANOS stack.

References

- [1] M. Fanciulli, G. Scarel (eds.), “*Rare earth oxide thin films: growth, characterization, and applications*”, Topics in Applied Physics vol. 106, Springer, Berlin (2007).
- [2] H. Okamoto, J. Phase Equilibria and Diffusion **26**, 292 (2005).
- [3] G. Scarel, A. Debernardi, D. Tsoutsou, S. Spiga, S. C. Capelli, L. Lamagna, S. N. Volkos, M. Alia, and M. Fanciulli, Appl. Phys. Lett. **91**, 102901 (2007).
- [4] S. Jeon and H. Hwang, J. Appl. Phys. **93**, 6393 (2003).
- [5] H. Ono and T. Katsumata, Appl. Phys. Lett. **78**, 1832 (2001).
- [6] D. G. Schlom and J. H. Haeni, MRS Bulletin **27**, 198 (2002).
- [7] L. Marsella and V. Fiorentini, Phys. Rev. B **69**, 172103 (2004).
- [8] S. Stemmer, J. Vac. Sci. Technol. B **22**, 791 (2004).
- [9] S. Stemmer, J. P. Maria, and A. I. Kingon, Appl. Phys. Lett. **79**, 102 (2001).
- [10] G. A. Botton, J. A. Gupta, D. Landheer, J. P. McCaffrey, G. I. Sproule, and M. J. Graham, J. Appl. Phys. **91**, 2921 (2002).
- [11] V. Narayanan, S. Guha, M. Copel, N. A. Bojarczuk, P. L. Flaitz, and M. Gribelyuk, Appl. Phys. Lett. **81**, 4183 (2002).
- [12] R. Lo Nigro and R. G. Toro, Adv. Mater. **15**, 1071 (2003).
- [13] D. J. Lichtenwalner, J. S. Jur, A. I. Kingon, M. P. Agustin, Y. Yang, S. Stemmer, L. V. Goncharova, T. Gustafsson, and Eric Garfunkel, J. Appl. Phys. **98**, 024314 (2005).
- [14] S. Schamm, G. Scarel and M. Fanciulli, in “*Rare earth oxide thin films: growth, characterization, and applications*”, M. Fanciulli and G. Scarel, Editors, Topics in Applied Physics vol. 106, p. 153, Springer-Verlag (2006).
- [15] M. V. Fischetti, D. A. Neumayer, and E. A. Cartier, J. Appl. Phys. **90**, 4587 (2001).
- [16] D. Tsoutsou, G. Scarel, A. Debernardi, S. C. Capelli, S. N. Volkos, L. Lamagna, S. Schamm, P. E. Coulon, M. Fanciulli, Microelectr. Eng. **85**, 2411 (2008).
- [17] S. Schamm, P. E. Coulon, S. Miao, S. N. Volkos, L. H. Lu, L. Lamagna, C. Wiemer, D. Tsoutsou, G. Scarel, and M. Fanciulli, J. Electrochem. Soc. **156**(1), H1 (2009).
- [18] H. M. Rietveld, Acta Crystallogr., **22**, 151 (1967); J. Appl. Crystallogr. **2**, 65 (1969).
- [19] ICSD, Inorganic Crystal Structure Data 2006-2, file number #200090.
- [20] ICSD, Inorganic Crystal Structure Data 2006-2, file number #96201.
- [21] ICSD, Inorganic Crystal Structure Data 2006-2, file number #28555.
- [22] J. Paivasaari, J. Niinisto, P. Myllymaki, C. Dezelah IV, C. H. Winter, M. Putkonen, M. Nieminen, L. Niinisto, “*Atomic Layer Deposition of Rare Earth Oxides*” in Topics in Applied Physics, Springer Berlin/Heidelberg, vol. 106 “Rare earth oxide thin films”, pp 15-32 (2006).
- [23] J. Paivasaari, Ph.D. Thesis “*Atomic layered deposition of lanthanide oxide thin films*”, Helsinki University of Technology, ISBN 951-22-8163-5 (2006).
- [24] S. Rushworth, H. Davies, A. Kingsley, T. Leese, R. Odedra, Microelectronics Reliability **47** 718 (2007).
- [25] S. D. Elliott, Surf. & Coat. Technol. **201**, 9076 (2007).
- [26] D. Eom, S. Y. No, C. S. Hwang, and H. J. Kim, J. Electrochem. Soc. **154**, G49 (2007).
- [27] S. Y. No, D. Eom, C. S. Hwang, and H. J. Kim, J. Appl. Phys. **100**, 024111 (2006).
- [28] J. Kwon, M. Dai, M. D. Halls, E. Langereis, Y. J. Chabal, and R. G. Gordon, J. Phys. Chem. C **113**(2), 654 (2009).
- [29] T. Gougousi, D. Niu, R. W. Ashcraft, and G. N. Parsons, Appl. Phys. Lett. **83**, 3543 (2003).
- [30] X. Li, D. Tsoutsou, G. Scarel, C. Wiemer, S. C. Capelli, S. N. Volkos, L. Lamagna, and M. Fanciulli, J. Vac. Sci. Technol. A **27**(2), L1 (2009).
- [31] L. Lamagna *et al.*, “*O₃-based atomic layer deposition of hexagonal La₂O₃ on Si and Ge*”, in preparation (2009).
- [32] Inorganic Crystal Structure Database, Fachinformationszentrum, Karlsruhe, 2009, file n°: 31584.
- [33] Inorganic Crystal Structure Database, Fachinformationszentrum, Karlsruhe, 2009, file n°: 24693
- [34] Y. H. Wu, M. Y. Yang, A. Chin, W. J. Chen, C. M. Kwei, IEEE Electron. Dev. Lett. **21**, 341 (2000).
- [35] J. Robertson, Rep. Prog. Phys. **69**, 327 (2006).
- [36] G. Scarel, A. Svane, and M. Fanciulli, *Rare Earth Oxide Thin Films: Growth, Characterization and Applications*, Topics in Applied Physics, Vol. 106, M. Fanciulli and G. Scarel (Eds.), Chapter 1, p. 1-14, Springer-Verlag Berlin (2007).

-
- [37] G. Scarel, A. Debernardi, D. Tsoutsou, S. Spiga, S. C. Capelli, L. Lamagna, S. N. Volkos, M. Alia, and M. Fanciulli, *Appl. Phys. Lett.* **91**, 102901 (2007).
- [38] A. V. Prokofiev, A. I. Shelyakh, and B. T. Melekh, *J. All. Comp.* **242**, 41 (1996).
- [39] Y. Zhao, M. Toyama, K. Kita, K. Kyuno, and A. Toriumi, *Appl. Phys. Lett.* **88**, 072904 (2006).
- [40] M. C. Zeman, C. C. Fulton, G. Lucovsky, R. J. Nemanich, and W.-C. Yang, *J. Appl. Phys.* **99**, 023519 (2006).
- [41] K. Bobzin, E. Lugscheider, and N. Bagcivan, *High Temp. Mater. Processes* **10**, 103 (2006).
- [42] J. W. Seo, J. Fompeyrine, A. Guiller, G. Norga, C. Marchiori, H. Siegwart, and J.-P. Locquet, *Appl. Phys. Lett.* **83**, 5211 (2003).
- [43] J. Fompeyrine, G. Norga, A. Guiller, C. Marchiori, J. W. Seo, J.-P. Locquet, H. Siegwart, D. Halley, and C. Rossel, in *Proceedings of the WODIM 2002, 12th Workshop on Dielectrics in Microelectronics* (IMEP, Grenoble, France, 2002), p65.
- [44] J. M. Gaskell, A. C. Jones, H. C. Aspinall, S. Taylor, P. Taechakumput, P. R. Chalker, P. N. Heys, and R. Odedra, *Appl. Phys. Lett.* **91**, 112912 (2007).
- [45] K. B. Jinesh, W. F. Besling, E. Tois, J. H. Klootwijk, W. Dekkers, M. Kaiser, F. Bakker, M. Tuominen, and F. Roozeboom, *Appl. Phys. Lett.* **93**, 062903 (2008).
- [46] J. M. Gaskell, A. C. Jones, P. R. Chalker, M. Werner, H. C. Aspinall, S. Taylor, P. Taechakumput, and P. N. Heys, *Chem. Vap. Deposition* **13**, 684 (2007).
- [47] R. L. Puurunen, *J. Appl. Phys.* **97**, 121301 (2005).
- [48] D. Tsoutsou, L. Lamagna, S. N. Volkos, A. Molle, S. Baldovino, S. Schamm, P. E. Coulon, and M. Fanciulli, *Appl. Phys. Lett.* **94**, 053504 (2009).
- [49] G-M. Rignanese, *J. Phys.: Condens. Matter* **17**, R357 (2005).
- [50] A. Lamperti, L. Lamagna, G. Congedo, S. Spiga, and M. Fanciulli (unpublished).
- [51] G. Katz, *J. Am. Cer. Soc.* **54**, 531 (1971) for cubic ZrO₂ and G. Teufer, *Acta Crystallogr.*, **15** 1187 (1962) for tetragonal ZrO₂.
- [52] A. Yoshigoe and Y. Teraoka, *Surf. Interface Anal.* **34**, 432 (2002).
- [53] X. Zhao and D. Vanderbilt, *Phys. Rev. B* **65**, 075105 (2002).
- [54] E. Bonera, G. Scarel, and M. Fanciulli, P. Delugas and V. Fiorentini, *Phys. Rev. Lett.* **94**, 027602 (2005).
- [55] S. A. Shevlin, A. Curioni, and W. Andreoni, *Phys. Rev. Lett.* **94**, 146401 (2005).
- [56] M. Alessandri, A. Del Vitto, R. Piagge, A. Sebastiani, C. Scozzari, C. Wiemer, L. Lamagna, M. Perego, G. Ghidini, M. Fanciulli, *Microelectr. Eng.* **85**, in press (2009).
- [57] S. K. Lai, *IBM J. Res. & Dev.* **52**, 529 (2008).
- [58] <http://www.itrs.net>.
- [59] M. Alessandri, R. Piagge, S. Alberici, E. Bellandi, M. Caniatti, G. Ghidini, A. Modelli, G. Pavia, E. Ravizza, and A. Sebastiani, *ECS Transactions*, **1** (5) 91 (2006).
- [60] G. Scarel, A. Debernardi, D. Tsoutsou, S. Spiga, S.C. Capelli, L. Lamagna, S. N. Volkos, M. Alia, and M. Fanciulli, *Appl. Phys. Lett.* **91**, 102901 (2007).
- [61] K. Kukli, J. Niinisto, A. Tamm, J. Lu, M. Ritala, M. Leskela, M. Putkonen, L. Niinisto, F. Song, P. Williams, P. N. Heys, *Microelec. Eng.* **84** 2010 (2007).
- [62] D. Fischer, A. Kersch, *Appl. Phys. Lett.* **92**, 012908 (2008).

Chapter 4

Er-based oxides*

* Results to be published as:

C. Wiemer, L. Lamagna, S. Baldovino, M. Perego, S. Schamm, P. E. Coulon, O. Salicio, G. Congedo, S. Spiga, and M. Fanciulli, “*Dielectric properties of Er-doped HfO₂ (Er ~15%) grown by atomic layer deposition for high-k gate stacks*”, in preparation (2009).

Introduction on Er-based oxides

In the search of new high- k oxides, special attention has recently been devoted to doped HfO_2 [1,2]. Actually, small percentages of dopant elements have been demonstrated to stabilize the cubic and tetragonal phases of HfO_2 , thus enhancing its dielectric constant [3,4]. In particular, doping HfO_2 with a rare earth element has been calculated to stabilize the cubic phase for dopant percentages above 9.9% [5]. The case of Er-doped HfO_2 (Er- HfO_2) is of particular interest, since Er has one of the highest electron negativities and of the lowest ionic radii of the lanthanide serie, therefore reducing the tendency to form hydroxide compounds. The stabilization of the cubic phase in Er- HfO_2 has been recently demonstrated in layers obtained with different deposition techniques. Incorporation of 30% atomic Er by reactive sputtering [6], and physical vapor deposition of Er-doped (10–20%) HfO_2 lead to the obtainment of high k values (~28-30) associated with low EOTs and low leakage currents [7,8]. The introduction of a 3^+ element, such as Er, in the metallic sub-lattice may be accompanied by the concomitant formation of oxygen vacancies, therefore reducing the performances of the MOS or memory device. On the other hand, the insertion of substitutional Er could result in the softening of the infrared-active transverse optical phonon modes, therefore increasing the κ value of the doped compound [9].

In this work, Er/Hf-based oxides were thus proposed as variant of HfO_2 ; in these systems the idea was to achieve the stabilization of a high- k phase by means of selected Er doping.

The research conducted on the development of the ALD processes and on the characterization of the physical properties of Er/Hf-based oxides was divided in two main parts:

- development of ALD of a ternary ErHfO compound and investigation of the structural, chemical and electrical properties of a selected stoichiometry (i.e. Er ~15%)
- development of ALD processes to deposit Er-doped HfO_2 (variable Er content 1-15 %) and investigation of structural, chemical and electrical properties of the Er-doped HfO_2 compounds.

Atomic layer deposition of ErHfO

The main aim was to develop a proper ALD process suitable to obtain an actual ternary ErHfO compound. In this respect, a preliminary screening of the pure binary ALD processes for Er_2O_3 and HfO_2 was performed. Mainly, the effect of the deposition temperature on the growth rate and on film thickness uniformity was taken into account to evaluate the different ALD recipes and thus to identify the best process parameters. In the following sections of this chapter, brief summaries of the results obtained for ALD of Er_2O_3 and HfO_2 are presented. Subsequently, the development of a ternary ALD recipe is discussed focusing the attention on the structural and the chemical properties of the various oxides obtained with a different Er/Hf content.

Atomic layer deposition of Er_2O_3

Er_2O_3 films were grown using $\text{Er}(\text{}^i\text{PrCp})_3$ in combination either with H_2O or with O_3 . The H_2O -based process displayed very poor thickness uniformity: such issue was found to become even more relevant with the increase of the deposition temperature. For this reason H_2O was withdrawn as oxygen source, in combination with $\text{Er}(\text{}^i\text{PrCp})_3$, for ALD of Er_2O_3 . On the contrary, O_3 -based process displayed good thickness uniformity at 200 °C; a self limiting behavior was observed during the ALD pulses at the latter growth temperature. However, film thickness uniformity was found to worsen with the increase of the growth temperature due to the partial thermal decomposition of the $\text{Er}(\text{}^i\text{PrCp})_3$ molecules. Growth rates of all the investigated Er_2O_3 ALD processes are reported in Table 4.1. Data concerning the O_3 -based process are also shown in Figure 4.1; the growth rate values were determined from the center of the wafer.

Table 4.1: Summary of growth parameters and growth rates for ALD of Er_2O_3 films.

| Process | $T_{\text{source of Er}}$ (°C) | T_{growth} (°C) | Growth rate (Å/cycle) \pm 0.1 |
|--|--------------------------------|--------------------------|---------------------------------|
| $\text{Er}(\text{}^i\text{PrCp})_3 + \text{H}_2\text{O}$ | 150 | 200 | 0.6 |
| $\text{Er}(\text{}^i\text{PrCp})_3 + \text{H}_2\text{O}$ | 150 | 250 | 0.7 |
| $\text{Er}(\text{}^i\text{PrCp})_3 + \text{O}_3$ | 150 | 200 | 0.7 |
| $\text{Er}(\text{}^i\text{PrCp})_3 + \text{O}_3$ | 150 | 250 | 0.9 |
| $\text{Er}(\text{}^i\text{PrCp})_3 + \text{O}_3$ | 150 | 300 | 0.6 |

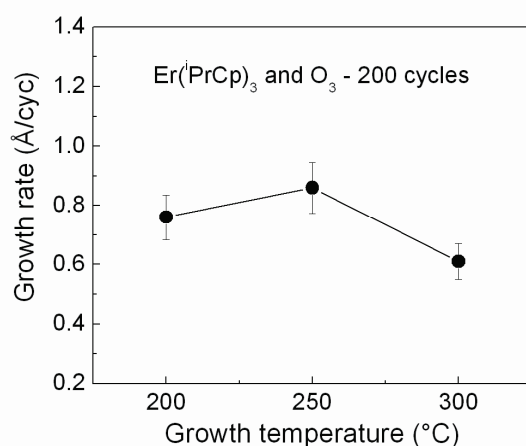


Figure 4.1: Growth rate as a function of the growth temperature for the O_3 -based process.

Atomic layer deposition of HfO₂

The HfO₂ ALD process was investigated on the basis of the results obtained for Er₂O₃. Therefore, the research was focused on the use of O₃ in order to develop an HfO₂ ALD cycle which could be easily integrated together with the Er₂O₃ ALD process, thus obtaining an O₃-based ErHfO ternary process. In Table 4.2 growth rates of the HfO₂ ALD process obtained at different temperatures are reported.

Table 4.2: Summary of growth parameters and growth rates of HfO₂ films.

| Process | $T_{\text{source of Hf}}$ (°C) | T_{growth} (°C) | Growth rate (Å/cycle) ± 0.1 |
|-------------------------|--------------------------------|--------------------------|-----------------------------|
| HfD-04 + O ₃ | 110 | 200 | 0.2 |
| HfD-04 + O ₃ | 110 | 250 | 0.4 |
| HfD-04 + O ₃ | 110 | 300 | 0.8 |

Figure 4.2 displays maximum, minimum and average thicknesses obtained for films grown at 200-300 °C. It turned out that thickness uniformity for this ALD process was very good regardless of growth temperature. However, the self-limiting behavior was achieved only at 300 °C whereas in the other cases the deposition rate appeared very poor.

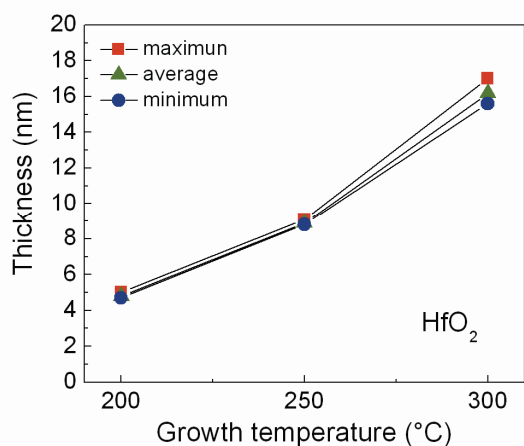


Figure 4.2: Maximum, minimum and average thickness of HfO₂ films deposited on 100 mm wafers in the 200 – 300 °C range.

In conclusion, the best reaction temperature which allowed the deposition of very uniform HfO₂ films was 300 °C; in well agreement with results reported in literature concerning the use of the same cyclopentadienyl-based Hf precursor [10,11]. On the basis of the latter results, a full O₃-based ALD process was investigated and characterized in order to develop and optimize ALD of a promising ternary ErHfO compound.

Atomic layer deposition of ternary ErHfO films

ErHfO films were grown using $\text{Er}(\text{PrCp})_3$ and HfD-04, respectively as Er and Hf source, and O_3 as oxygen source, thus alternating steps of Er_2O_3 and HfO_2 deposition. Films were deposited on 4" Si(100) wafers; pulses of carrier gas (N_2) were injected into the Er and Hf source cylinder to improve precursor vapour extraction. Er source temperature was set to 150 °C while Hf source temperature was set to 110 °C. Two different growth temperatures were investigated in combination with three different Er and Hf pulse ratio e.g., 1:1, 1:4 and 4:1. In Table 4.3 the growth rates of the ErHfO ALD processes are reported. When Er_2O_3 and HfO_2 are mixed together in a ternary ALD recipe, the growth rates of the single steps/ALD cycles ($\text{Å}/\text{O}_3$ pulse) may differ from the values expected for the pure binary processes and therefore also a new global growth rate ($\text{Å}/\text{ternary cycle}$) can be calculated.

Table 4.3: Summary of growth parameters and growth rates of ErHfO films.

| Process | Pulse ratio Er:Hf | T_{growth} (°C) | Growth rate ($\text{Å}/\text{ternary cycle}$) ± 0.1 | Growth rate ($\text{Å}/\text{O}_3$ pulse) ± 0.1 |
|---|----------------------|-----------------------------|--|---|
| 1[$\text{Er}(\text{PrCp})_3 + \text{O}_3$] + 1[$\text{HfD-04} + \text{O}_3$] | 1:1 | 200 | 1.0 | 0.5 |
| 1[$\text{Er}(\text{PrCp})_3 + \text{O}_3$] + 1[$\text{HfD-04} + \text{O}_3$] | 1:1 | 300 | 1.9 | 0.9 |
| 1[$\text{Er}(\text{PrCp})_3 + \text{O}_3$] + 4[$\text{HfD-04} + \text{O}_3$] | 1:4 | 200 | 1.3 | 0.3 |
| 1[$\text{Er}(\text{PrCp})_3 + \text{O}_3$] + 4[$\text{HfD-04} + \text{O}_3$] | 1:4 | 300 | 5.3 | 1.0 |
| 4[$\text{Er}(\text{PrCp})_3 + \text{O}_3$] + 1[$\text{HfD-04} + \text{O}_3$] | 4:1 | 200 | 3.1 | 0.6 |
| 4[$\text{Er}(\text{PrCp})_3 + \text{O}_3$] + 1[$\text{HfD-04} + \text{O}_3$] | 4:1 | 300 | 4.2 | 0.8 |

Figure 4.3 and Figure 4.4 show the maximum, minimum and average film thickness obtained for the ternary oxide grown with a pulse ratio of 1:4 and 4:1 at different temperatures.

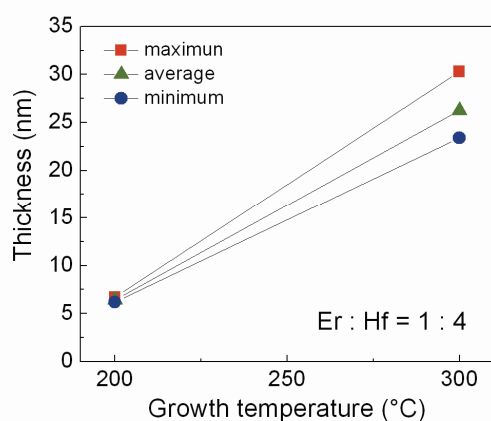


Figure 4.3: Maximum, minimum and average thickness of ErHfO films deposited on 4" Si(100) wafers at growth temperature 200–300 °C with an Er:Hf pulse ratio of 1:4.

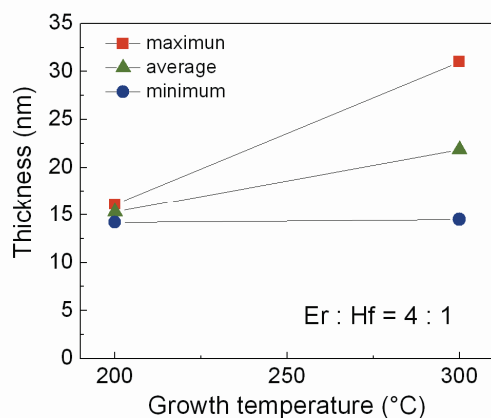


Figure 4.4: Maximum, minimum and average thickness of ErHfO films deposited on 4" Si(100) wafers at growth temperature 200–300 °C with an Er:Hf pulse ratio of 4:1.

Film thickness uniformity and growth rates are strongly dependent on the growth temperature. At a growth temperature of 200 °C, the HfD-04 molecule shows a very limited reactivity towards the substrate thus leading to a very low deposition rate of ~ 0.2 Å/cycle. On the contrary, the latter growth temperature appeared to be optimal for the ALD of Er_2O_3 . In fact, film thickness uniformity of ternary films grown at 300 °C is affected by the partial thermal decomposition of the $\text{Er}(\text{PrCp})_3$ molecules which may affect the ALD self-limiting behavior. Hence, the optimum growth temperatures for the binary oxides did not coincide, so that deposition of a uniform ternary film has to be pursued considering also this effect. Amongst the various Er/Hf-based ALD processes investigated, the combination based on $\text{Er}(\text{PrCp})_3$, HfD-04 and O_3 at a growth temperature of 300 °C, with an ALD pulse ratio Er:Hf = 1:4, turned out to appear as the most promising in order to deposit smooth and uniform films of a controlled stoichiometry. Films deposited from 125 cycles of $\text{Er}(\text{PrCp})_3$, HfD-04 and O_3 at different growth temperatures (Table 4.3) were analyzed by XRR, XRD and TXRF. A summary of the results is presented in Table 4.4. The chemical composition was determined by normalizing to 100 the sum of Hf and Er atomic content, being TXRF not able to determine neither light impurity like C, nor the O content. As expected, for a given pulse ratio, the Er content is higher when the growth temperature is lower. In the explored temperature range, the $\text{Er}(\text{PrCp})_3$ seems to be more reactive towards the substrate than HfD-04. Actually, at 300 °C up to 75% of Er can be incorporated in the film grown with a pulse ratio Er:Hf = 4:1, whereas only 50% of Hf can be incorporated in the film grown at 200 °C with a pulse ratio Er:Hf = 1:4. The electronic density value is influenced by both the Er/Hf ratio and the growth temperature. For similar chemical compositions, higher electronic density values are obtained for films grown at 300 °C. According to XRD, films grown at the latter temperature are crystallized in the as-deposited state while those grown at 200 °C are amorphous. The electronic density values, lower than those reported for films grown at 300 °C, might be associated to the amorphous nature of the film.

Table 4.4: Summary of growth parameters and growth rates of ErHfO films.

| Pulse ratio Er:Hf | T_{growth} (°C) | Chemical composition (at%) $\pm 2\%$ | Electronic density ($\text{e}^-/\text{\AA}^3$) ± 0.05 | Crystallization state |
|----------------------|--------------------------|---|--|--------------------------|
| 1:1 | 200 | Er: 81 ~ Hf: 19 | 1.44 | amorphous |
| 1:1 | 300 | Er: 40 ~ Hf: 60 | 2.37 | crystallized |
| 1:4 | 200 | Er: 50 ~ Hf: 50 | 1.93 | amorphous |
| 1:4 | 300 | Er: 15 ~ Hf: 85 | 2.43 | crystallized |
| 4:1 | 200 | Er: 95 ~ Hf: 5 | 1.42 | amorphous |
| 4:1 | 300 | Er: 75 ~ Hf: 25 | 2.07 | crystallized |

Figure 4.5 shows the diffraction patterns of the crystallized samples. All the diffraction patterns are compatible with the cubic, fluorite-like, structure of HfO_2 . However, the diffraction pattern of the film with the lowest Hf content presents also some features that can not be assigned to the fluorite-like HfO_2 . The film containing the highest Hf % has a lattice parameter in good agreement with the one reported in literature for cubic HfO_2 (5.06 Å as compared with 5.115 Å reported in database). Therefore, crystallization in a hafnia-based ternary $\text{Er}_{2x}\text{Hf}_{2-2x}\text{O}_{4-x}$ structure is suggested.

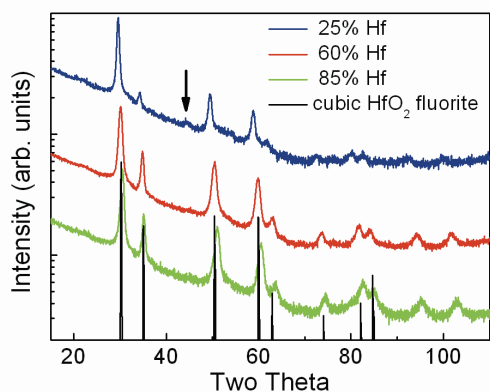


Figure 4.5: XRD analysis of crystallized, as deposited ErHfO films. The arrow indicates features not belonging to the fluorite structure.

The effect of a rapid thermal annealing at 900 °C in N_2 for one minute was investigated on all the films. The crystalline structure is stable in Hf-rich ($\text{Hf} \geq 50\%$) films grown at 300 °C, while the film grown at 300 °C using a Er:Hf = 4:1 pulse ratio shows a higher degree of crystallinity upon annealing. Figure 4.6 displays the Rietveld refinement of the diffraction pattern of the latter film performed using the bixbyite structure of Er_2O_3 and a lattice parameter of 10.38 Å. This refinement appears in good agreement with the experimental spectra, thus suggesting that crystallization takes place in an erbia-based ternary $\text{Er}_{2-2x}\text{Hf}_{2x}\text{O}_{3+x}$ structure.

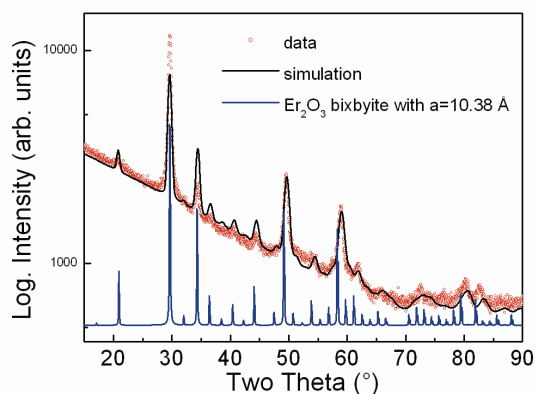


Figure 4.6: XRD analysis of film, grown at 300 °C with a Er:Hf = 4:1 pulse ratio, after annealing at 900°C. Red dots: experimental data. Black continuous line: Rietveld refinement. The positions of the peaks of the bixbyite structure, with a lattice parameter of 10.38 Å, are also reported.

In order to further investigate the effects of the post-deposition annealing on the properties of the ErHfO layers, a systematical XRR analysis was performed. The electronic density, as extracted by the fitting to the critical angle of the XRR data, is reported in Figure 4.7 for both as-grown and annealed films. The different crystallographic phases are also presented as a function of the chemical composition.

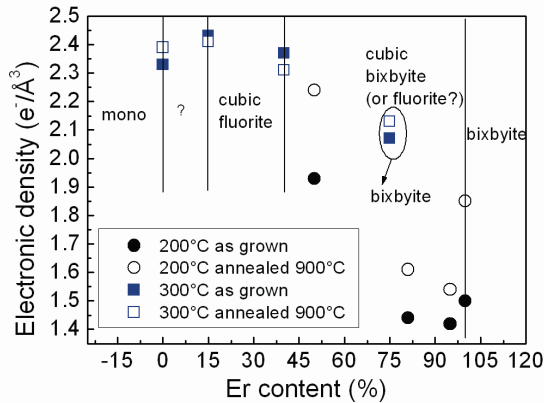


Figure 4.7: Electronic density plotted as function of the chemical compositions. The domains of the different crystallographic phases are identified.

However, three additional main factors that might directly influence the crystallization state should be also taken into account:

- the impurity content, that might be different depending on the deposition temperature
- the diffusion of Si atoms from the substrate, that might influence the crystallization state
- the thickness effect, since the analyzed layers were obtained with different growth rates depending on the specific deposition temperature

Characterization of ternary ErHfO films (Er content ~15%)

On the basis of a wide structural investigation of various ErHfO stoichiometries it can be concluded that the incorporation of 15% of Er stabilizes the cubic phase of HfO₂. Moreover, such a structure is maintained even after a high temperature annealing performed at 900 °C. Given this selected stoichiometry with Er content ~15%, a set of uniform ErHfO films was deposited by ALD on H-terminated Si(100) varying the film thickness in the 3-30 nm range by tuning the number of cycles between 25 and 300. All the deposited films were analyzed by XRD before and after annealing at 900°C. As-grown ErHfO films within the 8-33 nm thickness range are already crystallized, while films thinner than 8 nm are amorphous. Crystallization of ErHfO occurs in the fluorite cubic structure with a lattice parameter, as extracted from Rietveld refinement, equal to 5.06 ± 0.01 Å. Figure 4.8 shows the variation with RTA at 900 °C of the diffraction patterns of ErHfO. The cubic phase is maintained after annealing for films thicker than 8 nm. RTA induces the crystallization in films thinner than 8 nm also within the cubic structure. Annealing induces a modification of the intensity and shape of the diffracted maxima. Taking into account the reduction of thickness due to densification occurring in annealed films, Rietveld refinement suggests that upon annealing an increase of grain size is accompanied by the reduction of microstrain.

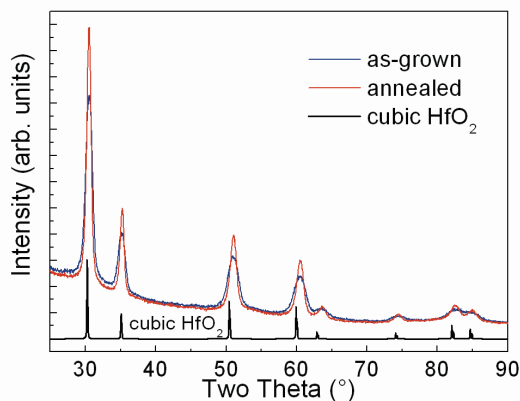


Figure 4.8: GIXRD patterns of as grown (blue) and annealed (red) nominally 30 nm thick ErHfO on H-terminated Si(100).

Two ErHfO films, grown with a nominal thickness of 3 and 10 nm, were analyzed by HRTEM and STEM-EELS (Figure 4.9) in the as-grown and annealed state. The structural thicknesses of the different layers constituting the stacks are reported on the figures. An amorphous and extended IL of clear contrast is formed atop the Si substrate. The thickness of this “structural” IL is around 1.4 ± 0.3 nm for the as-deposited films and increases up to 2.3 ± 0.3 nm after annealing at 900 °C. Concurrently, the thickness of the crystalline layers decreases upon annealing, due to the densification of the ErHfO layer and a corresponding increase of grain size within 40%.

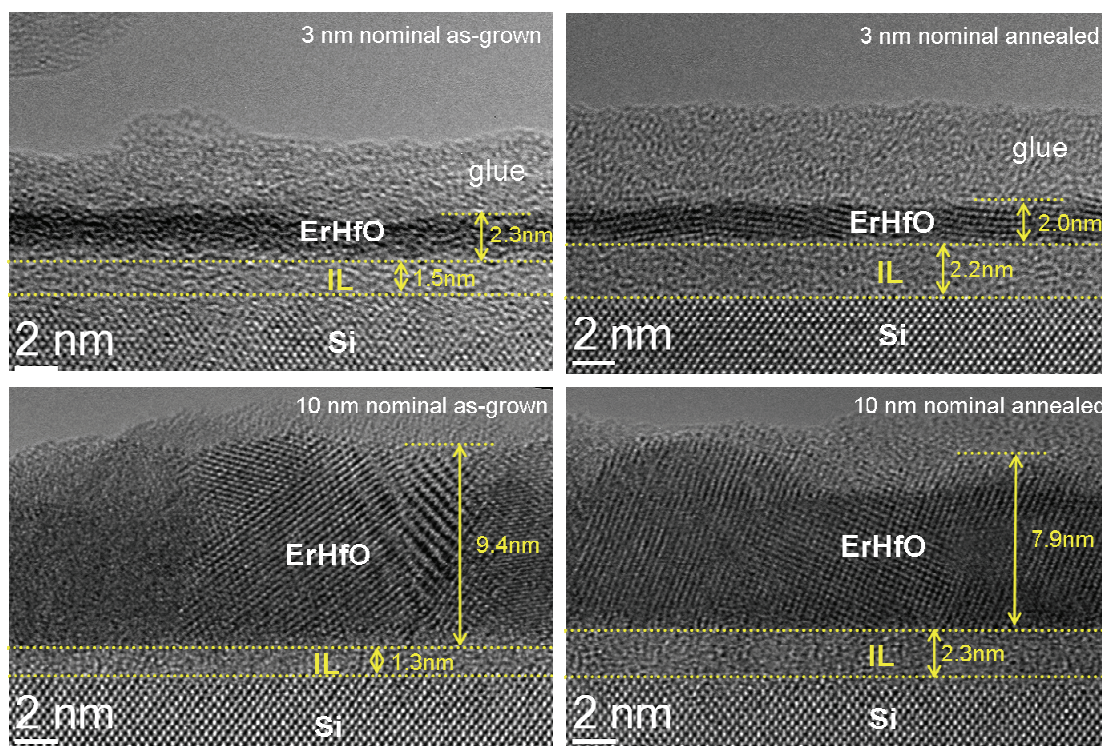


Figure 4.9: Atomic structure images of cross-section samples from ErHfO_x films deposited on Si.

The “chemical” IL thickness, defined by the extent of the Si elemental profile within the film, is similar for the as-grown and annealed films and for both thicknesses, being around 3.5 nm.

Figure 4.10 illustrates the case for the 10 nm thick annealed film.

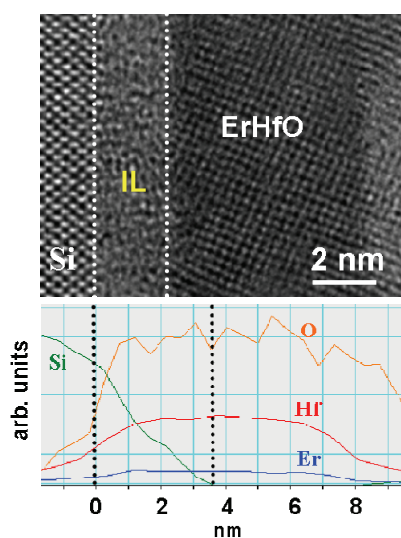


Figure 4.10: HRTEM cross sectional image and corresponding STEM-EELS chemical profiles of nominally 10 nm thick film annealed at 900 °C.

Information about the k of the ErHfO (Er ~15%) can be deduced from the C-V characteristics acquired on MOS capacitors fabricated using as-grown and annealed films (Figure 4.11).

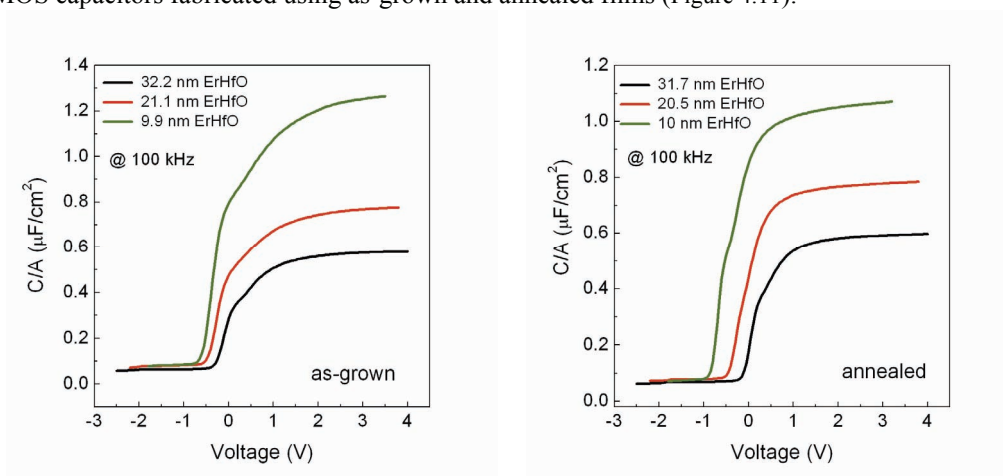


Figure 4.11: C-V curves acquired at 100 kHz on MOS capacitors fabricated using as-grown (left panel) and annealed (right panel) ErHfO films of different thickness.

From the plot of the CET vs the ErHfO thickness, deduced combining XRR and SE measurements, a k value of 27 ± 1 can be extracted for as-grown samples (Figure 4.12). The intercept of the linear fit with the CET y-axis reveals the presence of an IL with an EOT of 1.6 ± 0.1 nm. The EOT of the IL deduced from the electrical characterization is smaller than its physical thickness that can be deduced by the combination of SE and XRR measurements and by the HRTEM/STEM-EELS analysis. This finding is an indication that the k value of the IL should be slightly larger than that of SiO₂. This suggests the chemical composition of the IL being silicate-like. In fact, as evidenced by STEM-EELS profiles in Figure 4.10 the IL contains not only Si and O, but also Er and Hf species.

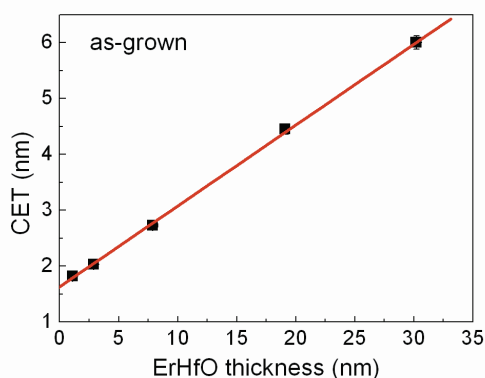


Figure 4.12: Plot of CET vs ErHfO thickness of the as-grown films.

After annealing, the k value of the ErHfO film increases up to 33 ± 1 (Figure 4.13). This effect might be associated to an increase of oxide crystallized fraction as revealed also by XRD and TEM analysis. The EOT of the IL increases up to 2.3 ± 0.1 nm, in fair agreement with the increase of the thickness of the IL observed by structural/chemical measurements performed using HRTEM/STEM-EELS.

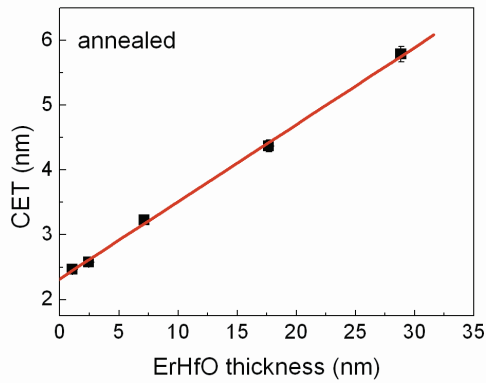


Figure 4.13: Plot of CET vs ErHfO thickness for annealed films.

From the dependence of the stack capacitance on the oxide thickness, the k value of the IL can be more accurately deduced. In the as-grown state the IL shows $k \sim 4.4$ - 4.9 , while after annealing k increases up to $k \sim 4.8$ - 5.1 . As far as the carrier transport through the oxide is concerned, the leakage current is acceptable for sample thicknesses above 10 nm ($J = 5 \times 10^{-7}$ A/cm² at +1 V from V-flatband). For samples thinner than 10 nm the leakage current strongly increases. This effect is more remarkable after annealing, as depicted in Figure 4.14(a) and Figure 4.14(b).

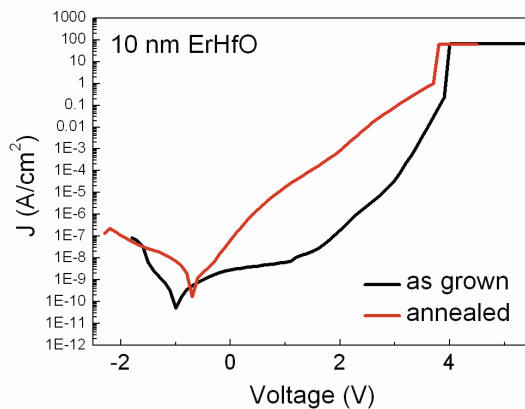


Figure 4.14: Leakage current before and after annealing for the 10 nm thick film.

It has been demonstrated that it is possible to stabilize both the hafnia-based $\text{Hf}_{2-2x}\text{Er}_{2x}\text{O}_{4-x}$ and the erbia-based $\text{Er}_{2-2x}\text{Hf}_{2x}\text{O}_{3+x}$. Moreover, no evidence of the pyrochlore structure (i.e. stable for the $\text{Hf}_2\text{La}_2\text{O}_7$ system) was found for these ternary oxides. All the films were polycrystalline already in the as-grown state and the cubic phase of HfO_2 can be identified without any dependence on the film thickness. By the combination of SE, XRR and HRTEM an IL between the high- k oxide and Si(100) can be detected; a thickness of 2 ± 0.5 nm was determined for the as-grown samples. Annealing induced an increase of the crystallized fraction of cubic HfO_2 and a corresponding reduction of microstrain; at the same time an increase of the IL thickness to 3 ± 0.5 nm was revealed by XRR and SE. ToF SIMS confirmed the presence of the IL and that its thickness increases upon annealing. From the chemical depth profiles it was also possible to appreciate a uniform Er content along the film thickness therefore proving a homogenous film stoichiometry while from STEM-EELS analysis a silicate-like chemical composition of the IL was revealed. Electrical measurements performed on as-grown samples revealed a k value of 27 ± 1 which is increased to 33 ± 1 by the annealing process.

Atomic layer deposition of Er-doped HfO₂

The chemical composition within the Er₂O₃-HfO₂ system was varied in order to investigate the dependence of the physical properties with the Er content. Er-doped HfO₂ films with a variable Er and Hf pulse ratio (from 1:8 up to 1:30) were grown by ALD at 300 °C using Er(ⁱPrCp)₃, HfD-04 and O₃ species. All the films were deposited targeting a film thickness in the 10–15 nm range in order to obtain a consistent set of films. Slight modifications of the growth rate were induced, as expected, by the variations of the pulse ratio and therefore of the ALD recipe. Our preliminary study (see previous sections of this Chapter) showed that the stabilization of the cubic phase of HfO₂ by Er-doping takes place in a wide range of chemical compositions above Er ~15%. Since the cubic phase of HfO₂ is expected to have a high dielectric constant (~29 [12]), we carefully investigate the variation of structural properties of Er-doped HfO₂ also varying the Er content within the 1-13% range. Films were subjected to a post-growth RTA in vacuum for 60 s at 900 °C. TXRF was used to determine the Hf/Er ratio in all the as-grown samples (Table 4.5).

Table 4.5: TXRF analysis performed on the as-grown Er-doped HfO₂ films.

| Er:Hf ratio | SE thickness (nm) | Er % at | Hf % at |
|-------------|-------------------|---------|---------|
| 1 : 8 | 17.5 | 12.8 | 87.2 |
| 1 : 10 | 10.6 | 9.7 | 90.3 |
| 1 : 12 | 11.6 | 8.2 | 91.8 |
| 1 : 15 | 14.8 | 4.1 | 95.9 |
| 1 : 30 | 12.8 | 1.5 | 98.5 |

Figure 4.15 shows the Er content incorporated in the HfO₂ as a function of the Er/Hf ALD pulse ratio.

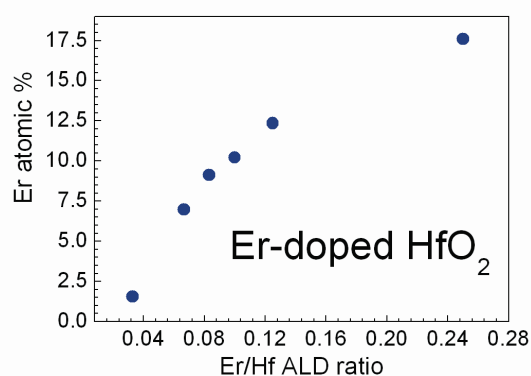


Figure 4.15: TXRF analysis performed on the set of Er-doped HfO₂ films.

ToF SIMS depth profiles acquired on the whole set of films, including pure HfO₂, corroborated the results provided by TXRF analysis. As displayed in Figure 4.16, the intensities of the ErO signal acquired in the films grown targeting a different Er doping actually scale from 0% (pure HfO₂) up to 12.8% (Er:Hf = 1:8).

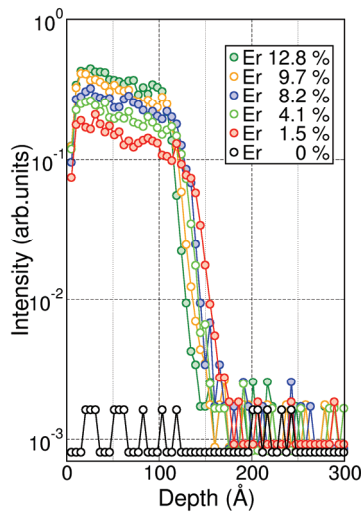


Figure 4.16: ToF SIMS depth profiles acquired on the set of Er-doped HfO₂ films. The different signal intensities are related to different Er contents within the films. The profile of pure HfO₂ (Er% = 0) is also reported as a comparison.

XRD and XRR were performed on both as-grown and annealed samples deposited on H-terminated Si(100). All the as-grown layers are smooth and uniform; the presence of an IL at the oxide/Si(100) interface can be revealed by means of combined XRR and SE analysis. XRR analyses, performed before and after annealing at 900 °C in N₂, reveal an increase of the electronic density and a reduction of the total thickness that likely correspond to the shrinking of the Er-HfO₂ layer. It is worthy to notice that the higher is the Er content, the more relevant appears the increase of the electronic density upon annealing. The structural evolution as a function of the Er content is discussed on the basis of the XRD diffraction patterns reported in Figure 4.17.

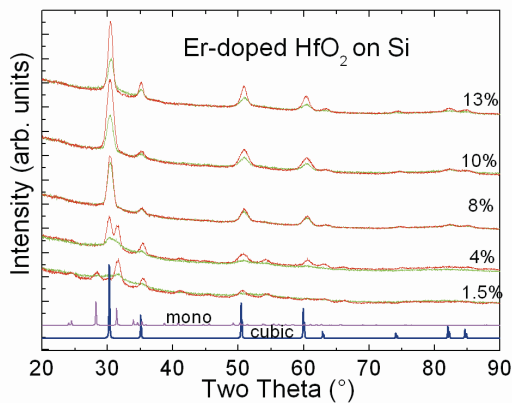


Figure 4.17: XRD analysis of as-grown (green) and annealed (red) Er-HfO₂ samples. The peak positions of cubic (blue) and monoclinic (magenta) HfO₂ are also added for comparison.

All the analyzed films are already crystallized in the as-grown state. For Er content within 8-13%, crystallization takes place in the cubic phase of HfO₂. The film containing ~4% Er presents a mixture of monoclinic and cubic crystalline phases of HfO₂ in the as-grown state. After annealing, the monoclinic contribution noticeably increases. This finding reveals that, for this level of Er inclusion around 4%, the stabilization of the cubic polymorph is not fully accomplished in the as-deposited film, and consequently even less efficient upon annealing.

The film with an Er percentage of ~1.5% presents a more complicated crystallographic structure, with smaller grain size and/or higher microstrain than the other stoichiometries. A detail of the spectra of as-grown and annealed film with 1.5% Er is presented in Figure 4.18.

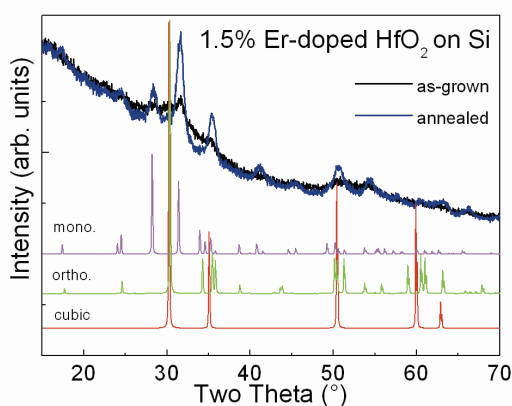


Figure 4.18: XRD analysis of 1.5% Er-HfO₂. As-grown (black) and annealed (blue) state.

The Rietveld refinement reveals that the as-grown sample is crystallized in a mixture of monoclinic and cubic (also possibly orthorhombic or tetragonal) phases. It should be remarked that, by means of XRD analysis, it is not possible to distinguish between cubic, orthorhombic or tetragonal phases. The amount of monoclinic phase that is present can be quantified around 70-80%, with an evidence of preferential orientation. For the 10% and 13% Er-doped samples, annealing induces a major development of the cubic phase of HfO₂, as already evidenced for higher Er content. Rietveld refinement, performed taking into account the different layer thickness, gives a microstrain of 2.1% and 1.8% for the 13% and 10% Er-HfO₂, respectively. Considering also the result of a microstrain of 2.8% obtained for the 15% Er-doped sample, we can argue that the microstrain diminishes reducing the Er content, in agreement with the scenario of a less distorted crystalline lattice. For the film doped with 8% of Er, the cubic phase is present both before and after annealing. However, annealing induces only a minor increase of the crystallization. After annealing, the film doped with the lowest Er content (i.e. 1.5%) is found to be crystallized mostly in the monoclinic phase of HfO₂. In this case also the cubic phase can be identified; its contribution to the diffraction pattern can be quantified around 15-20%. Given the aforementioned systematical study of the evolution of the structural properties as a function of the Er doping, an outstanding correlation would come from the study of the k values of the various Er-doped HfO₂ films. However, the study of the dependence of the k value on the doping level is an extremely challenging task on a single sample. Indeed, the thicknesses of the IL and of the high- k layer and the k value of the IL should be known. For this reasons, only a preliminary evaluation of the k value of the full stacks was possible. A preliminary analysis (data not shown) reveals that for Er doping concentrations below 8% the films appear characterized by a relatively small k values of the stack if compared to the ones calculated for films that include more Er. This finding is consistent with the XRD observations that films with Er content higher than 8% crystallize in a cubic phase, while films doped with an Er% <8% present an mixture of various crystalline phases. Moreover, this trend is in line with the fact that the cubic HfO₂ phase is characterized by a higher permittivity value than the one expected for the monoclinic polymorph [12,13].

References

- [1] J. Niinisto, K. Kukli, M. Heikkila, M. Ritala, and M. Leskela, *Adv. Eng. Materials*, **11**, 223 (2009).
- [2] P. R. Chalker, M. Werner, S. Romani, R. J. Potter, K. Black, H. C. Aspinall, A. C. Jones, C. Z. Zhao, S. Taylor, and P. N. Heys, *Appl. Phys. Lett.* **93**, 182911 (2008).
- [3] D. Fischer, A. Kersch, *Appl. Phys. Lett.* **92**, 012908 (2008).
- [4] W. He, L. Zhang, D. S. H. Chan, and B. J. Cho, *IEEE El. Dev. Lett.* **30**, 623 (2009).
- [5] C. K. Lee, E. Cho, H. S. Lee, C. S. Hwang, and S. Han, *Phys Rev B* **78**, 012102 (2008).
- [6] J. Chen, X. P. Wang, M-F. Li, S. J. Lee, M. B. Yu, C. Shen, Y. C. Yeo, *IEEE El. Dev. Lett.* **28**, 862 (2007).
- [7] S. Govindarajan, T. S. Böske, P. Sivasubramani, P. D. Kirsch, B. H. Lee, H. H. Tseng, R. Jammy, U. Schröder, S. Ramanathan, B. E. Gnade, *Appl. Phys Lett.* **91**, 062906 (2007).
- [8] S. Ramanathan, A. Karthikeyan, S. A. Govindarajan and P. D. Kirsch, *Journal Vac. Sci. Technol. B* **26**, L33 (2008).
- [9] G. Dutta, *Appl. Phys. Lett.* **94**, 012907 (2009).
- [10] J. Niinisto, M. Putkonen, L. Niinisto, F. Song, P. Williams, P. N. Heys, and R. Odedra, *Chem. Mater.* **19**, 3319 (2007).
- [11] K. Kukli, J. Niinistö, A. Tamm, J. Lu, M. Ritala, M. Leskelä, M. Putkonen, L. Niinistö, F. Song, P. Williams, P. N. Heys, *Microelectr. Eng.* **84**, 2010 (2007).
- [12] X. Zhao and D. Vanderbilt, *Phys. Rev. B* **65**, 233106 (2002).
- [13] D. Vanderbilt, X. Zhao, D. Ceresoli, *Thin Solid Films* **486**, 125 (2005).

Chapter 5

High- k oxides on high-mobility substrates*

*Results published and to be published as:

L. Lamagna, C. Wiemer, S. Baldovino, A. Molle, M. Perego, S. Schamm, P. E. Coulon, and M. Fanciulli, *Appl. Phys. Lett.* **95**, 122902 (2009).

A. Molle, G. Brammertz, L. Lamagna, M. Fanciulli, M. Meuris, and S. Spiga, *Appl. Phys. Lett.* **95**, 023507 (2009).

A. Molle, L. Lamagna, S. Spiga, G. Brammertz, M. Meuris, and M. Fanciulli, *Thin Solid Films*, in press (2009).

L. Lamagna *et al.*, “*O3-based atomic layer deposition of hexagonal La_2O_3 on Si and Ge*”, in preparation (2009).

Introduction on high- k oxides on high-mobility substrates

Coupling a high-mobility channel (e.g. Ge and III-V compounds) with a high- k dielectric represents an extremely promising strategy for the fabrication of advanced ultra-scaled devices. However, this approach still encompasses numerous technological and scientific concerns [1]. In addressing the integration of RE-based high- k oxides on high-mobility semiconductor substrates, this chapter is composed by three main parts focusing respectively on:

- ❖ La-based oxides grown by ALD on Ge(100)
- ❖ Er-based oxides grown by ALD on Ge(100)
- ❖ La-doped ZrO₂ grown by ALD on III-V compounds

In the first part, the integration of two La-based oxides (i.e. La₂O₃ and La-doped ZrO₂) grown on Ge substrates using ALD is presented. A particular attention is dedicated to La₂O₃/Ge interfaces. The La₂O₃/Ge stack is discussed addressing the stabilization of the h -La₂O₃ phase (see also Chapter 3) and the formation of a lanthanum germanate compound at the interface. The structural and electrical properties of La-doped ZrO₂ on Ge(100) are discussed focusing on the effects of the post-deposition thermal treatment on the dielectric constant of the material.

Latterly, an overview on the physical properties of thin Er-based oxides films deposited by ALD on Ge(100) is presented. The discussion is either focused on the properties of the stoichiometry characterized by the highest Er content (i.e. 15 %) and on the effects of the different Er content on the stabilization of the HfO₂ cubic phase.

In the last part of the chapter, some selected highlights concerning the ALD of La-doped ZrO₂ thin films on III-V semiconductor substrates are presented. In particular, interface chemical details and the effects of the intercalation of a Ge ultra thin layer between the high- k oxide and the III-V substrate are discussed with regard to the electrical passivation of interface defects.

La₂O₃ on Ge(100)

“O₃-based atomic layer deposition of hexagonal La₂O₃ on Ge(100)” [2]

All the films were grown in the Savannah 200 ALD reactor on 4” H-terminated n-type Si(100) and native oxide free n-type Ge(100) wafers. Removal of GeO₂ was achieved with a 30 s dip in a diluted HF solution (HF:H₂O=1:25), at room temperature, followed by a rinse in deionized water. La₂O₃ films were deposited at a growth temperature of 200 °C alternating pulses of La(ⁱPrCp)₃ and O₃; layers thickness was tuned varying the number of ALD cycles. ALD cycle structure was composed of 15 s La(ⁱPrCp)₃ pulse / 8 s purge with N₂ / 0.015 s O₃ pulse / 6 s purge with N₂. La source (supplied by SAFC Hitech) was kept at 150 °C; O₃ was obtained starting from ultra pure O₂ and was injected into the reactor at a concentration of ~200 g/Nm³. Film thickness was estimated by SE. In Table 5.1 is reported the list of as-grown and annealed samples and all the thicknesses values.

Table 5.1: Details of as-grown and annealed La₂O₃ films grown on native oxide free Ge(100).

| Sample | Stack | Thickness as-grown (nm) | RTA | Thickness after RTA (nm) |
|--------|-------------------------------------|-------------------------|----------------|--------------------------|
| G1 | n-Ge/La ₂ O ₃ | 20.4 | @400 °C in vac | 14.6 |
| G2 | n-Ge/La ₂ O ₃ | 14.8 | @400 °C in vac | 9.1 |
| G3 | n-Ge/La ₂ O ₃ | 10.0 | @400 °C in vac | 6.8 |
| G4 | n-Ge/La ₂ O ₃ | 5.6 | @400 °C in vac | 3.8 |

GIXRD analysis is performed on both as-grown and annealed La₂O₃ films in order to address the evolution of the crystallographic structure.

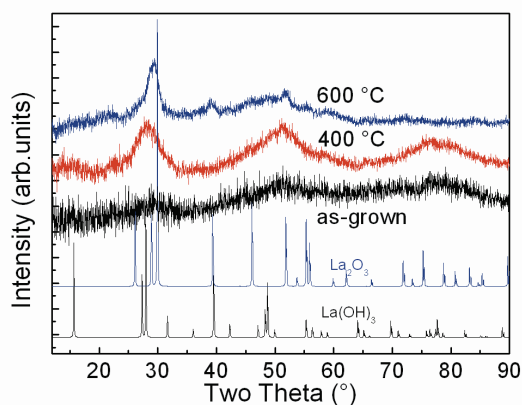


Figure 5.1: GIXRD analysis of 20 nm thick sample on Ge after annealing at different temperatures. The powder patterns of hexagonal La(OH)₃ [3] and La₂O₃ [4] are also added for comparison.

No clear evidence of crystallographic ordering is found in the as-grown sample (Figure 5.1), probably related to the absence of any long range order due to the mixture of different stoichiometries within the La(OH)₃. Differently, a single broad peak in the two theta ~29° region is visible after RTA at 400 °C. The 2theta position of this peak corresponds to the increase of the long range order within the La₂O₃ phase, in particular to the stabilization of La-La and La-O bonds. Annealing at 600 °C promotes the crystallization of the La₂O₃ layer in its hexagonal phase. The lattice parameters extracted from the Rietveld refinement of the GIXRD data are $a = 3.96 \pm 0.01 \text{ \AA}$ and $c = 6.26 \pm 0.01 \text{ \AA}$, slightly higher than those obtained for the films deposited using the same ALD recipe (see Chapter 3) on H-terminated Si(100), after annealing at the same temperature. The electron density profiles extracted by simulating the XRR curves of as-grown and 400 °C annealed samples are shown in Figure 5.2. Also in this case, as already discussed for films deposited on H-terminated Si(100), the as-grown layers are mainly

composed by La hydroxide formed upon air exposure by the incorporation of OH groups. Upon RTA performed in vacuum, the density of the La-based layer is found to increase up to a value being comparable to the one reported for crystallized *h*-La₂O₃.

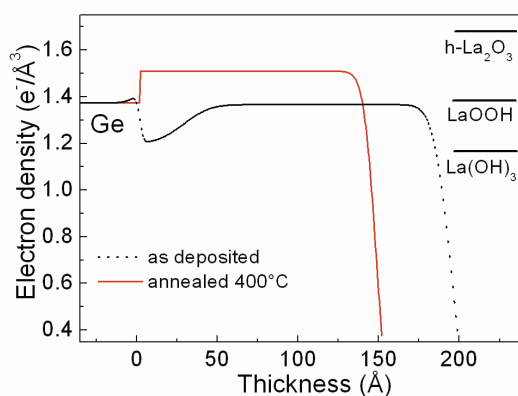


Figure 5.2: XRR Electron density profiles extracted from the simulation of XRR data for as grown (dotted line, black) and 400°C annealed (continuous line, red) nominally 20 nm thick sample on Ge.

However, for the as-grown state XRR reveals a decrease of the electron density close to the interface with Ge, that might be related to the partial oxidation of the Ge substrate. Differently, in Figure 5.2 (red line) the value of the electron density extracted after annealing appears uniform. This finding might be tentatively explained with the hypothesis that the electronic density of the LaGeO specie, that is likely forming at the oxide/Ge(100) interface upon annealing, is very similar to the electronic density of the La₂O₃ polymorphs. Actually, the electron density values reported for crystallized lanthanum germanates vary in the 1.38-1.45 e⁻/Å³ range. Therefore, from the electronic density profiles it is not possible to distinguish between the LaGeO specie and the *h*-La₂O₃. Additional structural information with nanometric-scale resolution is provided for both as-grown and annealed La₂O₃ films by HRTEM analysis. Figure 5.3 shows HRTEM image for an annealed La₂O₃ film deposited on Ge(100).

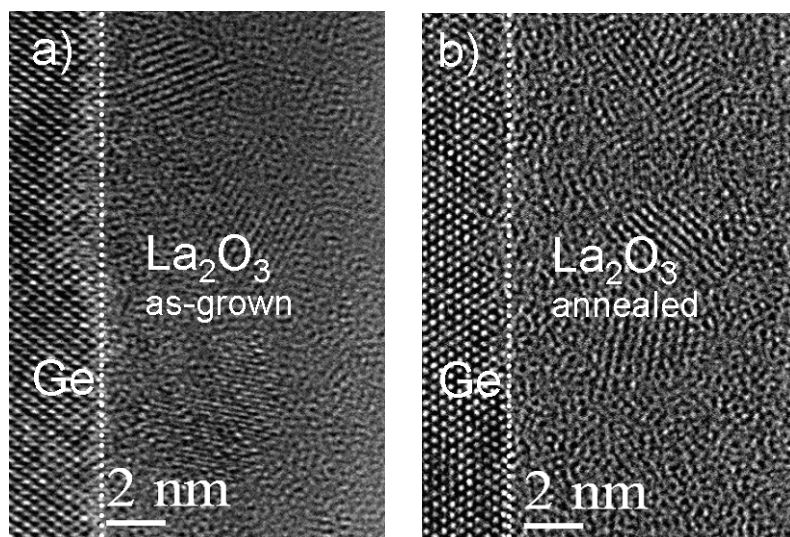


Figure 5.3: HRTEM cross sections of a 10 nm thick (a) as-grown and (b) annealed La₂O₃ film. Dotted white lines are a guide for the eyes to visualize the borderline between the substrate and the film.

It is not possible to clearly identify a “structural” amorphous IL neither in the as-grown film Figure 5.3(a), nor in the annealed one Figure 5.3(b). Nanocrystals can be identified in both cases. However, the presence of nanocrystals is more evident after annealing, in agreement with an increase of the crystalline order suggested by GIXRD analysis. In order to assess the chemical composition of the La_2O_3 layer grown on Ge(100), ToF SIMS depth profiles were acquired on sample G2 in the as-grown state and after annealing at 400 °C.

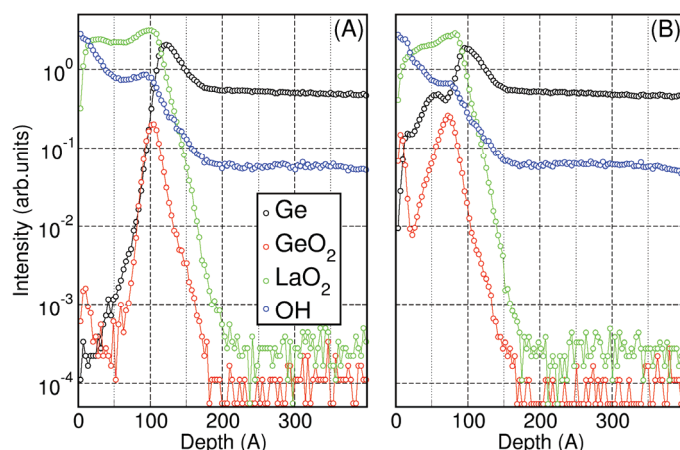


Figure 5.4: ToF SIMS chemical depth profiles acquired on 10 nm thick film (A) as-grown and (B) annealed at 400 °C.

In Figure 5.4(A) the intense GeO_2 signal at the $\text{La}_2\text{O}_3/\text{Ge}$ interface indicates the presence of a Ge-rich IL in the as-grown sample. No intense Ge related signals have been detected at the surface of the La_2O_3 film, suggesting a limited Ge diffusion during ALD process. As expected, in the as-grown state the shape of the OH⁻ profile suggests the presence of a relevant hydroxide component in the film. After annealing at 400 °C (Figure 5.4(B)), the OH⁻ profile is only slightly modified. As already demonstrated for the $\text{La}_2\text{O}_3/\text{Si}(100)$ stack, such low thermal budget is not sufficient to effectively promote the removal of the $\text{La}(\text{OH})_3$ component. After annealing Ge and GeO_2 signals appear more extended into the oxide layer indicating that Ge diffusion has occurred during the thermal treatment. Therefore, ToF SIMS reveals the presence of a “chemical” IL either before or after RTA. A graded Ge profile inside the La_2O_3 layer is revealed hence resulting in a non-uniform Ge atoms distribution along the thickness of the film. Although annealing at temperatures higher than 400 °C are not technologically suitable on Ge substrates, we believe that a higher post-deposition annealing temperature or a longer annealing time would probably lead to the formation of a full germanate-like layer promoting the diffusion of Ge atoms through the whole film thickness.

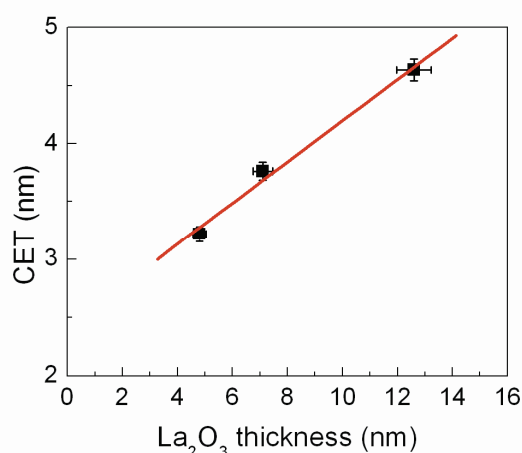


Figure 5.5: CET plot vs La_2O_3 physical thickness.

From the CET vs. La_2O_3 thickness plot (Figure 5.5), a k value of 22 ± 1 is calculated for the set of annealed films. This value, although slightly smaller, appears to be in fairly good agreement with the k calculated for films deposited on H-terminated Si(100). The difference can be associated to more efficient conversion of the hydroxide layer into a full $h\text{-La}_2\text{O}_3$ structure which occurs in the $\text{La}_2\text{O}_3/\text{Si}(100)$ stacks annealed at 600 °C. In these Ge-based stacks the identification of a clear IL is extremely complex. The k value was extracted reasonably assuming a 2 nm thick IL and thus calculating an the La_2O_3 thickness. However, the extraction of the dielectric constant is not affected by this assumption. On the contrary, the discussion of the CET intercepts with the y -axis must be extremely carefully addressed because of the uncertainties on the thickness and k of the IL that is formed upon annealing.

La-doped ZrO₂ on Ge(100)

“Thermally induced permittivity enhancement in La-doped ZrO₂ grown by atomic layer deposition on Ge(100)” [5]

Amongst the oxides investigated for high- k /Ge stack application, ZrO₂ has been broadly proved to be a promising insulator. Numerous results have been presented for ZrO₂/Ge stacks grown by sputtering [6,7] atomic layer deposition (ALD) [8,9,10] and ultra-high vacuum molecular beam deposition (MBD) [11]. Interface engineering still remains an outstandingly open issue as the Ge/oxide interface exhibits an unacceptably large density of interface traps (D_{it}) which can be related to the evidence of Ge dangling bond interface defects [12,13]. A broad range of solutions has been considered such as Ge controlled oxidation [9,14] and deposition of ultra-thin passivating interfacial layers (IL) [15].

Recently, a study on ZrO₂/GeO₂ stacks prepared by atomic oxygen-assisted MBD [11] correlates a very high k value (~ 44) with the promotion of tetragonal ZrO₂. Indeed, the observation of such large k is there associated to Ge incorporation into the ZrO₂ arising from the thermal decomposition of the GeO₂ IL throughout the overlying oxide. In our work, we focused on O₃-based ALD of La-doped ZrO₂ (La-ZrO₂) on bare Ge(100) therein targeting the growth of a high- k material, with a moderately defective interface, through a direct deposition approach without interposing any IL. The physical properties of the as-grown and annealed La-ZrO₂ films and their mutual implications were characterized by means of: (i) high resolution transmission electron microscopy (HRTEM) coupled to electron energy-loss spectroscopy (EELS) and selected area electron diffraction (SAED), (ii) X-ray photoemission spectroscopy (XPS), (iii) time of flight secondary ion mass spectroscopy (ToF SIMS), (iv) capacitance-voltage (C-V) measurements. La-ZrO₂ films were grown at 300 °C in a Savannah 200 ALD reactor (Cambridge Nanotech Inc.) on n-type Ge(100). Native GeO₂ was removed using a diluted HF solution (1:25). La incorporation in ZrO₂ ($\sim 5\%$ mean value) aims to enhance the k value, according to the effect of dopants on dielectric properties of high- k oxides [16,17]. Moreover, incorporation of La at the interface can favor the formation of La–O–Ge bonds, thus preventing the developing of Ge suboxides and reducing the electrical defects [18,19]. In this respect, O₃ oxidation was also demonstrated to opportunely passivate Ge interface [20,21]. These findings motivate our choice to start the ALD with a La₂O₃ step and to choose O₃ (~ 200 g/Nm³) as oxidizer. The metal sources were (¹PrCp)₃La and (MeCp)₂ZrMe(OMe) (SAFC Hitech). The ALD cycle number varied from 8 to 80, stack thickness was estimated using Spectroscopic Ellipsometry and X-ray reflectivity (XRR) in the 3-30 nm range. La doping was tuned altering the La and Zr pulse ratio. Postgrowth rapid thermal annealing (RTA) was performed for 60 s in N₂ at 400 °C.

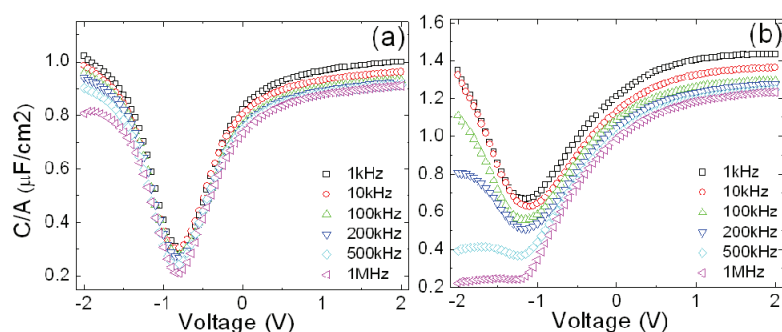


Figure 5.6: (a) C-V characteristics for Al-gate (0.85×10^{-5} cm²) MIS capacitors fabricated from a 14.5 nm thick as-grown sample and (b) from a 14.4 nm thick annealed sample.

Room temperature C-V measurements were performed on metal insulator semiconductor capacitors; capacitance equivalent oxide thickness (CET) was determined from the accumulation capacitance (C_{acc}) at 100 kHz. Figure 5.6(a) illustrates multifrequency C-V curves obtained for a 14 nm thick as-grown La-ZrO₂ film. Only weak frequency dispersion is observed both in accumulation and depletion, indicating a relatively low D_{it} ($\sim 8 \pm 1 \times 10^{11}$ eV⁻¹cm⁻² evaluated with the Hill-Coleman method [22] at

500 kHz). The overall k of the as-grown stack can be calculated from the C_{acc} by applying a single-layer capacitor model; with this approach a $k=18\pm 1$ is estimated. Figure 5.6(b) displays multifrequency $C-V$ curves obtained for a 14 nm stack annealed. A clockwise hysteresis of 550 and 850 mV, for the as-grown and annealed case respectively, is measured. $C-V$ curves appear more stretched and only a moderate increase of the D_{it} up to $\sim 2 \pm 1 \times 10^{12} \text{ eV}^{-1} \text{ cm}^{-2}$ can be observed. After annealing the C_{acc} is noticeably higher than the one related to the as-grown state thus suggesting a significant impact of the RTA on the dielectric features of the oxide. Applying a capacitor model a $k = 21 \pm 1$ for the annealed stack is calculated.

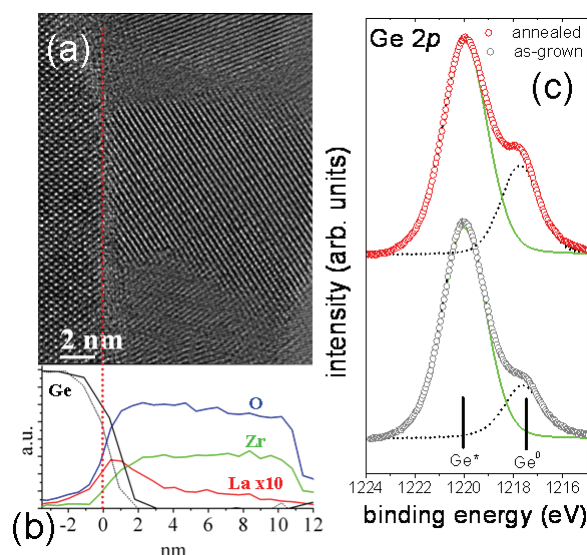


Figure 5.7: (a) HRTEM cross section of annealed La-ZrO₂ film (14 nm). (b) STEM-EELS profiles for the as-grown (dotted line) and annealed (plain line) case. For clarity, only the Ge profile is shown for the as-grown case since Zr, O, and La profiles remain almost stable upon annealing. (c) Ge 2p XPS lines of the as-grown and annealed 3 nm thick La-ZrO₂ film.

To understand the dielectric behavior modifications, a structural and chemical investigation of the interface between Ge(100) and La-ZrO₂ and within the film was performed at the nanometric level with HRTEM and EELS on the 14 nm thick sample before and after RTA. As-grown films are crystalline for all the analyzed thicknesses, as also proved by X-ray diffraction (not shown), with a predominant cubic (c -) and/or tetragonal (t -) phase of ZrO₂ which can not be directly assigned (Figure 5.8(c)). Differently from what reported for La_{0.25}Zr_{0.75}O_{2-δ} [23] the very low La content does not promote the amorphization of the ZrO₂ matrix. A direct contact between the La-ZrO₂ crystals and Ge(100) is observed in Figure 5.7(a) also after RTA. Consequently, there is no IL from the structural point of view. However, a chemical interfacial region is revealed as evidenced on the La, Zr, O and Ge elemental profiles determined by STEM-EELS (Figure 5.7(b)). The Zr and O profiles increase just after the substrate and beyond few nm become constant with a Zr/O ratio ~ 0.5 . The La profile has a peak just above the interface, the intensity at the maximum being La/Zr ~ 0.1 and then continuously decreases. The La, Zr and O profiles are very similar in the as-grown and annealed state. Firstly, Ge is present above the interface with a non-negligible content in the region of the La peak. After RTA, Ge profile has a similar shape but spreads over a larger distance from the substrate. STEM-EELS profiles reveal a La and Ge rich region near the interface different from the following region of nearly constant composition. Hence, the as-grown and annealed films can be described by a two layers structure from the chemical point of view. As indicated when the Ge profiles go to zero, we can infer that a 2 nm thick IL is present in the as-grown state and a nearly 2.5 nm thick IL is present after RTA (dotted and plain lines respectively, Figure 5.7(b)). The chemical bondings at the interface were probed by XPS analyses of the Ge 2p line performed on 3 nm thick as-grown and annealed samples (Figure 5.7(c)) in normal photoemission geometry by using a standard Mg K_α (1253.6 eV) radiation source with a pass energy of 20 eV. Both the Ge 2p lines can be deconvoluted in two different contributions from the elemental Ge bonding of the substrate (Ge⁰) and Ge-O like bonding (Ge*). The mutual shift between the two components is 2.3 eV, which significantly deviates from the expected chemical shift due to GeO₂

thereby suggesting the formation of a germanate-like region before and after RTA [24]. The increased intensity of the Ge^0 contribution after annealing reflects a thermally induced reduction of the overall thickness. XRR analysis (not shown) performed on the same samples also revealed a reduction of total thickness and a corresponding 10% electronic density increase upon RTA related to a densification of the whole layer. The formation of a germanate IL, associated to the use of O_3 , might be helpful in keeping the D_{it} value relatively low.

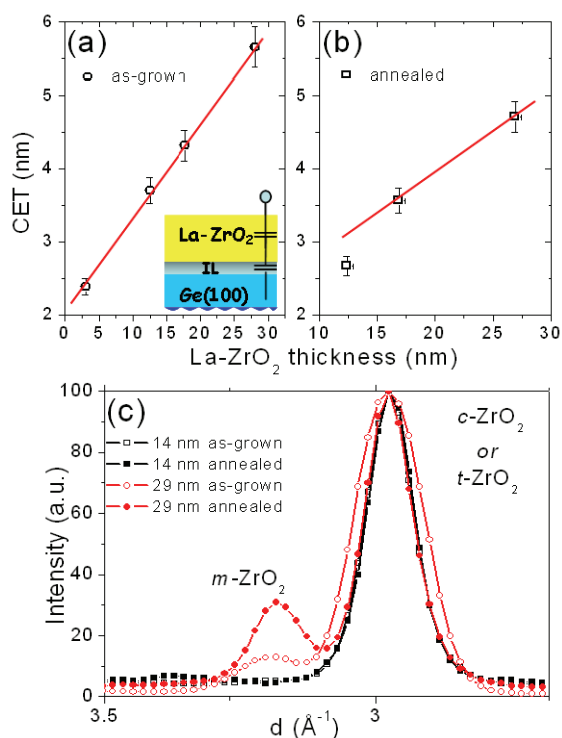


Figure 5.8: (a) CET vs La-ZrO₂ thickness plot for as-grown samples. MIS devices received no postmetallization annealing. Inset shows the two capacitors model (La-ZrO₂/IL/Ge). (b) CET vs La-ZrO₂ thickness plot for annealed samples. (c) SAED intensity profiles acquired on 29 and 14 nm thick as-grown and annealed samples.

Electrical results are discussed based on the previous detailed stack description. Figure 5.8(a) shows a linear dependence of the CET versus La-ZrO₂ physical thickness plot, leading to $k = 29 \pm 1$ for the as-grown films. This k value resembles the one expected for c - and is definitely higher than the one of monoclinic (m -) ZrO₂ (~ 20) [25,26]. An active role in determining the k of as-grown films might be played by the large ionic radius ($i_{\text{rad}} \sim 1.23$ Å) of La atoms, inserted into the ZrO₂ lattice, softening the ZrO₂ IR-active modes [23,27]. The intercept of the linear fit to the CET data confirms the presence of an IL between La-ZrO₂ and Ge(100) and clarifies the higher k values of La-ZrO₂ compared to the one of the stack. Considering a 2 nm thick IL, as revealed by STEM-EELS, a low IL k ($k_{\text{IL}} = 4$) is calculated. The use of this IL in a two capacitors model (inset of Figure 5.8(a)) results in a $k = 28 \pm 1$ for the as-grown La-ZrO₂. After annealing, CET versus La-ZrO₂ thickness plot (Figure 5.8(b)) can not be interpolated by a linear fit. This finding can be clarified by structural and chemical modifications within the films depending on their thickness as illustrated in Figure 5.8(c) and Figure 5.9. Figure 5.8(c) shows the SAED analyses performed on the thickest (29 nm) and the thinnest (14 nm) stacks before and after RTA. The presence of m -ZrO₂ phase is revealed in the thick (19 and 29 nm) as-grown samples and such m - fraction increases significantly upon annealing. Differently, the 14 nm thick film is free of m -ZrO₂. An estimation of the k , by means of linear fit, for the two thickest annealed stacks results in a $k = 34 \pm 1$ (Figure 5.8(b)); given a 2.5 nm thick IL revealed by STEM-EELS a $k_{\text{IL}} = 6.2$ is calculated from the fit intercept. This value is in agreement with the presence of a comparatively denser germanate compound at the interface or with k values proposed for germanates [24,28]. The use of these IL parameters in a two capacitors model for all the annealed films provides a $k = 32 \pm 1$ for the thick films (19 and 29 nm) whereas for the thinner annealed La-ZrO₂ the k is remarkably increased up

to $\sim 42 \pm 1$. Such result confirms that the 14 nm thick film must be considered structurally different. To assess modifications of the elemental composition within the film after RTA, ToF SIMS depth profiles were acquired in negative polarity on an ION-TOF IV instrument using Cs^+ ions at 1 keV for sputtering and Ga^+ ions at 25 keV for analysis. Upon RTA, LaO and ZrO_2 signals are not modified (Figure 5.9(a)) whereas Ge diffusion throughout the oxide is evidenced by the ^{70}Ge signal. This Ge diffusion towards the surface was not observed by STEM-EELS due to its sensitivity limit for Ge (3-5%). Ge can be inferred to diffuse up to the top of the La- ZrO_2 layer coming directly from the substrate; its diffusion strongly depends on film thickness as shown by the different ^{70}Ge profiles (Figure 5.9 (a-b and c)).

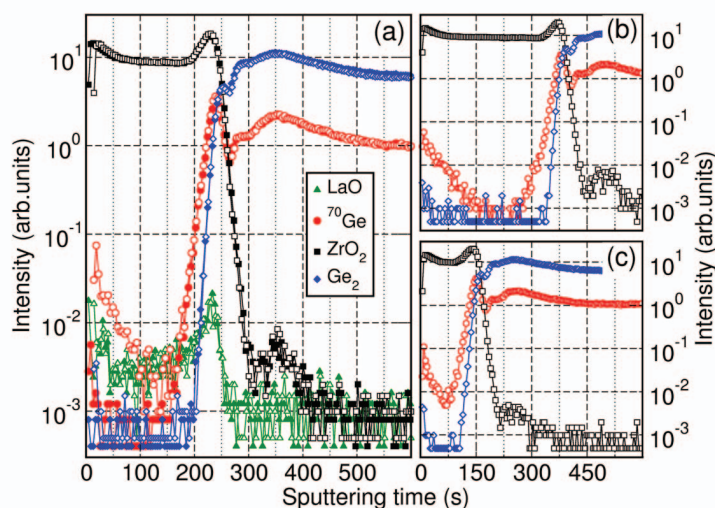


Figure 5.9: (a) ToF SIMS depth profiles for 19 nm thick, as-grown (closed symbols) and annealed (open symbols), La- ZrO_2 film. ToF SIMS depth profiles for 29 (b) and 14 (c) nm thick annealed La- ZrO_2 films.

Actually, the presence of a Ge-poor region is more pronounced in thicker films and therefore these dissimilar chemical profiles might be directly associated with the evidence of variable crystalline mixtures in different films. Hence, Ge diffusion is expected to be responsible for the absence of *m*- ZrO_2 phase in the 14 nm sample and thus for the increase of La- ZrO_2 *k* after RTA. Interdiffused Ge might be playing a role in stabilizing the *t*- ZrO_2 phase, as proposed in Ref. [11,16], since the *k* of the thicker samples also slightly increases after annealing despite the development of the *m*- phase. This can be corroborated by the fact that pronounced electrical differences are accompanied in the thinnest annealed sample by a remarkable Ge diffusion. To further support the role of Ge in the increase of the *k* it should be noted that, when ZrO_2 was deposited on a La_2O_3 passivating IL, only a *k* ~ 32 for ZrO_2 was measured [24]. Differently from Ref. [11,24,29], La- ZrO_2 has been directly deposited on bare Ge(100) without any intentional IL. The observed *k* enhancement is consistent with the prediction by Fischer *et al.* [16] that, upon introduction of Ge substitutional atoms, *t*- ZrO_2 can become energetically more favorable than *m*- or *c*- phases. Ge atoms, with a small i_{rad} (~ 0.53 Å), are readily incorporated in the thin La- ZrO_2 layer therein promoting the stabilization of *t*- ZrO_2 . Although the revealed Ge concentration in La- ZrO_2 is lower than the one theoretically considered, this value appears sufficient for stabilizing *t*- ZrO_2 [30]. In summary, we showed that the combination of a direct O_3 -based ALD of La- ZrO_2 and a postgrowth thermal treatment can lead to the obtainment of a high *k* > 40 . It is proved that Ge atoms are supplied by the substrate and penetrate into the oxide upon annealing. The observed large *k* value after RTA is consistent with Ge-induced stabilization of the *t*- ZrO_2 phase in thin film. Ge diffusion occurs without affecting the interfacial details qualified by a germanate-like region and an acceptably low D_{it} value.

Er-doped HfO₂ on Ge(100)

Er-doped HfO₂ films, with a variable Er content in the 1-16 % range, were grown by ALD on native oxide free Ge(100) using the same recipe employed on H-terminated Si(100) (see Chapter 4). The deposition temperature was fixed at 300 °C, sample thickness was determined by means of XRR, SE and HRTEM. Films were also subjected to a post-growth RTA in N₂ atmosphere for 60 s at 400 °C. In Table 5.2 the list of films grown on Ge(100) with different Er content is reported. TXRF analysis was performed on all films and showed an excellent agreement in terms of Er content with the analysis performed on the set of films grown on H-terminated Si(100).

Table 5.2: SE and TXRF analysis performed on the Er-doped HfO₂ films grown on native oxide free Ge(100).

| Er : Hf ratio | SE thickness as-grown (nm) | Er % at ± 2% | Hf % at ± 2% |
|------------------|-------------------------------|-----------------|-----------------|
| HfO ₂ | 13.0 | 0 | 100 |
| 1 : 4 (ErHfO) | 8.4 | 16.0 | 84.0 |
| 1 : 8 | 12.1 | 13.1 | 86.9 |
| 1 : 10 | 12.0 | 10.8 | 89.2 |
| 1 : 12 | 13.3 | 9.7 | 90.3 |
| 1 : 15 | 13.2 | 4.3 | 95.7 |
| 1 : 30 | 13.9 | 1.5 | 98.5 |

GIXRD spectra acquired on as-grown and annealed films with different Er contents are reported in Figure 5.10.

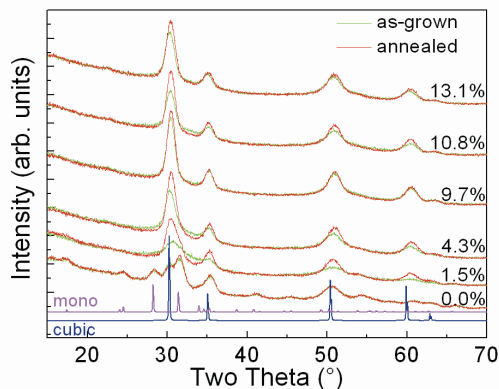


Figure 5.10: GIXRD patterns of as-grown and 400 °C annealed Er-HfO₂ films grown on Ge.

All the analyzed films are already crystallized in the as-grown state (Figure 5.10). The post-deposition annealing induces an increase of the crystallized fraction. The pure HfO₂ film grown on Ge(100) presents a monoclinic crystallographic structure, with a small contribution of the cubic (or tetragonal or orthorhombic) phase being also revealed. The film grown with an Er percentage of ~1.5% presents a more complicated crystallographic structure composed by a mixture of monoclinic and cubic phases. Differently, for Er percentages within 4-16%, crystallization takes place only in the cubic phase of HfO₂. A more detailed structural, chemical and electrical characterization is performed on the films grown incorporating the highest Er content (i.e. 16% Er) and found crystallized in the cubic phase of HfO₂. HRTEM cross sections of the as-grown and annealed ErHfO films are shown in Figure 5.11. It is worth noticing that there is no evidence of a structural IL between the Er-based oxide and the Ge(100). A direct contact between the nanocrystals and the Ge substrate surface can be observed on the high

resolution images. The thicknesses of the films are around 12 nm and the crystallization state looks similar in the as-deposited and annealed films.

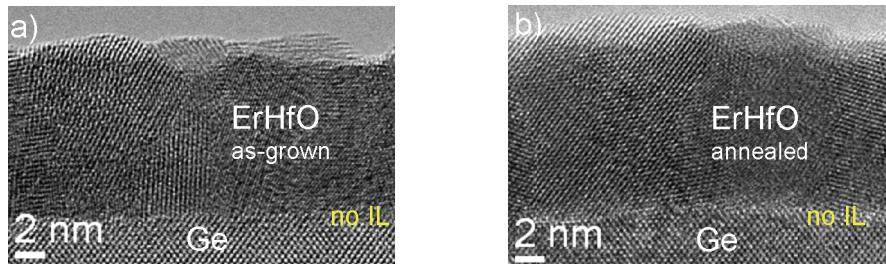


Figure 5.11: HRTEM cross sections of a 10 nm thick (a) as-grown and (b) annealed ErHfO film.

ToF SIMS depth chemical profiles (Figure 5.12) were acquired on the as-grown and the annealed ~10 nm thick ErHfO films. In order to evaluate the effect of the Er incorporation, ToF SIMS was also performed on pure HfO₂.

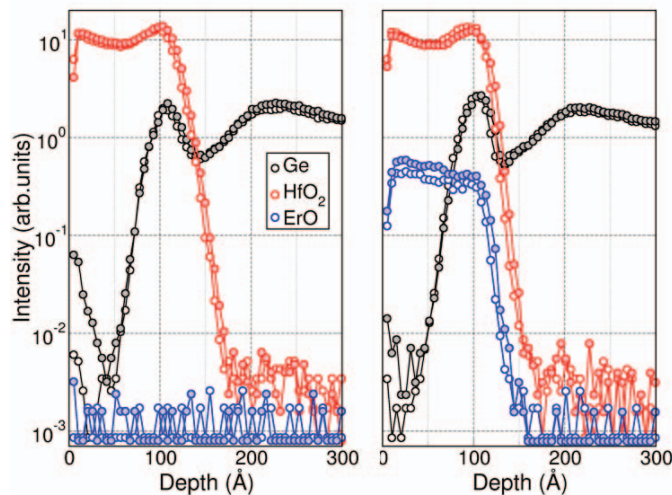


Figure 5.12: ToF SIMS depth profiles acquired for as-grown (open symbols) and annealed (closed symbols) HfO₂ film (left panel) and ErHfO film (right panel).

It is not possible to clearly define an IL between the HfO₂ (or ErHfO) film and the Ge(100). However, after annealing the Ge signal appears slightly modified, suggesting Ge diffusion both into the HfO₂ and ErHfO layer, with a higher amount of Ge diffusing through HfO₂ than through ErHfO. Electrical characterization was performed on MOS capacitors fabricated using a set of ErHfO films with different thickness in the 5-30 nm range.

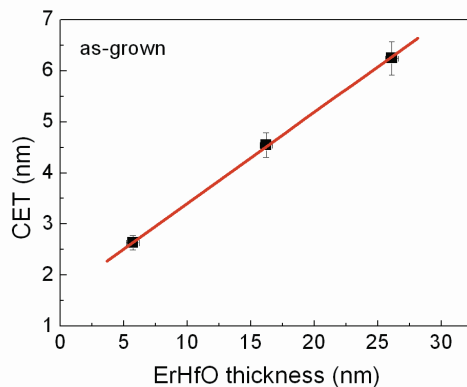


Figure 5.13: CET vs ErHfO thickness, as-grown films.

From the plot of the CET vs ErHfO thickness, deduced with combined XRR and SE measurements, a k value of 22 ± 1 can be extracted for as-grown case (Figure 5.13). Interestingly, annealing at $400\text{ }^\circ\text{C}$ does not affect the ErHfO dielectric constant; it remains $k = 21 \pm 1$, unchanged within the error bars (Figure 5.14). It is worth underlining that the same oxide (i.e. ErHfO, Er $\sim 16\%$), grown with the same ALD recipe, presents remarkably different dielectric constants as a function of the substrate. In fact, the latter k values calculated for ErHfO deposited onto Ge substrates are markedly lower than those calculated for the same oxide grown on H-terminated Si(100) (see Chapter 4, $k \sim 27$ and ~ 33 in the as-grown and annealed state, respectively).

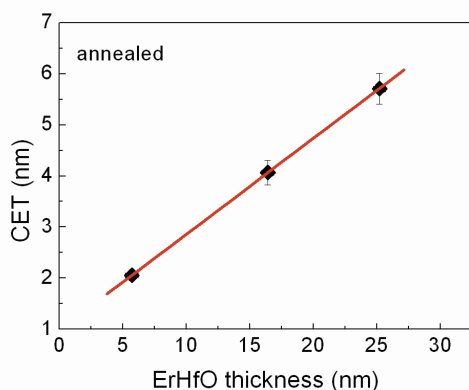


Figure 5.14: CET vs ErHfO thickness, films annealed at $400\text{ }^\circ\text{C}$ in N_2 .

This anomalous finding on Ge substrates may be attributed to the Ge atoms diffusion within the films which is found to occur either during ALD growth or during the post-deposition RTA. Such a Ge interdiffusion throughout HfO_2 neither enhances the k value of the ErHfO, nor stabilizes any high- k HfO_2 metastable phases (e.g. tetragonal HfO_2) although the crystallized fraction is slightly increased, as found by XRD analysis. Thus, differently from what reported for Zr-based systems [5,23,29,41], the doping of the ErHfO oxide by means of Ge atoms diffusion from the substrate does not improve the dielectric properties of the material. It is theoretically predicted that for Ge content $> 10\text{-}12\%$ the HfO_2 stable crystallographic phase is expected to be the cubic one. In this case, a k value around ~ 20 is predicted for the HfGe-based system [31]. The crystallization of cubic Ge-doped ErHfO might therefore induce a k value lower than the one of ErHfO, in good agreement with the different k values we obtained on Si(100) and on Ge(100).

Atomic Layer Deposition of high-*k* oxides on III-V substrates [32,33]

In the present section the research work carried out on La-doped ZrO₂ (La-ZrO₂), grown by ALD on properly engineered III-V interfaces is presented. La-ZrO₂ thin films were grown by O₃-based ALD on III-V (i.e. GaAs, In_{0.15}Ga_{0.85}As) substrates in two different configurations; e.g. through direct deposition onto NH₄(OH) treated surfaces and after intercalation of a Ge interfacial passivating layer (IPL). Indeed, capping III-V compound surfaces with Ge ultra thin layer might be a viable pathway to passivate the electrically active interface traps of III-V materials. The structural and compositional features of the La-ZrO₂/GaAs and La-ZrO₂/Ge/GaAs interfaces were thoroughly investigated by XPS. A general overview of the XPS compositional analysis accounting for the Ga 3*d* and As 3*d* core-level photoemission lines is reported in Figure 5.15(a) and (b) for 3 nm thick La-ZrO₂ films on GaAs without and with Ge IPL, respectively.

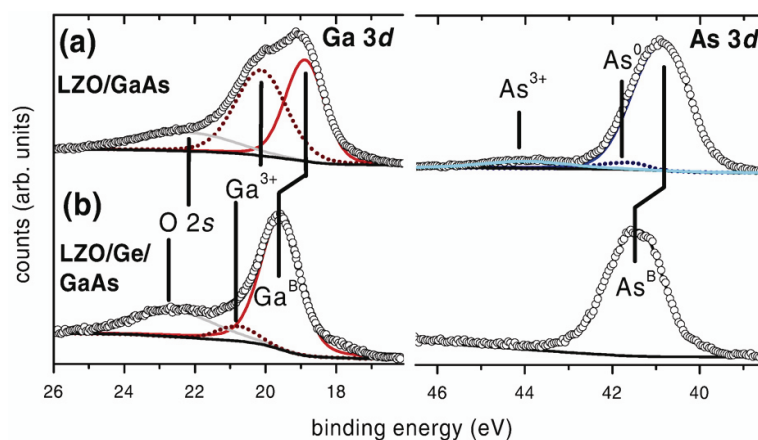


Figure 5.15: Ga 3*d* and As 3*d* XPS lines recorded for La-ZrO₂/GaAs (a) and La-ZrO₂/Ge/GaAs (b). Ga^B and As^B denote the bulk contributions, the displacement between the bulk peaks in case (a) and (b) is marked. Ga³⁺ and As³⁺ components reflect the presence of interfacial Ga₂O₃ and As₂O₃, respectively. As⁰ indicates interfacial elemental As bonding.

The binding energy (BE) of the spectra was referred to the pre-calibrated position of adventitious carbon in the C 1*s* line (BE=284.8 eV). Direct ALD of La-ZrO₂ onto GaAs is studied in Figure 5.15(a). Here, the Ga 3*d* line exhibits an interplay of three components, from GaAs bulk (Ga^B at BE=18.7 eV), from Ga₂O₃ interfacial bonding (Ga³⁺ at BE = 19.9 eV) and from the O 2*s* line coming due to the overlying oxide (BE = 22.2 eV). The As 3*d* line deconvolution involves three different contributions which can be assigned to As from GaAs bulk (BE = 40.7 eV), to As₂O₃ (and no As₂O₅) species (BE = 43.8 eV) and to elemental As bonding (BE = 41.6 eV). Opposed to the significant interface concentration of semiconductor–oxygen and As homopolar bonding observed after direct ALD processing, the scenario radically changes when Ge IPL is sandwiched between the oxide and GaAs. The related XPS analysis is illustrated in Figure 5.15 (b). As a result, the formation of As–O bonding can be here completely ruled out from the interface composition as no associated component is observed in the respective As 3*d* lines, whereas a remarkably lower Ga–O related component can be deduced from the Ga 3*d* line deconvolution. It should be noted that the position of the Ga 3*d* and As 3*d* bulk peaks are mutually displaced by an amount of 0.6 eV which reflects the different alignment of the electronic bands in the two different interface configurations.

The intercalation of a Ge IPL is shown to suppress the concentration of interface Ga-O, As-O and elemental As bonding which were significantly detected in case of the direct oxide deposition on GaAs. The interface configuration deriving from the Ge IPL insertion has been studied by means of SE and XPS analyses.

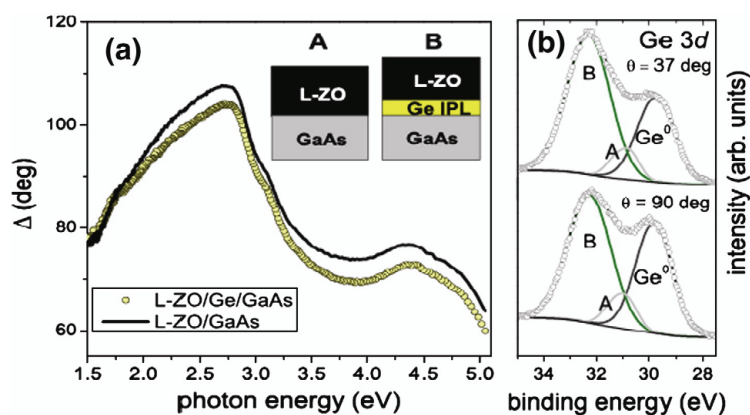


Figure 5.16: (a) SE scans registered for L-ZO/GaAs (line) and L-ZO/Ge/GaAs (circles). Inset: sketches of the two multilayer models used to interpolate the SE data in the two different interface configurations, L-ZO/GaAs and L-ZO/Ge/GaAs. (b) Ge 3d XPS lines taken at two take-off angles, $\theta=37^\circ$ (up) and 90° (down). See the text for details of the spectra deconvolution.

The electrical quality of the GaAs-based heterostructure should be dictated by the chemical details of the interface that Ge IPL forms with the overlying La-ZrO₂ film. The information from SE and XPS data were mutually combined in order to elucidate this aspect as reported in Figure 5.16. From the SE measurements of the NH₄(OH) treated GaAs(100), taken immediately before the oxide deposition, the pseudo-dielectric function ($\langle \epsilon \rangle = \langle \epsilon_1 \rangle + i \langle \epsilon_2 \rangle$) of the substrate [34] can be extracted by means of a Point-by-Point interpolation [35] of the spectra. This enabled us to model the semiconductor substrate as a nearly oxide free. Therefore the calculated $\langle \epsilon \rangle$ results in a qualitatively good agreement with the tabulated values expected for GaAs(100) [36] and is then used in all the models to represent the substrate. La-ZrO₂ dielectric function was estimated using a Cauchy dispersion relation [37] (oxide is transparent in the 1.2-5.0 eV range) on thicker samples and was then applied to model the thin layers constituting the samples; Ge dielectric function was assumed from tabulated values. The only free parameters used in the two SE fits were La-ZrO₂ thickness (t_{ox}) and Ge layer thickness (t_{ge}). In Figure 5.16(a) is reported a close-up of the experimental Δ spectra acquired after ALD deposition on GaAs(100) and on the Ge/GaAs(100) stack. The pronounced difference between the two curves can be uniquely attributed to the presence of the ultra-thin Ge IPL underneath the oxide. Such a difference can be rationalized in terms of the multi-layers physical model fit to the SE data. In detail, a two layer model (see scheme A in the inset of Figure 5.16) was used to represent La-ZrO₂/GaAs therein resulting in an oxide thickness of t_{ox} of 8.2 ± 0.2 nm. On the contrary, a three layer model based fitting was necessary to account for the Ge-passivated sample therein indicating the permanence of purely Ge IPL after oxide deposition. Using a three layers model (see scheme B the inset of Figure 5.16) results in $t_{\text{ox}} = 7.4 \pm 0.2$ nm and $t_{\text{ge}} \sim 0.6$. This picture can be corroborated by the complementary XPS analysis in Figure 5.16(b) where the Ge 3d line is studied as a function of the sampling depth, i.e. at a low take-off angle measurement ($\theta = 37^\circ$) and under normal photoemission ($\theta = 90^\circ$) to probe near-to-surface and deeper regions of the sample, respectively. Both Ge 3d lines exhibit three components, one at lower BE due to elemental Ge -Ge bonding of the Ge IPL and two (A and B in Figure 5.16(b)) at higher BE ($\text{BE}_A=30.7$ eV and $\text{BE}_B=31.9$ eV) being consistent with oxidized Ge bonding. The evidence of an elemental Ge bonding signal evidences the presence of a pure Ge/oxidized Ge interfacial structure. The observed Ge-O bonding signal can be located at the Ge/ La-ZrO₂ interface as the related XPS signal increases for decreasing take-off angles, i.e. with a lower sampling depth. The physical nature of the Ge-O component is consistent with the formation of a Ge-O bonding region throughout the La-ZrO₂ top stack. A more careful deconvolution of the Ge 3d line suggests the interplay of two Ge-O components (A and B in Fig. 2(b)) with different valence states. The A and B components can be

assigned and to minor GeO_x concentration and [38,39] to germanate like region [40], respectively. As the relative A/B intensity ratio slightly increases with increasing θ (from 0.14 at $\theta=37^\circ$ to 0.17 at $\theta=90^\circ$), the GeO_x species presumably places atop the pure Ge layer whereas germanate is located in between the GeO_x and the La-ZrO₂. Such a picture is also supported by the observed position of the relevant Zr 3d line at BE = 182.6 eV (not shown) being consistent with the Ge substitutional bonding inside ZrO₂ as described in Ref. [41].

In summary, given the potential application of Ge as passivating material for III–V compound surfaces, Ge ultra-thin films were grown on differently prepared GaAs(001) substrates and the relevant interface bonding was elucidated by XPS. Intercalation of Ge IPL between $\text{NH}_4(\text{OH})$ treated GaAs and La-doped ZrO₂ films grown by O₃-based ALD confers a remarkably improved chemical quality to the interface with GaAs compared to the case of the direct oxide deposition. The Ge IPL leads to an efficient removal of potentially defective Ga₂O₃, As₂O₃ and As elemental bonding from the interface. The use of O₃ as oxidizing agent is concomitantly intended to gain superior dielectric properties of the oxide [23] and to pursue the electrical passivation of the Ge IPL surface [21] providing an ALD suited approach to fabrication of Ge IPL/GaAs-based MOS capacitors. Furthermore, an improved electrical quality of the Ge-passivated interfaces due to the removal of Ga³⁺ bonding defects close to the conduction band-edge region was also demonstrated by conductance measurements at different temperatures [32].

References

- [1] MRS Bulletin, “*Ultimate scaling of CMOS logic devices with Ge and III-V materials*”, **34** (2009).
- [2] L. Lamagna *et al.*, “*O₃-based atomic layer deposition of hexagonal La₂O₃ on Si and Ge*”, in preparation (2009).
- [3] Inorganic Crystal Structure Database, Fachinformationszentrum, Karlsruhe, 2009, file n°: 31584.
- [4] Inorganic Crystal Structure Database, Fachinformationszentrum, Karlsruhe, 2009, file n°: 24693
- [5] L. Lamagna, C. Wiemer, S. Baldovino, A. Molle, M. Perego, S. Schamm, P. E. Coulon, and M. Fanciulli, *Appl. Phys. Lett.* **95**, 122902 (2009).
- [6] Y. Kamata, Y. Kamimuta, T. Ino, R. Iijima, M. Koyama, and A. Nishiyama, *Jap. J. Appl. Phys.* **45**, 5651 (2006).
- [7] Y. Kamata, Y. Kamimuta, T. Ino, and A. Nishiyama, *Jap. J. Appl. Phys.* **44**, 2323 (2005).
- [8] J. Oh, P. Majhi, C. Y. Kang, J.-W. Yang, H.-H. Tseng, and R. Jammy, *Appl. Phys. Lett.* **90**, 202102 (2007).
- [9] A. Delabie, F. Bellenger, M. Houssa, T. Conard, S. Van Elshocht, M. Caymax, M. Heyns, and M. Meuris, *Appl. Phys. Lett.* **91**, 082904 (2007).
- [10] H. Kim, C. O. Chui, K. C. Saraswat, and P. C. McIntyre, *Appl. Phys. Lett.* **83**, 2647 (2003).
- [11] P. Tsipas, S. N. Volkos, A. Sotiropoulos, S. F. Galata, G. Mavrou, D. Tsoutsou, Y. Panayiotatos, A. Dimoulas, C. Marchiori, and J. Fompeyrine, *Appl. Phys. Lett.* **93**, 082904 (2008).
- [12] M. Caymax, M. Houssa, G. Pourtois, F. Bellenger, K. Martens, A. Delabie, S. Van Elshocht, *Appl. Surf. Sci.* **254**, 6094 (2008).
- [13] S. Baldovino, A. Molle, and M. Fanciulli, *Appl. Phys. Lett.* **93**, 242105 (2008).
- [14] A. Molle, Md N. K. Bhuiyan, G. Tallarida, and M. Fanciulli, *Appl. Phys. Lett.* **89**, 082904 (2006).
- [15] H. J. Na, J. C. Lee, D. Heh, P. Sivasubramani, P. D. Kirsch, J. W. Oh, P. Majhi, S. Rivillon, Y. J. Chabal, B. H. Lee, and R. Choi, *Appl. Phys. Lett.* **93**, 192115 (2008).
- [16] D. Fischer and A. Kersch, *Appl. Phys. Lett.* **92**, 012908 (2008).
- [17] C. K. Lee, E. Cho, H. S. Lee, C. S. Hwang, and S. Han, *Phys. Rev. B* **78**, 012102 (2008).
- [18] G. Mavrou, S. Galata, P. Tsipas, A. Sotiropoulos, Y. Panayiotatos, A. Dimoulas, E. K. Evangelou, J. W. Seo, and C. Dieker, *J. Appl. Phys.* **103**, 014506 (2008).
- [19] M. Houssa, G. Pourtois, M. Caymax, M. Meuris, and M. M. Heyns, *Appl. Phys. Lett.* **92**, 242101 (2008).
- [20] D. Kuzum, T. Krishnamohan, A. J. Pethe, A. K. Okyay, Y. Oshima, Y. Sun, J. P. McVittie, P. A. Pianetta, P. C. McIntyre, and K. C. Saraswat, *IEEE Electron Device Lett.* **29**, (4) 328 (2008).
- [21] S. Spiga, C. Wiemer, G. Tallarida, G. Scarel, S. Ferrari, G. Seguini, and M. Fanciulli, *Appl. Phys. Lett.* **87**, 112904 (2005).
- [22] W. A. Hill and C. C. Coleman, *Solid-State Electron.* **23**, 987 (1980).
- [23] D. Tsoutsou, L. Lamagna, S. N. Volkos, A. Molle, S. Baldovino, and M. Fanciulli, S. Schamm and P. E. Coulon, *Appl. Phys. Lett.* **94**, 053504 (2009).
- [24] G. Mavrou, P. Tsipas, A. Sotiropoulos, S. F. Galata, Y. Panayiotatos, A. Dimoulas, C. Marchiori, and J. Fompeyrine, *Appl. Phys. Lett.* **93**, 212904 (2008).
- [25] X. Zhao and D. Vanderbilt, *Phys. Rev. Lett. B* **65**, 075105 (2002).
- [26] O. Ohtaka, D. Andrault, P. Bouvier, E. Schultz, and M. Mezouar, *J. Appl. Cryst.* **38**, 727 (2005).
- [27] S. A. Shevlin, A. Curioni, and W. Andreoni, *Phys. Rev. Lett.* **94**, 146401 (2005).
- [28] J. Song, K. Kakushima, P. Ahmet, K. Tsutsui, N. Sugii, T. Hattori, and H. Iwai, *Microelectron. Eng.* **84**, 2336 (2007).
- [29] D. Tsoutsou, G. Apostolopoulos, S. Galata, P. Tsipas, A. Sotiropoulos, G. Mavrou, Y. Panayiotatos, A. Dimoulas, *Microelectron. Eng.* **86**, 1626 (2009).
- [30] D. Fischer and A. Kersch, *J. Appl. Phys.* **104**, 084104 (2008).
- [31] A. Debernardi, *Mat. Sci. Eng.* in press (2009).
- [32] A. Molle, G. Brammertz, L. Lamagna, M. Fanciulli, M. Meuris, and S. Spiga, *Appl. Phys. Lett.* **95**, 023507 (2009).
- [33] A. Molle, L. Lamagna, S. Spiga, G. Brammertz, M. Meuris, and M. Fanciulli, *Thin Solid Films* in press (2009).
- [34] H. G. Tompkins and E. A. Irene, “*Handbook of Ellipsometry*”, William Andrew Publishing and Springer (2005).
- [35] E. D. Palik, “*Handbook of Optical Constants of Solids*”, Academic Press, (1985).
- [36] S. Zollner, D. Zarr, *Compound Semiconductors*, 2000 IEEE Int. Symp, 13 (2000).

-
- [37] H. G. Tompkins, “*A user's guide to Ellipsometry*”, Dover Publications, Inc., Mineola, New York (1993).
- [38] A. Molle, S. Spiga, M. Fanciulli, J. Chem. Phys. **129**, 011104 (2008).
- [39] A. Molle, M. N. K. Bhuiyan, G. Tallarida, M. Fanciulli, Appl. Phys. Lett. **89**, 083504 (2006).
- [40] O. Renault, L. Fourdrinier, E. Martinez, L. Clavelier, C. Leroyer, N. Barrett, C. Crotti, Appl. Phys. Lett. **90**, 052112 (2007).
- [41] P. Tsipas, S. N. Volkos, A. Sotiropoulos, S. F. Galata, G. Mavrou, D. Tsoutsou, Y. Panayiotatos, A. Dimoulas, C. Marchiori, J. Fompeyrine, Appl. Phys. Lett. **93**, 082904 (2008).

Chapter 6

In situ Spectroscopic Ellipsometry*

* Results to be published as:

L. Lamagna *et al.*, “*In situ* spectroscopic ellipsometry during atomic layer deposition of rare earth-based high-*k* dielectrics”, in preparation (2009).

***In situ* SE of thin films grown by ALD**

In this chapter, the application of *in situ* SE as a diagnostic to investigate ALD of binary and ternary oxides either on Si(100) or on Ge(100) is discussed. Recently, *in situ* SE has been definitely proved to be a powerful tool to perform online process monitoring and control of the deposition process even at the atomic level [1]. During ALD, having the possibility to control the film thickness evolution and thus the growth rate per cycle is an outstanding benefit in terms of process control. Moreover, process parameters such as the saturation pulse condition and the ALD window can be easily investigated by *in situ* SE measurements thus drastically reducing the number of required experiments. *In situ* SE can also provide an important contribution concerning the study of the very early stages of the growth. Indeed, SE measurements performed during the first 50 ALD cycles might reveal the actual formation of an IL between the substrate and the material which is being deposited on top. On the other hand, probing the early stages of the deposition provides information on the so-called “nucleation delay” which has been demonstrated for several ALD processes on different substrates. An important and innovative contribution on the *in situ* SE studies during ALD, which is present nowadays in literature, comes from the research activity carried out at the Department of Applied Physics of the Eindhoven University of Technology. A PhD thesis and a review paper on this specific topic have been recently published showing the versatility and the capability of *in situ* SE employed during thermal and plasma assisted ALD [1,2]. Depending on the total film thickness, different approaches were followed during the optical modeling of the films discussed in this work. Indeed, although the measurement capability of SE is actually adequate to detect thicknesses down to fractions of monolayers; when dealing with extremely thin films the modeling procedure has to be carefully considered. Often, only Δ varies significantly during the growth of extremely thin films and normally only thickness information is obtained from this kind of SE measurements [3,4]. Therefore, due to the strong correlation in the fit between thickness and optical constants values, the former are measured while the latter have to be reasonably assumed in the model. It is worth noticing that, in order to eliminate the spot-to-spot possible variation of Ψ and Δ , the *in situ* SE approach turns out to be the most reliable to probe extremely thin layers. In this work we arbitrarily consider as ultra thin films all the layers which present a total thickness below 5 nm.

In the following part of the chapter *in situ* SE results obtained for rare earth-based oxides grown by ALD are presented. In particular, two families of oxides were investigated:

- ❖ La- and Zr-based oxides (e.g. La_2O_3 , ZrO_2 , LaZrO and La-doped ZrO_2)
- ❖ Er- and Hf-based oxides (e.g. Er_2O_3 , HfO_2 , ErHfO and Er-doped HfO_2)

Some relevant examples concerning the applications of *in situ* SE during ALD of these materials are presented. The attention is firstly focused on the important contribution provided by the integration of SE as *in situ* diagnostic to monitor ALD processes. Afterwards, *in situ* SE is used to investigate specific details of the growth such as the IL formation and the interface reactivity at the oxide/semiconductor substrate interface.

Optical modeling

All the *ex situ* and *in situ* SE measurements were all carried out employing an M2000 rotating compensator ellipsometer (J. A. Woollam Co., Inc.) [5]. The acquired SE experimental optical data (Ψ and Δ curves) were simulated using a model based on the minimization of the Mean Square Error (MSE) routine [6]. The former is calculated from the difference in the experimental and model generated data and weighted with respect to the experimental standard deviations at each wavelength. The modeling of the experimental data allows extracting parameters such as film thickness and optical constant n and k (or ϵ_1 and ϵ_2) values [3]. The lamp which is operating on this ellipsometer generates light with photon energy in the 1-5 eV range. All the oxides discussed in this work can be considered transparent in this energy range due to the fact that all their optical gaps are placed at energy values well above 5 eV. Therefore, being the absorption of the light negligible during SE measurements, the absorption term has been always considered equal to zero ($k = \epsilon_2 = 0$) over the whole employed photon energy range. For the optical modeling of the layers, a Cauchy relationship was employed to describe the dispersion of the refractive index n [3]:

$$n = A_n + \frac{B_n}{\lambda^2} + \frac{C_n}{\lambda^4}$$

in which A_n , B_n and C_n are the Cauchy fit parameters.

Modeling was commonly performed using a two layers structure composed by:

- substrate: Si or Ge (at room temperature or at the actual deposition temperature)
- film

Regarding the optical modeling and model structure employed for stacks with thicknesses below 5 nm, a further discussion is dedicated in the last part of the chapter. In those cases an actual IL with different optical properties might be eventually probed and thus taken into account; provided that its optical constants are carefully assumed on the basis of an additional characterization. Prior to the modeling of the oxides grown using ALD, a parameterization of the Si and Ge dielectric functions has been performed taking into account the temperature effect on the optical properties of the semiconductor substrates. While for the case of Si the shape of the dielectric constants as a function of temperature is already known in literature and in standard SE commercial software [7,8], for Ge we have specifically extracted such dependence from *in situ* SE measurements performed at different temperatures in our ALD-SE system. The optical constants n and k (or ϵ_1 and ϵ_2) of Si and Ge substrates as a function of temperature were indeed modeled and refined on the basis of both literature reference values [9] and experimental measurements carried out at high temperature. Ψ and Δ spectra acquired at 80, 100, 200 and 300 °C allowed creating a temperature dependent model for the n and k of Si and Ge. In both cases, the same wafer was characterized under similar conditions and the only changing parameter was indeed the substrate temperature. More specifically, measurements were carried out directly on H-terminated Si(100) and native oxide free Ge(100) in order to obtain the actual “pseudo” optical constants of the substrates prior to begin the ALD growth. A proper “windows correction” factor was included in the ellipsometric software in order to take into account strain-induced birefringence of windows that can corrupt the polarization state of the measurement beam, and thereby the accuracy of the ellipsometric measurement.

The dispersion of the refractive index n of the various oxides was either calculated case by case from an ellipsometric fit or assumed on the basis of *ex situ* SE measurements performed on relatively thick (~30 nm) films. Moreover, film thickness obtained using SE was often checked and verified by means of XRR measurements performed on the same sample. A very good agreement between the results obtained using the two different characterization techniques was repetitively found regardless of the material considered. The dispersions of the refractive index for Er_2O_3 , HfO_2 and ErHfO , grown by ALD, are reported in Figure 6.1.

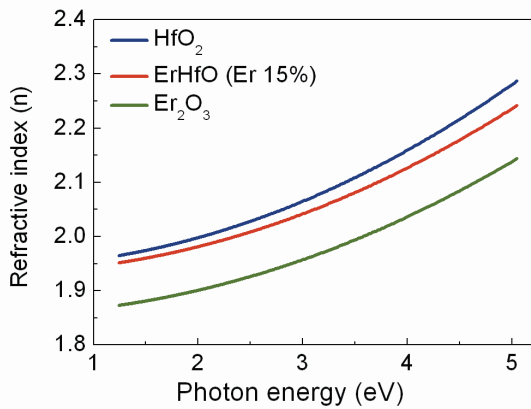
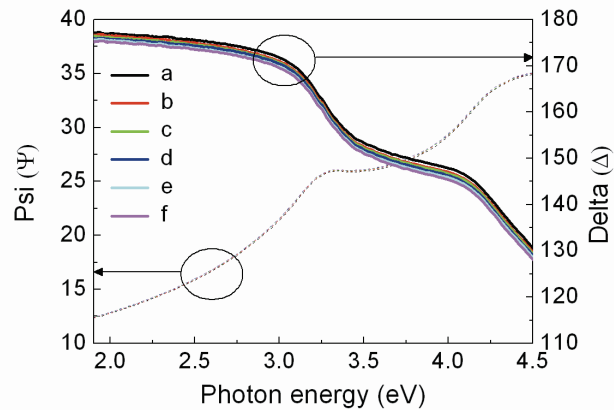


Figure 6.1: Dispersion of the refractive index (n) of HfO_2 , Er_2O_3 and ternary ErHfO (Er ~15%).

***In situ* SE monitoring in an ALD-SE experimental setup**

Using our ALD-SE experimental setup (see Chapter 2), *in situ* SE has been confirmed as an extremely sensitive technique even capable to detect changes in film thickness of fractions of monolayers. Figure 6.2 shows the Ψ and Δ curves obtained during ALD of a ternary LaZrO (La ~25%) film. In particular, Ψ and Δ spectra, acquired *in situ* during the first ternary ALD cycle of the whole deposition, are shown in Figure 6.2. Each ternary cycle consists of four ZrO_2 ALD cycles (curves b-e), followed by a single La_2O_3 cycle (curve f). Curve (a) represents the data acquired on the H-terminated $\text{Si}(100)$ at 300°C .

Figure 6.2: Ψ and Δ spectra acquired during the first ternary ALD cycles. (a) H-terminated $\text{Si}(100)$ at 300°C , (b-e) ZrO_2 ALD cycles, (f) La_2O_3 ALD cycle.



The different deposition steps of the first ALD cycle can clearly be distinguished and recognized in Figure 6.3, where a close-up of the Δ spectra is plotted.

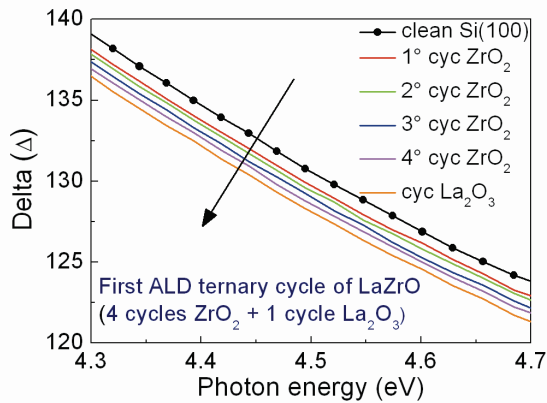


Figure 6.3: Close-up of the Δ spectra in the 4.3 – 4.7 eV energy region.

***In situ* SE for ALD process optimization**

In ALD there are several process parameters that can be easily investigated and thus optimized employing *in situ* SE. The first mandatory condition that has to be verified, when developing an ALD process, is the self-limiting behavior of the surface chemistry during the ALD reactions (see Chapter 2). This condition is commonly verified by means of the so-called “saturation curves” which are usually obtained by performing several experiments that are characterized by a different precursor pulse length, while all the other deposition parameters are kept constant. *In situ* SE measurements allow to measure film thickness at any stage of the growth. This means that after the deposition of few nm performed in a certain pulse condition, it is possible to increase the pulse length in order to check the self-limiting behavior of the reactions. Hence, it is possible to tune the precursor pulse length and investigate the effects related to the use of different saturation conditions during a single ALD run. In Figure 6.4 the excellent agreement between the growth per cycle of HfO₂ (HfD-04 and O₃ at 300 °C) measured using *in situ* SE, and the one calculated using separate ALD depositions is shown as a function of the HfD-04 precursor pulse length.

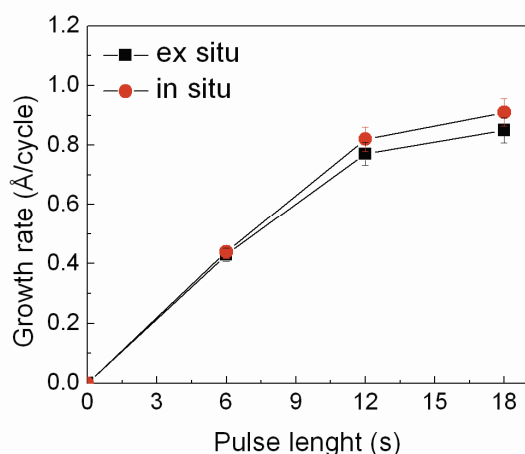


Figure 6.4: Growth rate vs HfD-04 pulse length; saturation curve for the HfD-04 and O₃ ALD process.

An alternative way to evaluate the self-limiting behavior of the ALD process is to plot the evolution of film thickness vs the number of ALD cycles. However, instead of constructing a single curve which refers to an established combination of ALD parameters, the precursor pulse length can be periodically increased after a certain number of cycles (i.e. ~100). Figure 6.5 shows the plot of film thickness vs the number of ALD cycles obtained by the *in situ* SE monitoring of La₂O₃ ALD. La(ⁱPrCp)₃ pulse length was increased (from 1 to 20 s) until the growth rate appeared to remain stable regardless of the La source pulse length.

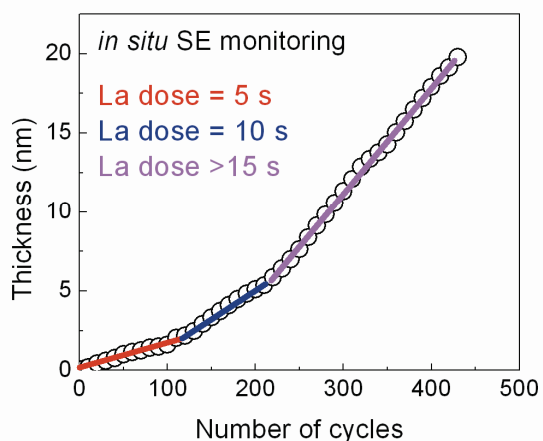


Figure 6.5: ALD of La₂O₃, *in situ* SE monitoring of the growth rate as a function of different La precursor pulse lengths.

In addition to the effect of the precursor pulse length (both metal and oxygen source), the effect of the variation of the deposition temperature on the growth rate can be also easily investigated by means of *in situ* SE measurements. The ALD reaction temperature can be indeed increased after the deposition of a certain film thickness and the related variation of the growth rate can be once again evaluated by looking at the film thickness *vs* the number of ALD cycles. Furthermore, the linear relationship between film thickness and the number of ALD cycles can be intrinsically evaluated during this kind of experiments. Indeed, unstable growths conditions such as undesired CVD side-reactions are immediately revealed when performing an accurate film thickness monitoring. Equally important is the outstanding possibility, provided by the *in situ* diagnostic, to identify something that is unexpectedly taking place during the growth and which is thus affecting the film deposition. Two common examples can be the cases when the metal precursor finishes during an ALD run or when the precursor's lines become blocked. In both cases, by means of *in situ* SE, the aforementioned issues can be immediately revealed through a simple thickness monitoring procedure.

Substrate effect: study of the Si(100) and Ge(100) cases

Most of the oxides investigated in the framework of this thesis were grown either on H-terminated Si(100) or on native oxide free Ge(100). The different starting conditions offered by the two semiconductor substrates, in terms of reactivity and density of surface chemical groups, were reasonably expected to affect the initial stages of the ALD growth and therefore the film nucleation behavior. *In situ* SE experiments were performed during ALD of ErHfO films (Er content ~16 %) as an example to clarify the substrate influence on the beginning of the oxide deposition. Especially, *in situ* SE provided useful information on the interface details of the two different stacks. These results were proved as affordable through the direct comparison of such analysis with complementary information obtained using *ex situ* characterization techniques such as XRR, HRTEM and STEM-EELS. In particular, a direct comparison between SE and XRR analyses is thoroughly discussed.

Film thickness nucleation behavior

In Figure 6.6 film thickness as a function of number of ALD cycles is shown for ErHfO deposition on H-terminated Si(100) and native oxide free Ge(100). Consequently to this analysis, the growth rate might be immediately estimated using the total stack thickness obtained with SE.

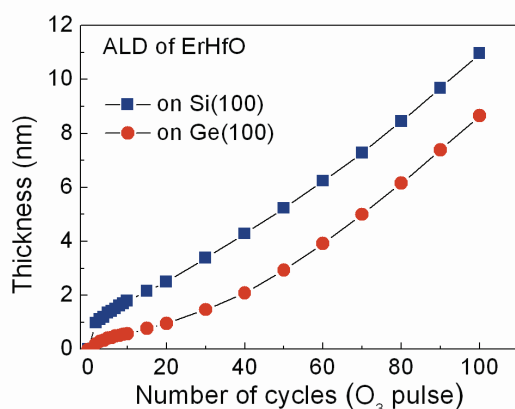


Figure 6.6: Film thickness evolution monitored by *in situ* SE during ALD growth on Si(100) and Ge(100). ALD of ErHfO (Er ~15%) from Er(¹PrCp)₃, HfD-04 and O₃ at 300 °C.

However, it is worth to carefully discuss the actual definition of ALD growth rate. Ideally, the growth rate is defined as the amount/thickness of material deposited per each ALD cycle and it is usually expressed in Å (or nm)/cycle. In case of ternary ALD processes instead of cycle, one can refer to the number of oxygen precursor (i.e. O₃) pulses. To simplify the discussion of the data, we count an ALD cycle after every O₃ pulse and therefore we will not distinguish and discuss here the difference between the binary “sub-cycles” or the ternary ALD “super-cycles”. However, we must bear in mind that every five O₃ pulses actually constitute a super-cycle in which we have performed four HfO₂ ALD sub-cycles and one Er₂O₃ ALD sub-cycle. The growth rate is commonly calculated dividing the total film thickness by the total number of ALD cycles; we arbitrarily can define this as the *stack growth rate* (*stack gr*). For the ALD process shown in Figure 6.6, a *stack gr* $\sim 1.10 \pm 0.05$ Å/O₃ pulse and $\sim 0.90 \pm 0.05$ Å/O₃ pulse is calculated on Si(100) and on Ge(100), respectively. This calculation takes into account the whole stack thickness and the total number of ALD cycles as it might be done in a standard *ex situ* approach. Nevertheless, from Figure 6.6, it appears clear that the ALD process is evidently characterized by two different kinds of nucleation behaviors on the two different substrates. On H-terminated Si(100), the growth looks enhanced at the beginning of the deposition; on the contrary, on native oxide free Ge(100), a nucleation delay is revealed. Therefore, it is reasonable to infer that the calculated *stack gr* values could be affected by these two different types of nucleation.

Actually, using data acquired by *in situ* SE, it is possible to plot the evolution of this *stack gr* versus the number of ALD cycles (O_3 pulse) as shown in Figure 6.7. This plot additionally suggests that, regardless of the substrate, we have two different growth regimes during ALD of ErHfO. Indeed, anomalous growth rate values are observed on both Si(100) and Ge(100) at the beginning of the deposition.

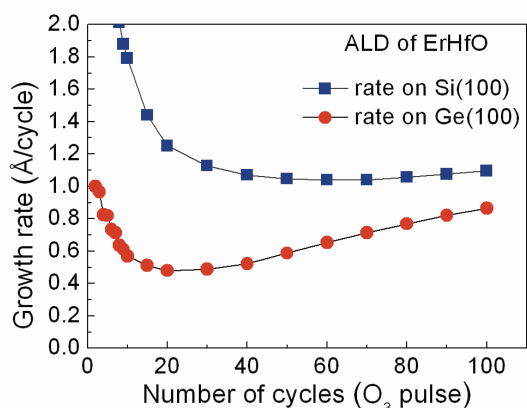


Figure 6.7: Growth rate evolution monitored by *in situ* SE during ALD growth on Si(100) and Ge(100). ALD of ErHfO (Er ~15%) from $Er(^iPrCp)_3$, HfD-04 and O_3 at 300 °C.

On Si(100), during the first 20 cycles, the *stack gr* is always higher than 1.10 Å/ O_3 pulse. Latterly, increasing number of cycles, it is possible to appreciate a sort of convergence of the curve towards the previously calculated *stack gr* value. This initial deviation can be directly associated to the formation of an IL during the early stages of the deposition. The use of O_3 , which is a powerful oxidizing agent, likely promotes the oxidation of the Si(100) surface concomitantly with the formation of the first ErHfO monolayers.

The fast oxidation of Si(100), clearly revealed by *in situ* SE study, is corroborated by HRTEM analysis performed on a ~10 nm thick as-grown stack (Figure 6.8). An amorphous and well defined structural IL of clear contrast is formed atop the Si(100). The clear contrast is the signature of a silica-rich layer; the thickness of this IL is ~1.3 nm. As revealed by the STEM-EELS elemental profiles (Figure 6.8(b)) of Si, O, Hf and Er, the area very near the interface is silica-rich and it becomes richer in Hf and Er and poorer in Si as the distance from the substrate increases.

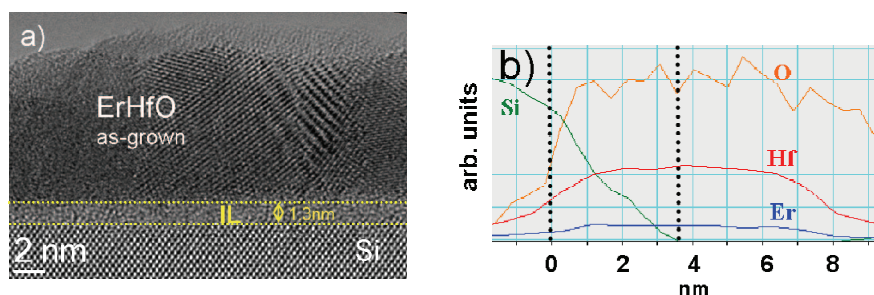


Figure 6.8: (a) HRTEM cross section of as-grown ErHfO film deposited on H-terminated Si(100). (b) STEM-EELS profiles acquired on the same stack.

On Ge(100) the situation looks completely different. In this case, as can be deduced by looking at the Ge related curve in Figure 6.7, the *stack gr* in the early stages of the deposition behaves differently. As opposed to the Si(100) case where growth was initially enhanced and then was constantly slowing during the first 20 cycles, on Ge(100) the growth appears to be somehow inhibited for a while, before

recovering towards a stabilized value. This behavior might be associated to a sort of nucleation delay which is probably occurring on the surface treated with HF [10]. Contrarily to what might be expected [11], O_3 does not seem to promote any sudden oxidation of the Ge substrate and from *in situ* SE analysis we can exclude the initial formation of a GeO_2 -like IL. This speculation is in agreement with the absence of a clear amorphous IL as revealed by HRTEM cross section of an as-grown ErHfO/Ge(100) stack (~ 10 nm thick) shown in Figure 6.9(a).

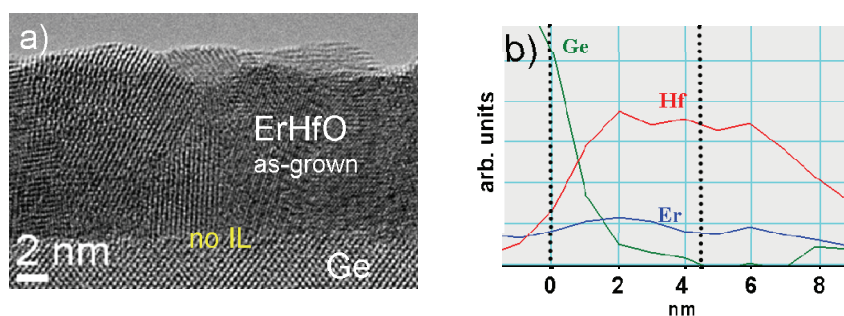


Figure 6.9: (a) HRTEM cross section of as-grown ErHfO film deposited on native oxide free Ge(100). (b) STEM-EELS profiles acquired on the same stack.

Even though there is no “structural” IL atop of Ge(100), a “chemical” IL can be identified. The intermediate Ge, Hf, Er and O STEM-EELS profiles (Figure 6.9(b)) in the area of graded composition are very similar to that obtained in film deposited on Si(100). However, the Ge profile is not associated with the existence of an isolated amorphous IL as evidenced on Si(100). As corroborated by ToF SIMS analysis on as-grown stacks (see Chapter 4), the “chemical” IL is the result of Ge diffusion from the substrate which is actually occurring during the ALD growth. The “structural” IL that forms on Si(100) has a silicate-like composition and it is found amorphous. On the contrary, on Ge(100) the “chemical” IL detected at the interface is crystalline. We may attribute the markedly different growth rates displayed by the *in situ* SE analysis to the latter fundamental structural difference. In addition to that, Ge atoms outdiffusion could additionally explain the transient region evidenced in the growth rate curve obtained during ALD on Ge(100).

Growth rate study: combination of *in situ* SE and XRR characterization

Given the previous discussion on the IL formation and its chemical nature in the two different oxide/semiconductor substrate stacks, a more detailed discussion on the growth rate calculation can be done. Indeed, looking at the evolution of the *stack gr* through *in situ* SE analysis, it has been possible to probe the IL formation or the film nucleation delay, and to distinguish those initial phases from the linear part of the ALD process. These findings corroborate the idea that the calculated *stack gr* values are affected by the presence of even completely different types of nucleation. Further proof of the fact that the IL formation must be considered, is that the final film thickness obtained from *in situ* SE was confirmed by XRR measurements provided that the presence of an extra layer between the ErHfO and the substrate was taken into account for both stacks. For this kind of stacks, XRR analysis can precisely provide the thickness of the actual ErHfO layer while, for the IL thickness, an uncertainty might be present depending on its electronic density. The thickness of this IL can be reasonably estimated comparing the stack thickness measured by SE and the actual ErHfO thickness measured by XRR.

$$\text{IL thickness} = \text{stack thickness} - \text{ErHfO thickness}$$

If we calculate the *stack gr* using the thickness of the ErHfO measured by XRR we get an inaccurate value due to the fact that we are not considering the IL and thus underestimating the total thickness, while the number of cycles is still the same. For example, in the case of ErHfO grown on Si(100) we obtain $\sim 1.00 \pm 0.05 \text{ \AA/O}_3$ pulse.

In situ SE allows us to distinguish between the formation of the IL, which occurs during the first 20 cycles, and the following “pure” growth of the ErHfO film. Indeed, Figure 6.7 shows that after the formation of the IL, the *stack gr* tends towards a constant value. Hence, in the light of the *in situ* SE analysis, the whole ALD process on Si(100) can be divided in two parts.

- IL formation, occurring during the first 20 ALD cycles
- *steady state* ALD of ErHfO after 20 ALD cycles

We can arbitrarily define *steady state gr*, the growth rate which can be obtained from linear regression analyses of the *in situ* SE data acquired after at least 20 ALD cycles. This *steady state gr* is not affected by the IL formation contribution and can be ideally considered as the real ALD growth rate of an ErHfO film. Linear regression performed on *in situ* data provides a *steady state gr* of $1.12 \pm 0.05 \text{ \AA/O}_3$ pulse. A further calculation that can be accomplished is based on the use of the ErHfO thicknesses extracted using XRR and a “corrected” number of ALD cycles provided on the basis of *in situ* SE analysis. Indeed, the speculations made on the IL formation using *in situ* characterization can allow us to correct the total number of cycles to be employed in combination with the thickness of the ErHfO measured by XRR. The calculation based on XRR thickness and a number of cycles corrected subtracting 20 (i.e. the number of cycles responsible of the IL formation) gives a *steady state gr* of $1.15 \pm 0.05 \text{ \AA/O}_3$ pulse, in excellent agreement with the linear regression made on the *in situ* SE data. The same approach can be followed to discuss the growth rate calculation for ALD of ErHfO on Ge(100). *In situ* SE clearly reveals the formation of a more complicated IL which is probably generated from the intermixing of ErHfO with the Ge atoms of the substrate. We ruled out the formation of an additional distinct GeO₂ IL during ALD therefore most likely consider a germanate-like compound. Although in this case it is more complicated to define a precise number of cycles responsible of the IL formation, it is however possible to roughly estimate this number from Figure 6.7. Taking into account 50 cycles, the calculation based on XRR thickness analysis performed on ErHfO/Ge(100) stack gives a *steady state gr* of $1.15 \pm 0.05 \text{ \AA/O}_3$ pulse, in excellent agreement with the results obtained with the same approach on films grown on Si(100). On the basis of these results we are prone to conclude that the *steady state gr* of the ErHfO ALD process can be considered independent on the starting substrate, provided that the crystallographic phase of the films is the same.

In situ characterization of Er-doped HfO₂

In situ SE was also employed to characterize the ALD of Er-doped HfO₂ films, with a variable Er content, on Ge(100). In Figure 6.10 film thickness as a function of number of ALD cycles is shown for HfO₂, Er-HfO₂ (Er content 8% and 15 %) on native oxide free Ge(100). In addition, data of ErHfO (Er 15%) grown on H-terminated Si(100) are reported for a direct comparison.

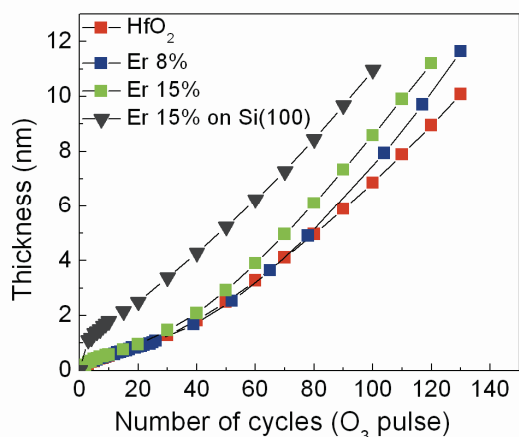
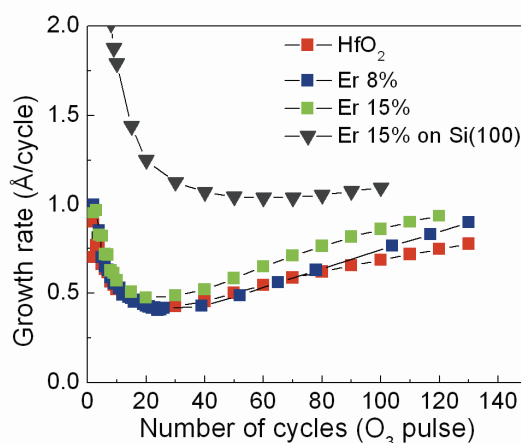


Figure 6.10: Film thickness evolution monitored by *in situ* SE during ALD growth on Si(100) and on Ge(100). ALD of Er-doped HfO₂ (Er = 0 - 8 - 15%) from Er(¹PrCp)₃, HfD-04 and O₃ at 300 °C.

From this plot, it immediately turns out that the growth regime on Ge(100) is confirmed as completely different than the one obtained on Si(100), thus corroborating the previous detailed discussion. The *stack gr* is found to increase on Ge(100) with the increase of the Er content. Indeed, the lowest *stack gr* is calculated for HfO₂ while the higher is obtained for ErHfO (Er 15 %). Furthermore, using data acquired by *in situ* SE it is possible to plot the evolution of the *stack gr* versus the number of O₃ pulses for all the ALD processes (Figure 6.11).

Figure 6.11: Growth rate evolution monitored by *in situ* SE during ALD growth on Si(100) and on Ge(100). ALD of Er-doped HfO₂ (Er = 0 - 8 - 15%) from Er(¹PrCp)₃, HfD-04 and O₃ at 300 °C.



This analysis confirms a remarkable difference in the nucleation behavior on Si(100) and on Ge(100). Although it is not possible to detect any influence of the Er content on the shape of the curves in the early stages of the deposition, the trend in the *stack gr* behavior is evidently confirmed with the increase of the number of cycles. The fact that an increase of the Er content promotes an increase of the *stack gr* might be explained referring to the different global reactivity of the overall ALD cycle, which is probably associated to the introduction of a larger amount of Er precursor [i.e. Er(¹PrCp)₃].

APPENDIX: SE modeling of ultra thin films

Considering the data acquired on Si(100), from the *in situ* SE measurements we can perceive that a fast growth is occurring during the first 20 ALD cycles. This is represented by the high growth rate values which are calculated and displayed in Figure 6.7. Moreover, from XRR and ToF SIMS *ex situ* analysis, we already know that an IL clearly forms between the ErHfO film and the H-terminated Si(100). An alternative approach to the one discussed in Chapter 6, is to formulate some hypotheses with the aim to fit the *in situ* SE data minimizing the MSE value. In this respect:

- ❖ we can assume that the film which is growing is pure ErHfO
- ❖ we can assume that during the first 20 cycles we are actually depositing pure HfO₂ since the Er content should be extremely low (only four cycles)
- ❖ we can assume that O₃ is playing a leading role in the ALD surface chemistry since it is a well known strong oxidizing agent toward Si(100) surface

On the basis of the previous assumptions, different optical constants are assumed in the different SE models. Those models can be validated by comparing the thickness values and the MSE values that come out using different approaches. In Figure 6.12 all the extracted thickness values are illustrated, while in Figure 6.13 the comparison between the MSE values is shown.

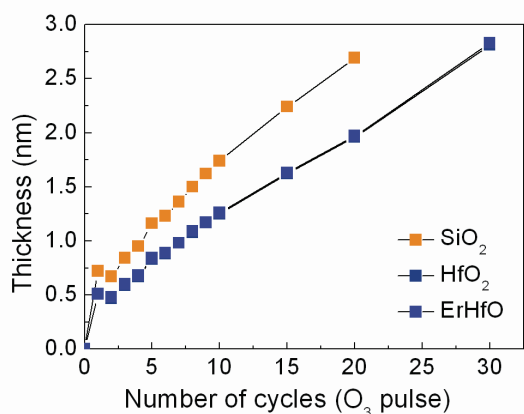
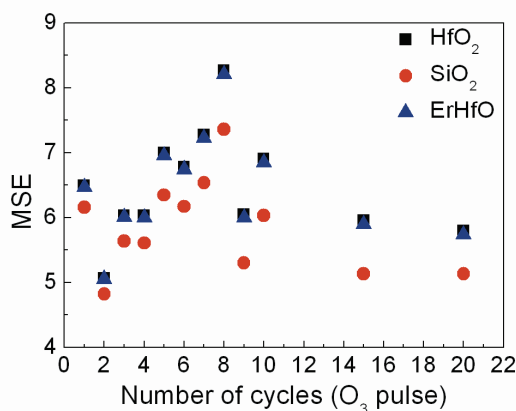


Figure 6.12: Thickness values obtained by using 3 different SE models on Si(100). The data obtained using HfO₂ and ErHfO models are overlapped.

The film thickness seems not to be affected by the use of the HfO₂ or ErHfO optical constants. In the same way, the MSE values obtained with those two approaches for all the fits performed at different number of cycles appear to be almost the same and actually never improved.

Figure 6.13: MSE values obtained by using 3 different SE models on Si(100).



Conversely, a clear trend in reducing the MSE values is obtained when the optical constants of SiO₂ are used to fit the first 20 cycles of the ALD growth on Si(100). This scenario is in very good agreement with the hypothesis that a strong undesired oxidation of Si(100) is here being promoted by the use of O₃. In this case *in situ* SE is providing important information about the SiO₂-like character of the interface between ErHfO and Si(100). *In situ* SE is here giving an insight into the optical properties of the IL between the high-*k* oxide and the Si(100). We must however always bear in mind that the modeling of an IL using SE can be extremely tricky when such analysis is not integrated with complementary techniques.

Modeling of the optical properties at the interface ErHfO/Si and ErHfO/Ge

In order to address the actual optical properties of the interface region and thus of the IL, we might consider an ultra thin (<5 nm) stack which has been characterized with XRR, SE and HRTEM. Optical constants of ErHfO are obtained from the analysis of 30 nm thick film. Then, these optical constants are kept fixed during the analysis of the thinner ErHfO film, thus assuming that the optical constants remain the same regardless of the total thickness. XRR reveals a thickness of thin ErHfO film $\sim 2.3 \pm 0.1$ nm. Thus it is possible to fix it in the model. Using such input XRR thickness while doing SE analysis is acceptable and both techniques can often provide reliable complementary information. The unknowns at this point are thickness and optical constants of the interface region. The stack (ErHfO + IL) is initially modeled as a single film using Cauchy (fitting A_n parameter and thickness). This provides a combined thickness of 4.3 nm. Thus it is possible to subtract ErHfO thickness (obtained using XRR) from the stack thickness (obtained using SE) to give $4.3 - 2.3 = 2$ nm. It is worth noticing the fact that the aforementioned thickness analysis appears in excellent agreement with HRTEM measurements that reveals, as shown in Figure 6.14, an ErHfO and IL thickness of ~ 2.3 and ~ 1.5 nm, respectively.

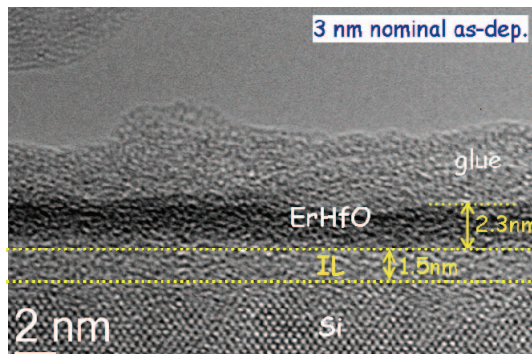


Figure 6.14: HRTEM cross section of as-grown, 3 nm nominally thick, ErHfO film grown on H-terminated Si(100).

Provided that the IL thickness is actually ~ 2 nm and being $A_n=1.808$, the IL refractive index dispersion (Figure 6.15) can be unambiguously calculated.

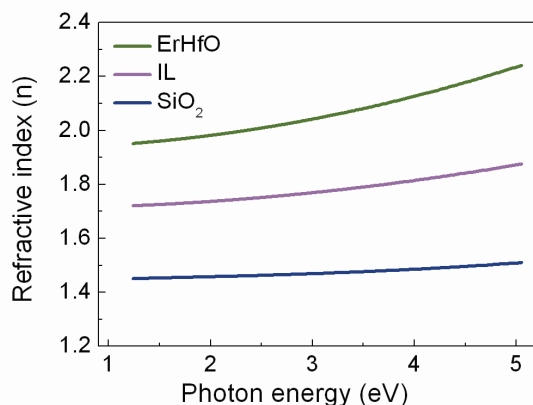


Figure 6.15: Refractive index dispersion of the IL compared with the dispersions of SiO₂ and ErHfO.

References

- [1] E. Langereis, S. B. S. Heil, H. C. M. Knoop, W. Keuning, M. C. M. van de Sanden, and W. M. M. Kessels, *J. Phys. D: Appl. Phys.* **42**, 073001 (2009).
- [2] E. Langereis, PhD Thesis “*Plasma-assisted atomic layer deposition - an in situ diagnostic study*”, Eindhoven University of Technology (2008).
- [3] H. G. Tompkins, *A user’s guide to Ellipsometry*, Dover Publications, Inc., Mineola, New York (1993).
- [4] H. G. Tompkins and E. A. Irene, “*Handbook of Ellipsometry*”, W. Andrews Inc., New York (2005).
- [5] J. A. Woollam Co., Inc., 645 M street, suite 102 Lincoln, NE 68508-2243 (USA).
- [6] Guide to using WVASE 32, J. A. Woollam Co., Inc., (www.jawoollam.com).
- [7] J. A. Woollam Co., Inc., 645 M street, suite 102 Lincoln, NE 68508-2243 (USA).
- [8] Guide to using WVASE 32, J. A. Woollam Co., Inc., (www.jawoollam.com).
- [9] E. D. Palik, “*Handbook of Optical Constants of Solids*”, Academic Press, (1985).
- [10] A. Delabie, R. L. Puurunen, B. Brijs, M. Caymax, T. Conard, B. Onsia, O. Richard, W. Vandervorst, C. Zhao, M. M. Heyns, M. Meuris, M. M. Viitanen, H. H. Brongersma, M. de Ridder, L. V. Goncharova, E. Garfunkel, T. Gustafsson, W. Tsai, *J. Appl. Phys.* **97**, 064104 (2005).
- [11] S. Spiga, C. Wiemer, G. Tallarida, G. Scarel, S. Ferrari, G. Seguini, and M. Fanciulli, *Appl. Phys. Lett.* **87**, 112904 (2005).

Chapter 7

Thermal and Plasma-Assisted Atomic Layer Deposition of Ruthenium thin films^{*}

^{*}This research work was carried out during the three months internship spent in the Plasma & Materials Processing group at the Department of Applied Physics of the Eindhoven University of Technology in the Netherlands.

Introduction on Plasma-assisted ALD

Plasma-assisted (or Plasma-enhanced) ALD is a novel configuration which is nowadays becoming more popular amongst semiconductor industries and thin films research groups. In this ALD configuration, the idea is to benefit from the additional reactivity that can be provided by plasma species during the second half of the ALD cycle [1,2,3]. Therefore, a part of the energy required for the ALD chemical reactions is supplied by the reactants that are activated in the gas phase. The plasma species that contribute to the ALD reactions can be generated either in direct or in remote plasma configuration and several feed gasses can be used for this aim.

Plasma-assisted ALD of oxides [4,5,6], nitrides [7,8,9], and metals [10,11] has already been successfully demonstrated and is currently broadly investigated by the materials research community. Amongst the several potential merits of plasma-assisted ALD it is worth to underline [12]:

- the possibility to deposit films at reduced deposition temperatures in comparison to thermal ALD
- the potential increase of the growth rate of some processes together with the possibility to shorten the overall cycle length
- the chance to extend the choice of materials that can be deposited by ALD processes and to introduce alternative dopant elements during the plasma step

In particular, plasma-assisted ALD of metals can be considered especially interesting and promising for the realization the next generations of DRAM devices. Indeed, the thickness of the metal layers employed in such ultra scaled structures must continuously decrease while retaining the necessary low resistivity. At the same time, the deposition of such metal films has to fulfill the conformality requirements of complex three dimensional structures with a high aspect ratio. In this respect, plasma-assisted ALD is a growth technique that might successfully be employed for the conformal deposition of high quality metal thin films. A potential promising metal electrode that might be integrated in future high density trench capacitors, for DRAM technology, is Ruthenium (Ru). In fact, this noble metal is characterized by a low resistivity ($\sim 7 \mu\Omega \times \text{cm}$ [13]) and by an adequate chemical stability in contact with the ultra high- k dielectrics (e.g. SrTiO_3 , BaTiO_3) that are currently under investigation for the fabrication of advanced MIM capacitors [14,15,16,17]. Moreover, Ru presents a strong resistance against oxidation and can be chemically etched, thus resulting compatible with the standard CMOS process flow [18]. So far, thermal and plasma-assisted ALD of Ru thin films from various precursors have been reported in literature [10,19,20]. In general, polycrystalline metal layers have been obtained with a satisfactory resistivity close to the bulk value. However, critical issues such as the ALD nucleation delay [14,19,20], the film roughness or the formation of an undesired interfacial layer (IL) with the substrate appeared to be directly dependent on the growth conditions. In this regard, the choice to employ a plasma gas as a reducing agent for Ru precursors is a potential feasible way to efficiently deposit smooth and dense Ru films with fairly high growth rates. It is worth considering that NH_3 plasma has been mostly investigated for plasma-assisted ALD of Ru films. However, the use of NH_3 might result in undesired chemical modifications of the oxide film that should be sandwiched in a MIM stack. More specifically, the formation of metal nitrides or the reduction of the oxide layer may occur, actually modifying the nature of the dielectric and thus affecting the final electrical properties of the capacitor. In this respect, the use of O_2 for ALD of Ru films would lead to the development of a more compatible metal process or even to a fully O_2 -based ALD process for the fabrication of a MIM stack.

In this work, we have developed and investigated both thermal and plasma-assisted ALD of Ru thin films grown using a novel and more volatile Ru precursor in combination with O_2 . For these two ALD processes we have addressed a major issue such as the film nucleation behavior by means of an *in situ* monitoring of the early stages of the deposition and of a structural and chemical analysis of the properties at the substrate/Ru interface.

Experimental details

ALD of Ru film was performed using $\text{CpRu}(\text{CO})_2\text{Et}$ (SAFC Hitech) as Ru source and O_2 gas or O_2 plasma for the thermal and plasma-assisted configuration, respectively. The depositions were performed at a growth temperature of 400°C in a FlexAL remote plasma ALD reactor (Figure 7.1, Oxford Instruments), which is reported in Ref. [6].

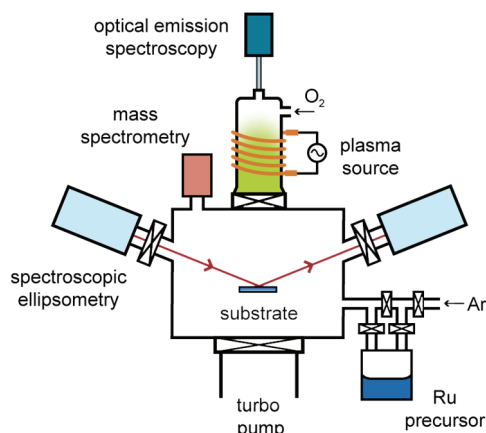


Figure 7.1: Sketch of the FlexAL remote plasma ALD reactor.

ALD of Ru films was performed on top of 6-8 nm thick TiN buffer layers which were grown on Si(100) using plasma-assisted ALD. TiN films were deposited on n-type Si(100), with native SiO_2 on top, using TiCl_4 in combination to a $\text{H}_2\text{-N}_2$ (10:1) gas at 400°C [7]. The choice of TiN as substrate for the Ru depositions was made in the light of its potential technological employment, coupled with Ru, in fabricating multilayer electrodes [18,21]. An ALD cycle for the deposition of Ru consisted of a $\text{CpRu}(\text{CO})_2\text{Et}$ pulse, followed by a purge with Ar gas, and subsequently an O_2 gas (for thermal ALD) or an O_2 plasma (for plasma-assisted) exposure followed by another Ar gas purge and a final pumping down to the base pressure ($<10^{-6}$ Torr). For plasma-assisted ALD, the plasma was preceded by a 2 s long O_2 pre-exposure to stabilize the flow; the O_2 plasma was ignited for 800 ms. Film growth was monitored by *in situ* SE performed through two diagnostic ports located at 70° with the normal to the substrate stage. More details about the optical modeling of Ru thin films will be given in the Appendix of the chapter. Ru films, grown with the two different ALD processes, were thoroughly characterized by means of XRR, XRD, AFM, ToF-SIMS and SE measurements.

Results

A clear nucleation delay, being directly dependent on the ALD process configuration (thermal or plasma) employed for the Ru deposition, was observed on the TiN films used as starting surface. More specifically, for plasma-assisted ALD the growth starts earlier than for thermal ALD. As shown in Figure 7.2, the use of O_2 plasma promotes a faster film nucleation. *In situ* SE reveals the formation of an initial ultra thin layer on the TiN substrate between 50 and 60 cycles. Differently, for thermal ALD *in situ* analysis detects the actual beginning of the films growth between 70 and 80 cycles.

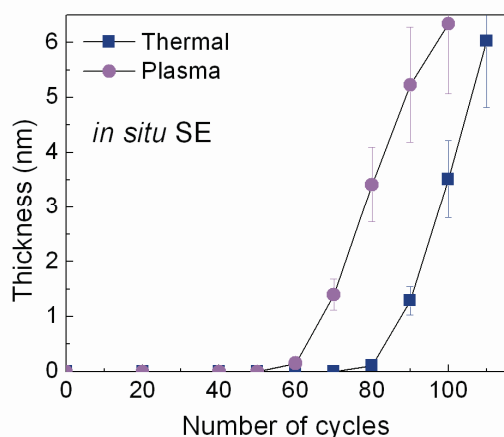


Figure 7.2: Plot of the Ru film thickness evolution vs number of ALD cycles. Thickness was measured every 10 cycles by *in situ* SE. A different nucleation delay is detected for thermal (blue) and plasma-assisted (magenta) ALD.

The increase of the film thickness observed through the SE measurements can be associated, in both cases, to the actual Ru deposition. However, also the oxidation of the TiN surface must be taken into account considering the significant exposure of TiN surface to both O₂ gas and O₂-plasma pulses during the film nucleation. Indeed, the growth rate calculated during the early stages of the deposition appears fairly high (~2.0 Å/cycle) thus suggesting the presence of additional reactions occurring at the surface. Therefore, only an overall growth rate of the stack can be deduced from this analysis and the measured thickness is the result of the Ru growth and the TiN oxidation. Nevertheless, although large error bars have to be considered, in both cases the different nucleation delays are well evidenced. Thermal and plasma-assisted ALD showed a fairly linear increase of film thickness with number of cycles. In Figure 7.3, the thicknesses measured by XRR are plotted; a growth rate $\sim 1.0 \pm 0.1$ Å/cycle for both processes can be calculated from the slope of the linear fit of the data. Lower growth rates were reported in literature for both thermal and plasma-assisted ALD using different Cp-based Ru precursors, e.g. RuCp₂, Ru(EtCp)₂ [22,23] in combination with O₂ or NH₃, respectively. The differences in reactivity may be associated either to the different nature (i.e. steric hindrance) of the Ru complexes or by the use of different gasses in the plasma-assisted ALD configuration. A rough estimation of the nucleation delay can be obtained also from this plot by looking at the intercept of the extrapolated linear fit with the x-axis. Interestingly, it seems that the deposition starts after ~80 cycles for thermal ALD and after ~40 cycles for plasma-assisted ALD, in fairly good agreement with the results obtained by the *in situ* SE analysis.

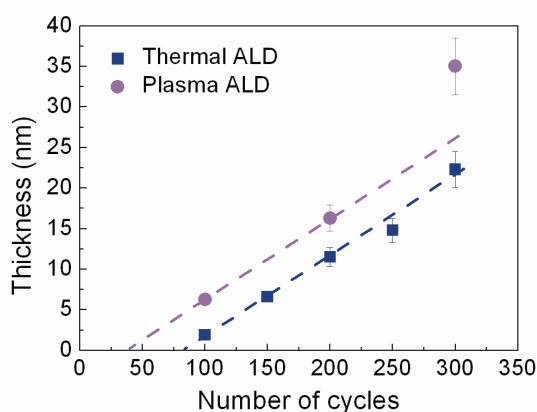


Figure 7.3: Plot of film thickness vs number of ALD cycles for films grown by thermal (blue) and plasma-assisted (magenta) ALD. Thickness was measured by XRR.

Also for XRR analysis, large error bars have to be taken into account, due to the fairly high surface roughness of the films that may significantly affect the thickness estimation. Indeed, AFM measurements (data not shown, acquired on 15 nm thick films) revealed a considerably high surface roughness being ~5 nm and ~10 nm in films grown by thermal and plasma-assisted ALD, respectively. The data point that represents the thickest film grown with plasma-assisted ALD lies far from the linear plot region also for unexpected process issues arose during the growth.

XRD analysis performed on Ru films (Figure 7.4) grown either with thermal or plasma-assisted ALD unveils no structural differences. In both cases it is evidenced a polycrystalline material which displays the expected Ru cell parameters [24]. Differently from what reported for plasma-assisted ALD of Ru films using NH_3 [10,20], no preferential crystalline orientation is revealed.

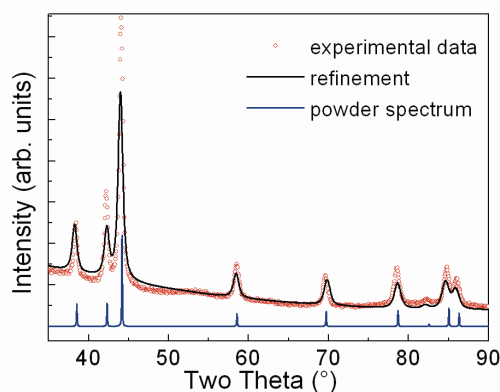


Figure 7.4: XRD analysis of Ru film. Red dots: experimental data. Black continuous line: Rietveld refinement. Blue line: powder spectrum of Ru is reported as reference.

From the XRR measurements performed on Ru films, electronic density of $\sim 3.0 \pm 0.05 \text{ e}^-/\text{\AA}^3$ for films grown using thermal ALD and of $\sim 2.8 \pm 0.05 \text{ e}^-/\text{\AA}^3$ for films grown using the plasma-assisted configuration are calculated. The electronic density obtained from the XRR fits is lower than the reference value of $3.25 \text{ e}^-/\text{\AA}^3$ [24]. It must be noted that XRR data analysis might be directly affected by film roughness. Due to the polycrystalline nature of the layers, and to the fairly high surface roughness evidenced by AFM, the estimation of the electronic density values might be slightly conditioned. However, due to the fact that the lattice parameters measured by XRD are very close to those reported in literature, XRR measurements suggest a structure of Ru grains with some voids between them. This involves that the low electronic density is not caused by deposition of less dense Ru films, but because fully crystallized Ru grains are separated by some voids or by some low-density, amorphous boundaries. Consequently, by combining the electronic density and thickness obtained from XRR, the mass densities of the Ru films were calculated to be $\sim 10 \text{ g/cm}^3$ and $\sim 11 \text{ g/cm}^3$ for thermal and plasma-assisted ALD, respectively. These mass densities are slightly lower than 12.4 g/cm^3 ; that is the value expected for bulk Ru [23]. In order to tentatively address the origin of the two different Ru nucleation behaviors on TiN probed by means of *in situ* SE (Figure 7.2) and *ex situ* XRR (Figure 7.3); ToF SIMS chemical depth profiles were acquired. Figure 7.5 shows the profiles of Ru films, ~ 20 and $\sim 30 \text{ nm}$ thick, grown by thermal and plasma-assisted ALD, respectively.

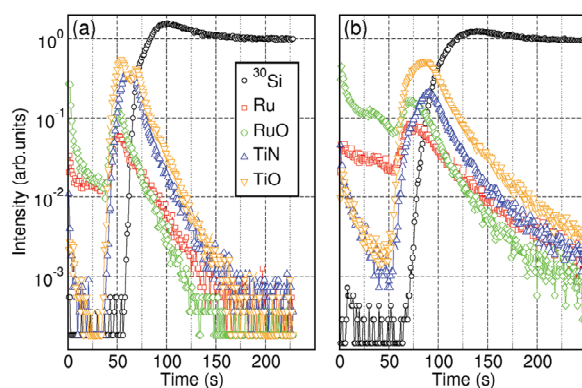


Figure 7.5: ToF SIMS depth profiles acquired on thick Ru films grown by (a) thermal ALD and (b) plasma-assisted ALD.

As far as the TiN layer is concerned, in Figure 7.5(a) a relevant TiO signal is present; actually two peaks of the TiO signal are evidenced. This finding can be attributed to the formation, during thermal ALD of Ru, of two oxidized interfacial regions respectively placed at the TiN/SiO₂ interface and at the Ru/TiN interface. Differently, for the Ru film grown using plasma-assisted ALD (Figure 7.5(b)), the TiO signal presents a unique broad peak which is actually overlapped along the time axis to the TiN signal. This broad peak is more likely associated with the presence of a significant amount of TiO species throughout the whole TiN layer. This scenario might be even consistent with the hypothesis of the formation of a full TiN_xO_y layer. However, in both cases also the exposure to ambient air of the TiN layer before the Ru depositions could have probably affected the TiN/SiO₂ interface composition. A well defined Ru layer is evidenced on top of the TiN film for both thermal and plasma-assisted deposition. Oxygen is detected inside the Ru layer (RuO signal, Figure 7.5); it is likely present in a very low amount and hence it can be considered just as a contaminant species. The oxygen content in the Ru layer is comparatively higher in the film grown using plasma-assisted ALD. ToF SIMS analysis performed on two ultra thin (~2 nm thick) Ru films (Figure 7.6) provided a more detailed and precise close-up of the chemical composition of the interfaces. The Ru and RuO signals are indeed hardly detectable in these cases.

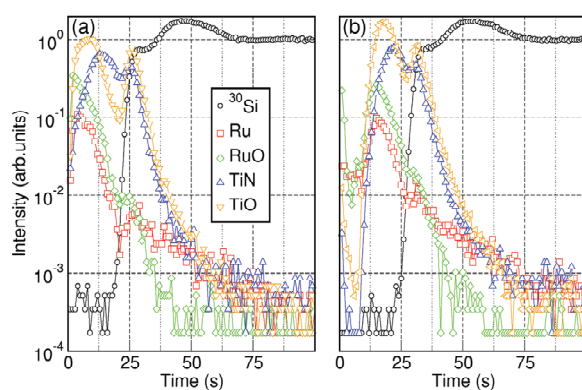


Figure 7.6: ToF SIMS depth profiles acquired on ultra thin Ru films grown by (a) thermal ALD and (b) plasma-assisted ALD.

The interfaces analysis performed on this stack reveals in the case of thermal ALD (Figure 7.6(a)) two peaks of the TiO signal, thus confirming the development of two almost distinct ILs. One IL forms at the Ru/TiN interface during the ALD of Ru, another one forms at the TiN/SiO₂. However, a TiN layer in between the two ILs is fairly defined by the TiN signal. In the stack where Ru was deposited using plasma-assisted ALD (Figure 7.6(b)), the TiO signal is more intense, in particular at the Ru/TiN interface. Differently from what observed in Figure 7.5(b), in this case the TiN signal is not fully overlapped with the one of TiO. This might be explained considering the limited exposure (100 cycles only, equivalent to 80 s of plasma exposure) of the TiN surface to the O₂ plasma if compared to the significantly longer exposure of 300 cycles relative to the thick film deposition. On the basis of the previous analysis, the nucleation behavior and the differences between the thermal and the plasma-assisted ALD processes can be addressed more in detail. The revealed nucleation delay of Ru films on the TiN surface depends on the density and on the reactivity of the surface groups which are involved in the ALD reactions and thus on the consequent density of generated Ru nuclei. It was found that the nucleation behavior also depends on the bonding types between the atoms of the substrate [14,25]. More specifically, when the bonding character is ionic (Metal-Oxygen), the Ru film tends to grow uniformly on the substrate. On the other hand, when the bonding character is more covalent (Metal-non Metal), Ru films grow with the tendency to form discrete nucleation sites and therefore separate islands. The mechanism behind this behavior resides in the fact that, during ALD of Ru, the metal precursor has first to chemically adsorb on the surface to be subsequently reduced by the species

injected in the second half of the ALD cycle. In the O₂-based ALD process, as already reported by Aaltonen *et al.* [26], it is the dissociative chemisorption of oxygen on the catalytic Ru surface which is dictating the film growth. Therefore, there must be favorable conditions for the formation of an intermediate surface Ru complex which temporarily bonds with the surface. The strength of the surface chemical complex directly depends on the nature of the substrate atoms bonding. Given that pure TiN species has a clearly covalent bonding nature, the nucleation of Ru films is in principle quite difficult to succeed. Indeed, a clear nucleation delay is detected during the depositions. Actually, an oxidation of the TiN surface is being promoted by the O₂ gas and O₂ plasma in both the ALD processes employed. This fact is supported by the TiO profiles evidenced by ToF SIMS analysis. The prevailing ionic character of the oxidized TiN surface, being more likely TiO_x or TiN_xO_y, favors Ru growth. Therefore, the actual undesired TiN oxidation plays a key role in the early stages of the deposition defining the nucleation delay. Compared to thermal ALD, the use of O₂ plasma accelerates the Ru film nucleation, probably because of the stronger oxidation of the TiN surface. Ru precursor is favorably chemically adsorbed on a more ionic surface and is then reduced by the oxygen which is catalytically adsorbed on Ru surface. Hence, on a mostly oxidized TiN surface, Ru precursor more easily forms the chemical complexes with the substrates enhancing the nucleation probability. This might explain the differences found by *in situ* SE analysis and XRR thickness study and could clarify the effect of the O₂ plasma on the nucleation behavior. On the other hand, another speculation about the faster nucleation revealed for plasma-assisted ALD can be done. Inside the O₂ plasma, the molecules dissociation process leads to atomic radicals, ions and electrons. The presence of dissociated oxygen within the O₂ plasma may be beneficial for the Ru film nucleation. Indeed, during plasma-assisted ALD the dissociative chemisorption of oxygen on the catalytic Ru surface is accompanied by a direct supply of dissociated O₂ which is coming from the plasma. This mechanism would further explain the improved nucleation evidenced for the plasma-assisted configuration.

Given the potential technological interest in building multilayer metallic stacks [18,21], it is worth to better investigate the properties of a Ru layer coupled with TiN to be employed as top or bottom electrode in MIM capacitor structures. The successful integration of a Ru film with such an established metal might indeed improve the integrability of Ru in a large scale production. In this respect, a TiN/Ru/TiN trilayer stack was deposited using a full plasma-assisted ALD process. The aim was to address and investigate the details of ALD of Ru atop TiN and vice versa. The three layers were grown sequentially, targeting a thickness of 15 nm for the TiN layers and 10 nm for the Ru layer placed in between. *In situ* SE measurements and *ex situ* XRR characterizations revealed that the stack was composed of ~15 nm as TiN bottom layer, ~7 nm thick Ru film in between, and ~15 TiN top layer. The formation of a ~1 nm thick IL has to be taken into account in the XRR model in between the Ru and bottom TiN. In Figure 7.7, ToF SIMS depth profiles acquired on the TiN_top/Ru/TiN_bottom stack are shown. As expected, the TiN_bottom layer seems partially oxidized (TiO signal) through its overall thickness.

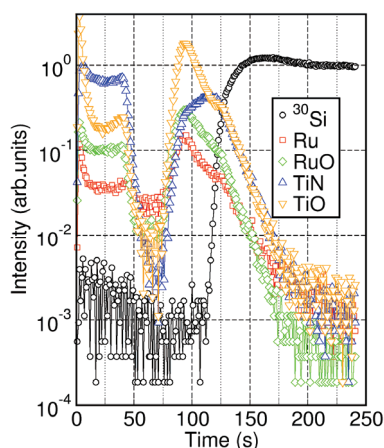


Figure 7.7: ToF SIMS depth profiles acquired on the stack grown by ALD TiN/Ru/TiN.

This result is in line with what was previously discussed for the Ru/TiN interfaces prepared using plasma-assisted ALD and is connected to the use of the O₂ plasma. The Ru film is well identified in between the two TiN layers. Different intensities of Ru signal for different sputtering time can be attributed to the effect of different matrixes being evidenced (e.g. TiN, Ru and TiN_xO_y). The second interface (TiN_top/Ru) looks really sharp and no intermediate layers are evidenced. It is worth noticing that no IL and no modifications of the Ru surface occur during the plasma-assisted ALD of the TiN_top layer. On the contrary, XRR reveals that the TiN_top film presents a surface roughness which is very similar to the one detected for the Ru film also by AFM. This might be explained considering the rough polycrystalline nature of the Ru films and the good conformality of TiN thin films grown by ALD. Ru and RuO signals are present through the TiN_top layer suggesting a possible Ru diffusion during the last TiN deposition. On the TiN_top surface, a peak related to the presence of a superficial additional oxidation is also evidenced.

Conclusions

In this work, we have investigated O₂-based thermal and plasma-assisted ALD of Ru thin films grown using a novel Ru precursor on TiN substrates. The material properties obtained with the two different ALD configurations were very similar. In both cases the structural analysis demonstrated the obtainment of pure polycrystalline Ru films deposited on TiN with a growth rate of $1.0 \pm 0.1 \text{ \AA/cycle}$. A suitably low resistivity value $\sim 20 \text{ }\mu\Omega \times \text{cm}$ was measured for the Ru films, regardless of the ALD process employed. The nucleation behavior on TiN substrates, in the light of a possible use of a Ru/TiN electrode stack, was specifically addressed. *In situ* SE monitoring revealed a clear nucleation delay in both cases. Interestingly, an improved nucleation behavior, although associated to an increased surface roughness, was obtained for films grown using plasma-assisted ALD. The use of O₂ results in the oxidation of TiN substrate and likely promotes a more favorable Ru nucleation; this effect is further enhanced by the use of O₂ plasma. Promising ALD processes were demonstrated, together with the obtainment of adequate material properties. A further thorough investigation should be dedicated to ALD of Ru films on ultra high-*k* dielectrics such as SrTiO₃.

APPENDIX: SE modeling of thin metal films

In order to obtain the dispersions of the optical constants of the Ru and TiN films grown with ALD, SE data analysis was performed on the basis of a detailed parameterization of the material dielectric functions (ϵ_1 and ϵ_2). Either *ex situ* or *in situ* SE measurements were employed. For the analysis of the *in situ* SE data, the dispersions were corrected as a function of the sample temperature (see Chapter 6).

The dielectric functions of TiN films, grown with plasma-assisted ALD, were modeled using a Drude-Lorentz oscillator parameterization as reported and discussed in Ref. [7]. Differently, as far as the optical modeling of Ru is concerned, it was not possible to extract film thickness assuming *a priori* the dispersion of the optical constants. In fact, ϵ_1 and ϵ_2 of Ru ultra thin films were initially unknown; the dielectric constants of a thick Ru layer (360-410 nm) proposed by Choi *et al.* [27] were used as initial reference values. The strategy followed to perform the parameterization of Ru dielectric functions was based on the employment of *ex situ* SE measurements characterized by an extended photon energy both in the IR and UV range. Actually, two ellipsometers with a different photon energy range were alternatively employed; appending the data was thus possible to obtain SE spectra in the 0.75 – 6.5 eV range. The method of direct numerical inversion was applied iteratively to extract the dielectric function of Ru from the pseudo-dielectric function of the stack. The film thickness was assumed on the basis of XRR analysis while the dispersion of the optical constants was extracted by means of a point-to-point fit of the SE data [28]. The SE data inversion performed using XRR thicknesses allowed to obtain the dielectric function of Ru. It must be underlined the fact that the fairly high surface roughness of the Ru films certainly affects either the SE measurements or the SE data analysis. The ϵ_1 and ϵ_2 calculated through the direct inversion procedure were found in reasonable agreement with the values proposed by Choi *et al.* [27], as shown in Figure 7.8.

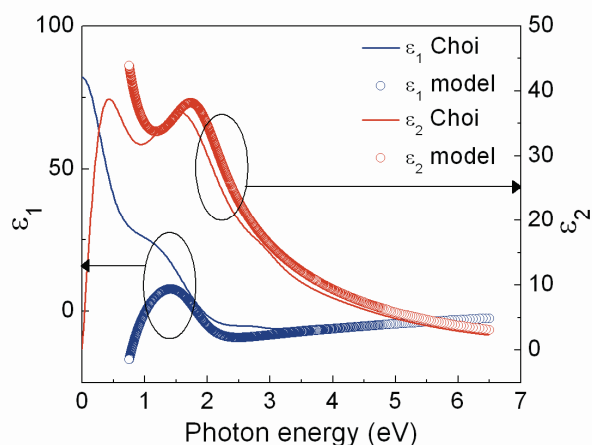


Figure 7.8: Ruthenium ϵ_1 and ϵ_2 spectra calculated by Choi (blue and red continuous lines) and obtained in this work by means of SE optical parameterization (blue and red dots).

A parameterization was then performed to obtain the Ru dielectric functions including different oscillators to describe interband and intraband absorptions. From the theoretical calculations four Lorentz oscillators relative to the interband absorptions are expected for Ru [27]. Actually, the optical parameterization was performed using a combined Drude-Lorentz oscillator model. Two Lorentz oscillators are positioned at ~ 1.7 and ~ 3.0 eV, being in very good agreement with the proposed theoretical values of 1.8 and 2.9, respectively [27]. There is no need to include an additional Lorentz oscillator at 4.1 eV, as suggested theoretically. However, differently from the model proposed in Ref [27], in which a fourth Lorentz term is taken into account at 0.6 eV, at low energy the absorption could be better described by using a Drude term. In fact, a Drude oscillator was added in the SE model to account for the intraband absorptions by conduction electrons in the Ru film. The reason behind this

alternative approach might be associated with the fact that, differently from the calculated optical spectra, the experimental SE data are not extended down to 0 eV. Therefore, the shape of the ϵ_2 peak can be better approximated by a Drude term rather than a Lorentz one. Moreover, in the experimental SE data the Drude part that seems to be present at low energy actually interferes with the Lorentz oscillator that should be placed at 0.6 eV making the modeling more complex in that region. As far as the description of ϵ_1 is concerned, it can be improved including a pole term positioned at very low energy (~ 0.1 eV). The final dispersion model was optimized by fitting Ru samples with different thickness and then checking the stability of all the parameters included in the Drude-Lorentz model.

Given this optimized parameterization of the Ru optical constants, the model obtained was employed to perform the thickness analysis of the films grown either with thermal or with plasma-assisted ALD. The model showed a good consistency and an acceptable dependence on film thickness variation. Moreover, the Ru optical model was employed to perform the analysis of the early stages of the deposition. According to the Drude theory, the Drude oscillator contains information on the metallic properties of the film; therefore it was even possible to estimate the electrical resistivity of the films. Values in the 20-40 $\mu\Omega \times \text{cm}$ range were calculated for films thinner than 20 nm.

References

- [1] M. de Keijser and C. van Opdorp, *Appl. Phys. Lett.* **58**, 1187 (1990).
- [2] S. M. Rosnagel, A. Sherman, and F. Turner, *J. Vac. Sci. Technol. B* **18**(4), 2016 (2000).
- [3] H. Kim and S. M. Rosnagel, *J. Vac. Sci. Technol. A* **20**(3), 802 (2002).
- [4] J. L. van Hemmen, S. B. S. Heil, J. H. Klootwijk, F. Roozeboom, C. J. Hodson, M. C. M. van de Sanden, and W. M. M. Kessels, *J. Electrochem. Soc.* **154**, G165 (2007).
- [5] E. Langereis, M. Creatore, S. B. S. Heil, M. C. M. van de Sanden, and W. M. M. Kessels, *Appl. Phys. Lett.* **89**, 081915 (2006).
- [6] S. B. S. Heil, J. L. van Hemmen, C. J. Hodson, N. Singh, J. H. Klootwijk, F. Roozeboom, M. C. M. van de Sanden and W. M. M. Kessels, *J. Vac. Sci. Technol. A* **25**(5), 1357 (2007).
- [7] E. Langereis, S. B. S. Heil, M. C. M. van de Sanden, and W. M. M. Kessels, *J. Appl. Phys.* **100**, 023534 (2006).
- [8] E. Langereis, H. C. M. Knoop, A. J. M. Mackus, F. Roozeboom, M. C. M. van de Sanden, and W. M. M. Kessels, *J. Appl. Phys.* **102**, 083517 (2007).
- [9] S. B. S. Heil, E. Langereis, F. Roozeboom, M. C. M. van de Sanden, and W. M. M. Kessels, *J. Electrochem. Soc.* **153**, G956 (2006).
- [10] O. K. Kwon, J. H. Kim, H. S. Park, and S. W. Kang, *J. Electrochem. Soc.* **151**, G109 (2004).
- [11] H. C. M. Knoop, A. J. M. Mackus, M. E. Donders, M. C. M. van de Sanden, P. H. L. Notten, and W. M. M. Kessels, *Electrochem. Solid-State Lett.*, **12**, G34 (2009).
- [12] E. Langereis, PhD Thesis "*Plasma-assisted atomic layer deposition - an in situ diagnostic study*", Eindhoven University of Technology (2008).
- [13] D. R. Lide, "*Handbook of Chemistry and Physics*", CRC Press, Boca Raton, 85th edition (2005).
- [14] S. Y. Kang, C. S. Hwang, and H. J. Kim, *J. Electrochem. Soc.* **152**, C15 (2005).
- [15] S. J. Won, W. D. Kim, C. Y. Yoo, S. T. Kim, Y. W. Park, J. T. Moon, M. Y. Lee, *IEDM IEEE* 789 (2000).
- [16] Y. Matsui, M. Hiratani, T. Nabatame, Y. Shimamoto, and S. Kimuraa, *Electrochem. Solid-State Lett.* **4**, C9 (2001).
- [17] J. H. Ahn, J. Y. Kim, S. W. Kang, J. H. Kim, and Jae-Sung Roh, *Appl. Phys. Lett.* **91**, 062910 (2007).
- [18] B. K. Moon, J. Aoyama, K. Katori, *Appl. Phys. Lett.* **74**, 824 (1999).
- [19] T. Aaltonen, M. Ritala, K. Arstila, J. Keinonen, and M. Leskela, *Chem. Vap. Deposition* **10**, 215 (2004).
- [20] S. J. Park, W. H. Kim, H. B. R. Lee, W. J. Maeng, H. Kim, *Microelectr. Eng.* **85**, 39 (2008).
- [21] S. H. Kwon, O. K. Kwon, J. S. Min, S. W. Kang, *J. Electrochem. Soc.* **153**, G578 (2006).
- [22] T. Aaltonen, P. Alén, M. Ritala, and M. Leskela, *Chem. Vap. Deposition* **9**, 45 (2003).
- [23] O. K. Kwon, S. H. Kwon, H. S. Park, and S. W. Kang, *Electrochem. Solid-State Lett.* **7**, C46 (2004).
- [24] Inorganic CrystalStructure Database, file 54236 for Ru.
- [25] K. C. Smith, Y. M. Sun, N. R. Mettlach, R. L. Hance, J. M. White, *Thin Solid Films* **376**, 73 (2000).
- [26] T. Aaltonen, A. Rahtu, M. Ritala, and M. Leskela, *Electrochem. Solid-State Lett.* **6**, C130 (2003).
- [27] W. S. Choi, S. S. A. Seo, K. W. Kim, T. W. Noh, M. Y. Kim, S. Shin, *Phys. Rev. B* **74**, 205117 (2006).
- [28] E. Langereis, S. B. S. Heil, H. C. M. Knoop, W. Keuning, M. C. M. van de Sanden, and W. M. M. Kessels, *J. Phys. D: Appl. Phys.* **42**, 073001 (2009).



Chapter 8

Conclusions

Concerning the innovation in micro- and nanoelectronic, atomic layer deposition (ALD) is certainly considered as one of the most promising growth techniques that could be employed to realize novel ultra scaled devices. The growth of oxides, metals and nitrides with an atomic level thickness control, associated with the possibility to obtain an excellent conformality, represents an outstanding advantage in the deposition of ultra thin films. Spectroscopic Ellipsometry (SE) is one of the most versatile, fast and powerful non-destructive characterization techniques employed in thin films technology to extract the thickness and the optical properties of several materials with an elevated accuracy and sensitivity.

The research work described in this thesis aims at the development of ALD processes for the deposition of ultra thin films of high permittivity (high- k) materials to be employed in the forthcoming low power and high performances micro- and nanoelectronic devices. The ALD processes were developed using novel organometallic precursors and comparing the effect of two different oxygen sources, i.e. H₂O and a more powerful oxidizing agent such as O₃. In particular, the work was focused on the development of ALD of rare earth-based oxides; thus taking into account actual ternary compounds or transition metal oxides doped by rare earth elements. The employment of *in situ* SE allowed performing an efficient and innovative optimization of the ALD recipes. The *in situ* SE study provided remarkable information on the early stages of the growth being capable to probe the oxide/semiconductor interface evolution during the deposition. A thorough and extended *ex situ* structural, chemical and electrical characterization was performed on all the different films. Particular issues were addressed by means of the combination of several characterization techniques; i.e. the formation of an interfacial layer between the oxide and the semiconductor substrate or the effect of doping on the growth rate and on the structural properties of the film.

A section of the research was dedicated to La-based compounds. An O₃-based ALD process was demonstrated as an effective way to achieve the hexagonal La₂O₃ polymorph either on Si or on Ge substrates. In both cases, it was assessed that the occurrence of undesired interfacial reactions represents an obstacle for the scaling of the film physical thickness. However, due to the relevant technological drawbacks associated to the La₂O₃ hygroscopic character, alloying La₂O₃ and ZrO₂ turned out to be a more feasible solution. ALD of LaZrO compound (La content ~25%) was scaled up onto large area industrial wafers and the oxide was tested in non-volatile memory test structures demonstrating encouraging dielectric properties.

Another part of the research was devoted to ALD of Er-based compounds. ALD was demonstrated as a powerful growth technique to obtain different oxide stoichiometries. The consequence of the Er content on the stabilization of metastable phases (i.e. cubic HfO₂) was thoroughly addressed either probing the effects of Er content on the ALD growth rates or investigating the crystalline phases distribution. It was established that remarkable differences, as a function of the semiconductor substrates (e.g. Si or Ge), can be recognized by analyzing different stacks. In this respect, *in situ* SE allowed to systematically compare the same ALD processes on Si and Ge emphasizing the important aspect of the interfacial layer formation.

Furthermore, La₂O₃, La-doped ZrO₂ and Er-doped HfO₂ films were deposited and specifically characterized on high-mobility substrates (i.e. Ge, GaAs and Ge/GaAs stacks).

The alternative plasma assisted ALD configuration was investigated and compared to the thermal ALD approach for the specific case of Ruthenium thin films growth. In this respect, *in situ* SE provided insights on the so-called nucleation delay demonstrating differences between the use of O₂ gas or O₂ plasma. An *ex situ* characterization of the stack interfaces corroborated the latter analysis.

Some of the investigated ALD processes and the related material characterization were proposed to the scientific community through peer-reviewed publications and presentations at international conferences affording dissemination of new knowledge on the different topics that were addressed through the research activity. The dielectrics were proposed to the academic and industrial research communities as novel promising candidates for advanced technology based on both Si- and high-mobility substrates. Concomitantly, a deep understanding of the bulk and interface properties of these oxide/semiconductor substrate stacks has been provided through a careful discussion of the experimental results.

Pursuing the integration of ALD processes for the deposition of rare earth-based dielectrics at an industrial level could provide the possibility of achieving advanced micro- and nanoelectronic devices with improved performances on a very large production scale.

The scientific research on the ALD of rare earth doped oxides and on the doping effects on the material properties will be certainly continued by the scientific community in order to achieve a more exhaustive comprehension of the physical and chemical phenomena involved. Moreover, the actual implementation of rare earth-based dielectrics on high-mobility substrates represents an extremely promising solution for the forthcoming advanced technological nodes. Therefore, this specific topic will attract an ever-increasing attention both of the scientific research community and of the industries.

List of publications related to this work

- 1) G. Scarel, A. Debernardi, D. Tsoutsou, S. Spiga, S. C. Capelli, L. Lamagna, S. N. Volkos, M. Alia, M. Fanciulli, "*Vibrational and electrical properties of hexagonal La_2O_3 films*", Appl. Phys. Lett. **91**, 102901 (2007).
- 2) S. Schamm, P. E. Coulon, S. Miao, S. N. Volkos, H. L. Lu, L. Lamagna, C. Wiemer, D. Tsoutsou, G. Scarel, M. Fanciulli, "*ALD-Grown Rare Earth Oxides for Advanced Gate Stacks*", ECS Transactions **13**, 77 (2008).
- 3) S. Schamm, P. E. Coulon, S. Miao, S. N. Volkos, H. L. Lu, L. Lamagna, C. Wiemer, D. Tsoutsou, G. Scarel, M. Fanciulli, "*Chemical/Structural Nanocharacterization And Electrical Properties of ALD-grown $\text{La}_2\text{O}_3/\text{Si}$ Interfaces For Advanced Gate Stacks*", J. of Electrochem. Soc. **156** (1), H1 (2008).
- 4) H. L. Lu, G. Scarel, L. Lamagna, M. Fanciulli, S. J. Ding, D. Zhang, "*Effect of rapid thermal annealing on optical and interfacial properties of atomic-layer-deposited Lu_2O_3 films on $\text{Si}(100)$* ", Appl. Phys. Lett. **93**, 152906 (2008).
- 5) D. Tsoutsou, G. Scarel, A. Debernardi, S. C. Capelli, S. N. Volkos, L. Lamagna, S. Schamm, P. E. Coulon, M. Fanciulli, "*Infrared spectroscopy and X-ray diffraction studies on the crystallographic evolution of La_2O_3 films upon annealing*", Microelectr. Eng. **85**, 2411 (2008).
- 6) D. Tsoutsou, L. Lamagna, S. N. Volkos, A. Molle, S. Baldovino, S. Schamm, P. E. Coulon, and M. Fanciulli, "*Atomic layer deposition of $\text{La}_x\text{Zr}_{1-x}\text{O}_{2-\delta}$ ($x=0.25$) high- κ dielectrics for advanced gate stacks*", Appl. Phys. Lett. **94**, 053504 (2009).
- 7) X. L. Li, D. Tsoutsou, G. Scarel, C. Wiemer, S. C. Capelli, S. N. Volkos, L. Lamagna, and M. Fanciulli, "*Chemical and structural properties of atomic layer deposited La_2O_3 films capped with a thin Al_2O_3 layer*", J. Vac. Sci. Technol. A **27**, L1 (2009).
- 8) L. Lamagna, G. Scarel, G. Pavia, and M. Fanciulli, "*Investigation of interfacial layer development in thin Al_2O_3 films grown using ALD and $\text{Si}(100)$, $\text{Ge}(100)$ and $\text{GaAs}(100)$* ", J. Vac. Sci. Technol. A **27**, 443 (2009).
- 9) L. Fumagalli, M. Binda, I. Suarez Lopez, D. Natali, M. Sampietro, S. Ferrari, L. Lamagna, M. Fanciulli, "*Multi layer structure for encapsulation of organic transistors*", Organic Electronics **10**, 692 (2009).
- 10) G. Congedo, S. Spiga, L. Lamagna, A. Lamperti, Yu. Lebedinskii, Yu. Matveyev, A. Zenkevich, P. Chernykh, and M. Fanciulli, "*Effect of high-temperature annealing on Lanthanum Aluminate thin films grown by ALD on $\text{Si}(100)$* ", Microelectr. Eng. **86**, 1696 (2009).
- 11) A. Zenkevich, Yu. Lebedinskii, Yu. Matveyev, S. Spiga, L. Lamagna, and M. Fanciulli, "*Effect of heat treatments on electric dipole at metal/high- κ dielectric interfaces measured by in situ XPS*", Microelectr. Eng. **86**, 1777 (2009).
- 12) A. Molle, G. Brammertz, L. Lamagna, M. Fanciulli, M. Meuris, and S. Spiga, "*Ge-based interface passivation for atomic layer deposited La-doped ZrO_2 on III-V compound (GaAs , $\text{In}_{0.15}\text{Ga}_{0.85}\text{As}$) substrates*", Appl. Phys. Lett. **95**, 023507 (2009).

- 13) L. Lamagna, C. Wiemer, S. Baldovino, A. Molle, M. Perego, S. Schamm-Chardon, P. E. Coulon, M. Fanciulli, "*Thermally induced permittivity enhancement in La-doped ZrO₂ grown by atomic layer deposition on Ge(100)*", Appl. Phys. Lett. **95**, 122902 (2009).
- 14) M. Alessandri, A. Del Vitto, R. Piagge, A. Sebastiani, C. Scozzari, C. Wiemer, L. Lamagna, M. Perego, G. Ghidini, M. Fanciulli, "*Rare earth-based high-k materials for non-volatile memory applications*", Microelectr. Eng. **in press** (2009).
- 15) A. Molle, L. Lamagna, S. Spiga, M. Fanciulli, G. Brammertz, M. Meuris, "*Interface analysis of Ge ultra thin layers intercalated between GaAs substrates and oxide stacks*" Thin Solid Films, **in press** (2009).

Acknowledgements

If you ever manage to write a Ph.D. Thesis, this certainly means that you have to acknowledge a huge number of people.

Ho deciso di intraprendere la splendida (ora posso dirlo con certezza) esperienza del dottorato di ricerca dopo aver svolto la tesi di laurea specialistica in MDM. Quando racconto del dottorato sottolineo sempre con piacere sia quanto sia effettivamente contento di aver scelto di fare una tale esperienza sia che la ripeterei immediatamente. E' stato facile ed immediato rimanere affascinati dalla ricerca che si svolge in MDM, dalle sue intriganti tematiche, dalle sfide quotidiane del lavoro in laboratorio ed in clean room ma soprattutto dall'incredibile qualità delle persone che ci lavorano ancora oggi. I miei ringraziamenti vanno innanzitutto a tutti i colleghi del laboratorio.

Inizio da Marco Fanciulli: mi ha accolto in MDM più di tre anni fa come tesista e mi ha poi saputo incuriosire ed attirare in questa esperienza. Durante questi tre anni di dottorato mi ha consigliato, stimolato e guidato, mi ha dato l'opportunità di lavorare sempre su tematiche e con persone di altissimo livello, mi ha permesso di rappresentare il laboratorio a conferenze internazionali facendomi girare mezzo mondo, mi ha sempre fornito strumenti, stimoli e possibilità per crescere a livello professionale e personale. Con lui sono piacevolmente e profondamente indebitato. Ringrazio Leo Miglio, il coordinatore del dottorato, per il suo supporto ed anche per quella chiacchierata stimolante di tre anni fa, prima che iniziasse il tutto.

Proseguo ringraziando Giovanna Scarel: mia correlatrice di tesi di laurea e mio punto di riferimento durante i primi mesi di dottorato. A lei sono associati i miei primi ricordi ed i miei primi passi nella ricerca, di lei non scorderò mai l'entusiasmo e i tanti consigli.

Un ringraziamento speciale va a Claudia Wiemer: per essere stata un costante riferimento ed esempio nel lavoro, per aver saputo rendere semplicemente piacevole ogni momento passato insieme (persino la scrittura di kilometriche deliverables!) e per essere stata una deliziosa compagna di missione, ovunque si andasse.

Molti colleghi in MDM hanno dato un contributo importantissimo per il mio lavoro di ricerca durante il dottorato, ma io li ringrazio soprattutto per l'aiuto, il costante e prezioso supporto scientifico e morale e per tutto quello che mi hanno insegnato. In questi anni ho avuto il grandissimo piacere di lavorare, di collaborare e di condividere tante giornate con: Alessandro Molle, Michele Perego e Silvia Baldovino; Sabina Spiga e Grazia Tallarida, la mia socia di box-scrivania ed ALD Elena Cianci, Gabriele Seguini, Alessio Lamperti, Massimo Longo, Alberto Debernardi, Roberto Mantovan, Enrico Prati, Olivier Salicio, Emiliano Bonera. Ho avuto il piacere di affrontare le più svariate questioni tecniche, IT e tecnologiche con Simone Cocco e Roberto Colnaghi; ho passato giorni, anzi mesi chiuso nella tuta a fianco di Mario Alia ad imparare le gioie ed i dolori della clean room, lo ringrazio per non avermi mai fatto mancare il suo aiuto e per tutti i piacevoli momenti passati insieme al lavoro e sul campo da tennis. Ringrazio per l'appoggio e la tanta pazienza lo staff organizzativo-amministrativo MDM: Mara Lanati, Anna Grazioli, Vania Zoccarato ed Antonella Biondi. Nel corso della mia permanenza in MDM

molte persone sono arrivate, tante altre se ne sono andate. Tra queste ultime un grazie va a Silvia Capelli ed uno a Sandro Ferrari. Un grazie speciale va ad Antonio Vellei ed a Francesca Taraballi, miei compagni unici ed inimitabili di dottorato, di risate e di mille sbattimenti burocratici. In MDM non posso dimenticare il mio primo unico ed inimitabile student-tutor Andrea Cappella, i ragazzi PhD Gabriele Congedo, Roberto Fallica, Andrea Andreozzi, Guido Petretto.

Ringrazio per la disponibilità e per la collaborazione il gruppo della R&D di Numonyx ed in particolare Annalisa Del Vitto, Rossella Piagge e Mauro Alessandri.

There's now a part that has to be dedicated to all the foreign people that I had the pleasure to meet during my PhD; most of them have been working at MDM. I would like to thank for the wonderful time spent together and for the fruitful collaboration Inma Suarez Lopez, Eleni Katsia, Dimitra Tsoutsou, Stelios Volkos and Hong Liang Lu. Special thanks go to Nolwenn Huby (and Fred!) for the amazing extra-work time spent together e per la preziosa amicizia che abbiamo costruito. I've been working in the framework of an European Project together with several partners coming from different european countries. Therefore, there are many other people that I would like to acknowledge for the pleasant time spent together at the meetings and for the extremely interesting and fruitful collaboration within the project. I want to thank the project coordinator Simon Elliott, Alexandra Zydor, Mikko Ritala and Kjell Knapas, Simon Rushworth and Peter Heys, Marko Tuominen and Eva Tois, Tony Jones, Wim Besling, Lars Oberbeck. An outstanding contribution to my research activity was provided by Sylvie Schamm and Pierre-Eugène Coulon. It has been a great pleasure to work with them and I want to thank them for all the scientific discussions, the joint publications, the endless phone calls; for their kindness and professionalism. Merci beaucoup.

I spent three wonderful months working in Eindhoven. A really special "thank you" goes to Erwin Kessels who made it possible, who let me work in his nice group and who also supported me during the preparation of this Thesis. I want to thank for the amazing time spent together at work, in the clean room, at the Borrell and hanging around Renee Verkuijlen, Erik Langereis, Harm Knoops, Noemi Leick, Fred Roozeboom. Furthermore, I want to mention and thank Lianne, Wytze, Stephen, Arno, Teo and Anitha, Gianfranco, Aafke, Gjis, Terje, Willem-Jan, Adri, Floran, Cristina, Harald, Nick, Jan-Willem, Luc, Jan-Pieter. I would like to thank Neha Singh (and her husband Sri) for the pleasant time spent together in Atlanta and for the precious and continuous support on ellipsometry data analysis.

Ringrazio i miei genitori Giuseppe e Fiorella per avermi dato la possibilità di arrivare fino qui, fino in fondo, per avermi lasciato ancora una volta correre libero verso i miei sogni e per aver sempre creduto in me e nelle mie intenzioni; mia sorella Silvia per non avermi mai fatto mancare il suo affetto.

Voglio poi ringraziare una lunga lista di amici, gli amici di sempre - tutti sempre al mio fianco, nelle serate, nei viaggi, sulle piste da sci ed anche in questa avventura: Benny, Luca, Gule, House, Marione, il Crema, Ciglio, Mister, Perny lo svizzero, Frank, Zurri, il capocordata Chandu, Giulio, Giò, Darione, Doris e la Vale, la Fra, il Mera, SaraM, Je Jey, SaraR. Nonostante i più svariati e differenti lavori e le inevitabili lontananze geografiche un grazie ai sempre presenti soci del Poli ed amici veri Cuz, Zan, il Colombo e Vale.

A tutte queste persone, ed a quelle che ho imperdonabilmente dimenticato, dico GRAZIE.

*“Questo è un laboratorio di ricerca. Ricercare vuol dire cercare di nuovo?
Vuol dire che stanno cercando qualcosa che avevano trovato una volta e che poi è scappata, in un modo o in un altro, e adesso devono ri-cercarla?”*

K. Vonnegut

Milano, 17 Dicembre 2009

Luca Lamagna

Curriculum Vitae

Personal information

First name: Luca
Family name: Lamagna
Place and date of birth: Milano, Italy - 24 November 1982
E-mail: luca.lamagna@gmail.com

Education

July 2001: Diploma di maturità scientifica
Liceo Scientifico “Niccolò Machiavelli”
Pioltello (MI), Italy.

October 2004: Bachelor of Science, Materials Engineering
Politecnico di Milano, Italy.

October 2006: Master of Science, Materials Engineering
Politecnico di Milano, Italy.

November 2006 – 2009: Ph.D. student, “Nanostructures & Nanotechnologies”
Università degli Studi di Milano-Bicocca
Laboratorio Nazionale MDM, CNR-INFN,
Agrate Brianza (MI), Italy.

Three months internship in the Plasma & Materials
Processing group, Department of Applied Physics,
Eindhoven University of Technology, Eindhoven,
The Netherlands.

Currently at Laboratorio Nazionale MDM, CNR-INFN, Post-Doc position.

An online record is available on: <http://www.boa.unimib.it/>

© 2009 Luca Lamagna and Laboratorio Nazionale MDM, CNR-INFM.
All rights reserved. This work may not be translated or copied in whole or in part without
the written permission of the author.